Sensitivity studies on the SciBar Cosmic Ray Telescope (SciCRT) at full performance for ground-based observations of solar neutrons

Yoshinori Sasai

Division of Particle and Astrophysical Science
Graduate School of Science
Nagoya University
Japan
March, 2017

NAGOYA
UNIVERSITY

Abstract

Cosmic rays have been studied over the course of one century. However, the origin and acceleration mechanism of particles are not fully understood. Sun is the nearest cosmic-ray source, which allows us to detect particles directly. Therefore, we are able to regard it as a cosmic laboratory for studying the cosmic-ray acceleration. It is known that solar flares have a potential to accelerate ions to multi-GeV energies in the maximum case. Solar neutrons are byproducts of interactions between accelerated ions and the solar atmosphere. A part of neutrons can escape from the influence of beta decay and may travel into the vicinity of the Earth. Although neutrons originated from the Sun are influenced by the attenuation in the atmosphere of the Earth, high energy neutrons (>100 MeV) may be detectable at high altitudes. About 10 solar neutron events have thus far been registered by a world-wide network of Neutron Monitors (NMs) since the first detection was made in 1957. Solar Neutron Telescopes (SNTs) have been deployed at seven summits of high altitudes on the globe since the latter half of 1990's. SNTs have a capability to measure energies of incident neutrons with four energy thresholds, but the capability has been hardly demonstrated, because of fewer statistics of neutrons.

SciBar Cosmic Ray Telescope (SciCRT) is a new solar neutron telescope installed at the top of Mt. Sierra Negra (4600 m) in the middle of Mexico, which uses the SciBar detector constructed for long-baseline neutrino oscillation experiments. This detector is characterized by a fully active scintillator tracker. That is to say this telescope can acquire not only the trigger rate of neutrons by scaler (neutron scaler) but also the energy deposit which is converted into ADC counts (neutron ADC). The SciCRT began to acquire these data using the SciBar's electronics in September 2013.

At such a high mountain, the proportion of background neutrons are 30 times (>1 MeV) higher than the ground at 0 meter above sea level. Therefore, the dominant background components must be fully understood to extract solar neutron components. However, the trigger rate of neutrons is very limited by dead time under the situation using the original electronics. Neutron

scalers have a limited time window to count the trigger rate of neutrons, because of the VME readout noise. Furthermore, the readout rate of neutron ADC data is significantly limited by a combination of back-end boards and VME bus.

Therefore, I began to develop faster and more reliable new back-end boards (BEBs). I adopted network communication via Ethernet for data transmission instead of the VME bus. It is realized by SiTCP which is a hardware-based network processor. Two new BEBs were designed and developed in March 2014. The performance of these new BEBs were evaluated by several tests. As a consequence of evaluations for a single board, it was found that a new BEB achieves a very low noise level and have a potential of 20 times faster readout rate of neutron ADC data compared with an old BEB. After minor changes, additional eight new BEBs were produced in March 2015. The performance tests were made for these new BEBs. After assembly of these nine new BEBs, I eventually installed new DAQ systems in muon layers and 1/8 of the neutron detection part of the SciCRT in July 2015. Although the new DAQ system processes multiple new BEBs, the throughput rate is 10 times faster than that of the old one for neutron ADC data. This confirms that the expected performance of the new DAQ system was achieved.

Based on the results of performance tests of the new DAQ systems, the future performance of the SciCRT was studied by using the Monte Carlo simulation. Assuming a case that new DAQ systems are equipped in a half size of the SciCRT, I simulated the same emission of solar neutrons as occurred on 2005 September 7. Neutron scaler data are comparable with data obtained by SNTs. The sensitivity will be enhanced up to 3.6 times in comparison with the conventional Mexico SNT installed at the top of Mt. Sierra Negra. Therefore, it can be said that the SciCRT will be the most sensitive solar neutron telescope at the ground in the world, albeit a half size of the full configuration. Furthermore, the event-by-event track and its energy deposition followed by neutron ADC data are a fully new function compared with SNTs. It is possible to discriminate a difference of the power-law index 0.1. It was confirmed that the new DAQ system enables us to acquire neutron ADC data in a nearly ideal situation. According to these results, it is expected to obtain more solar neutron events with high statistics of neutrons and pursue much more detailed information on ion acceleration mechanism at the solar surface.

Acknowledgments

I am grateful to my research adviser Prof. Yutaka Matsubara for giving me an opportunity for this research. He permitted to participate in the experimental group: SciCRT. It enables me to learn an attitude to the research from his sometimes kind and sometimes strict observations. I wish to thank Prof. Yoshitaka Itow for advice on the experiment. He has pointed out many things from his experience through the K2K experiment. As a leader of our Open-It project, his leadership led me to a smooth development environment. I am thankful to Dr. Takashi Sako. His professional advice around the detector has led me the correct way to our experiment. He has listened to my problems and given me advice about the development of the new BEB.

I am grateful to the member of the SciCRT collaboration. I wish to thank Prof. Valdés-Galicia for giving chances to do experiments at Sierra Negra in Mexico. His powerful support makes me facilitate experiments. I really appreciate his concern to my stay in Mexico. I would like to thank for help to collaborate the experiment to Mexican members: L. X. González, O. Musalem, A. Hurtado, E. Ortiz, M. Anzorena, M. Barrantes, R. Garcia, R. Taylor.

I wish to thank Mr. Tetsuya Kawabata for corporation for development of the new BEB. We have discussed about many problems. He taught me how to curiously face the tasks through the development. I am firstly thankful to Dr. T. Uchida for giving an opportunity to learn SiTCP at KEK. Furthermore he kindly taught me how to solve problems around SiTCP for new BEBs. Mr. T. Ikeno helps a design of the new BEB circuit and give comments to mistakes of the PCB design which we could not notice as a professional. Prof. M. Tanaka also help us to comment to the architecture of new BEBs through his experience for development of old BEBs for the SciBar detector.

I am thankful members of Cosmic Ray Research Group in Nagoya University: Prof. H. Tajima, Prof. K. Masuda, Prof. F. Abe, Dr. K. Yamaoka, Dr. A. Okumura, Dr. F. Miyake, Dr. D. Lopez, Mr. N. Hidaka, Mr. H. Takiya, Mr. Y. Makino, Ms. E. Matsubayashi, Ms. A. Suzuki, Mr. Q. Zhou, Mr. R. Hikimochi, Mr. Y. Okuno, Mr. Y. Wakiyama, Ms. R. Kegasa, Mr.

A. Tsuchiya.

I am grateful to the SciBar and SciBooNe experiments teams for allowing our group to use the SciBar as a cosmic-ray detector. I would like to acknowledge supports from the Japan Society for Promotion of Science (JSPS). Grants from CONACyT and PAPIIT-UNAM are also acknowledged. This work is also supported in part by the joint research program of the Solar Terrestrial Environment Laboratory (STEL) and Institute for Space-Earth Environmental Research (ISEE), Nagoya University. Funding from the Leadership Development Program for Space Exploration and Research of Nagoya University Program for Leading Graduate School is gratefully acknowledgement. I also thank advice and help by the development of the Open-It consortium.

Yoshinori Sasai
Nagoya, Japan
December 2016

Contents

Chapter 1

Introduction

In this chapter, I summarize a review of cosmic-ray physics including state-of-the-art results in Section 1.1. Then I describe the acceleration mechanism of high-energy particles in association with solar flares at the Sun in Section 1.2. This section focuses on the acceleration of ions such as protons and heavy nuclei, which is related to cosmic-ray physics. Thus, I describe the measurement methods of such ions: observations of ions and secondary neutral particles in space and on the ground of the Earth in Section 1.3.

1.1 Cosmic-ray physics

Cosmic rays have been researched over the course of 100 years since Victor Hess proved the existence of cosmic rays in 1912 (Hess, 1912). He demonstrated that the proportion of ionizations increased as altitude increased up to about 5 km above the ground in a free balloon flight. He concluded that these ionizations come from the upper atmosphere. That was a discovery of cosmic rays. The term "cosmic rays" was first appeared in Millikan (1926) written by Roberto Millikan who is a Nobel prize laureate.

Pierre Victor Auger found that a single cosmic-ray event is coincident with other single event, which leads to indirect discovery of an air shower (Auger et al., 1939). He estimated that a large air shower is created in the atmosphere by incident particles which have the energy of at least 10^{15} eV. This confirmed that high-energy cosmic rays interact with oxygen and nitrogen molecules in the atmosphere of the Earth, producing low-energy particles detected on the ground, namely, gamma rays, neutrons, neutrinos, muons, electrons, and positrons. Research of air showers has opened a new world of

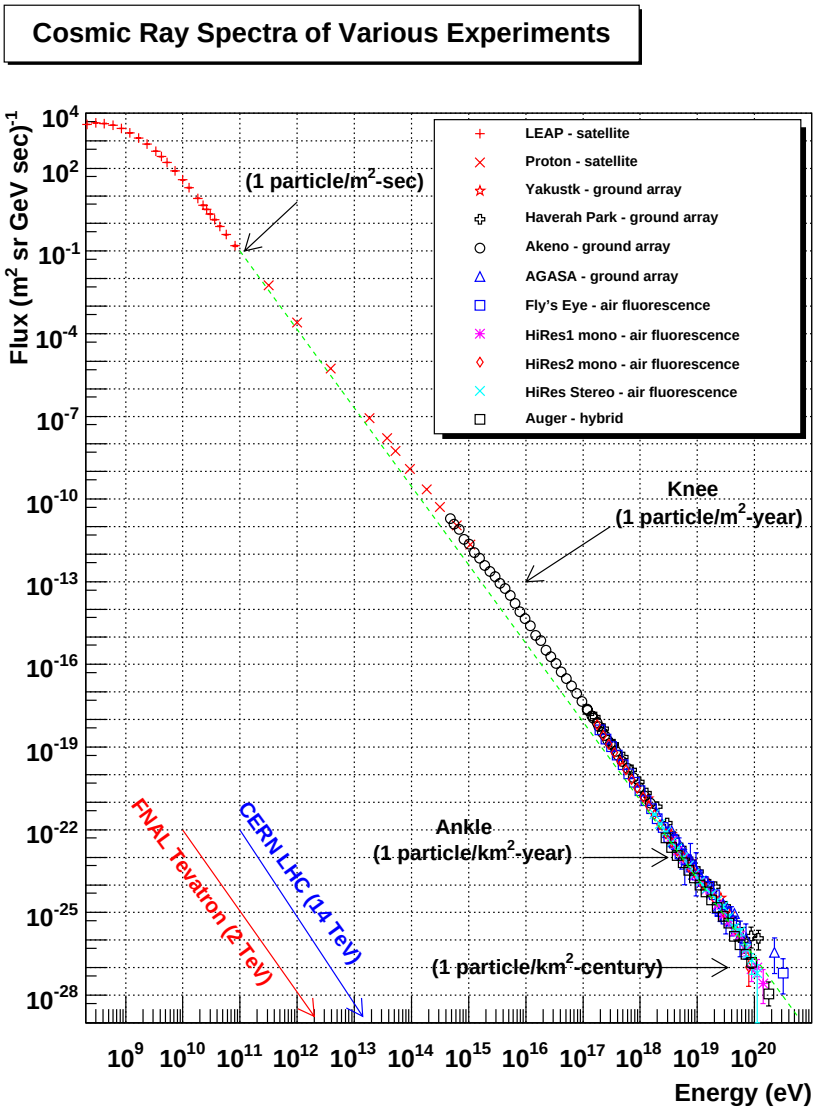

Figure 1.1: Cosmic-ray spectrum from 10^9 eV to 10^{21} eV. Available at: <http://www.physics.utah.edu/~whanlon/spectrum.html> [Accessed 29 November 2016]

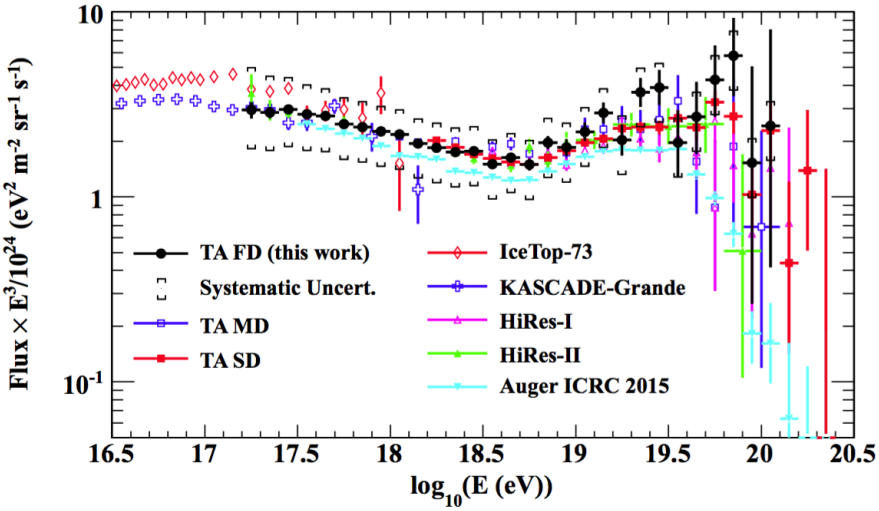

Figure 1.2: Energy spectrum above $10^{16.5}$ eV obtained by several experiments (Abbasi et al., 2016).

particle physics: a discovery of muons, mesons, and positrons. The maximum energy of cosmic rays exceeds 10^{20} eV. Although 100 years have passed, the origin and the acceleration mechanism of cosmic rays are not fully understood.

Figure 1.1 shows the cosmic-ray spectrum from 10^9 to 10^{21} eV. In the energy range below 10^{15} eV, cosmic rays have been measured by experiments using ballon-borne detectors and detectors onboard satellites represented by BESS, CREAM, PAMELA, and AMS-02. Due to the limited detector volume, it is difficult to detect high-energy cosmic rays with energies above 10^{15} eV. Thus, cosmic-ray induced showers have been measured by using ground-based detectors: the surface detectors and the fluorescence detectors, which are represented by AGASA, HIRES, the Pierre Auger Observatory (Auger), and Telescope Array experiment (TA).

In the energy range above 10^{11} eV, the cosmic-ray flux is not influenced by solar activity; the spectrum follows the power-law function of $E^{-\gamma}$. The spectral index, γ, is about 2.7 up to $10^{15.5}$ eV, where it changes to γ about 3.0. The spectrum softens slightly to γ about 3.3 around 10^{17} eV, and hardens again to γ about 2.7 just below 10^{19} eV. These three spectral-index discontinuities are called, the "knee", the "second knee", and the "ankle". Cosmic rays above 10^{18} eV are called ultra-high-energy cosmic rays (UHECRs). It is expected that UHECRs above $10^{19.7}$ eV interact with the Cosmic Microwave

Background (CMB) radiation via pion production or photo-disintegration processes, and the mean free path of UHECRs will be reduced. As a consequence, the energy spectrum above $10^{19.7}$ eV will be suppressed - the so-called GZK (Greisen-Zatsepin-Kuzmin) limit if the sources of cosmic rays are distributed uniformly. Figure 1.2 shows a recent result of the cosmic-ray spectrum above $10^{16.5}$ eV. The result of Auger is consistent with that of TA within the systematic uncertainty, but the spectrum shape at the edge is not completely same between two experiments. In any case, it is evident that there is the GZK cutoff around $10^{19.5}$ eV from observations thus far.

Cosmic rays are some varieties of particles, and the dominant components are different nuclei of ions. The chemical composition of cosmic rays below energies 10^{15} eV is as follows:

- 90% protons
- 10% nuclei of helium
- 1% heavier nuclei

Besides that, it is well known that about 1% and 0.1% of the components are electrons and gamma rays, respectively.

At energies higher than $10^{15.5}$ eV, the composition changes from lightweight particles to heavy ones. The maximum energy for galactic protons is about $10^{15.5}$ eV, whereas that for iron nuclei is about 10^{17} eV according to the popular models of cosmic-ray accelerations.

The views on the composition of UHECRs are not in accord. The recent result by Auger shows that the composition is consistent with protons nearby 10^{18} eV, but it changes to heavier ions as the energy approaches to 10^{20} eV. According to TA, the measurement indicates that the result is not in contradiction with protons in the whole energy range.

On the other hand, neutral particles such as photons and neutrinos are produced by interactions between high-energy particles and matters. Observations of these particles are useful to search the sources of high-energy particles and the acceleration mechanism. Very-high-energy photons can be produced through various radiative processes, e.g., synchrotron radiation, inverse Compton processes, and hadronic interactions. In terms of the hadronic processes, there are two leading processes: inelastic pp collisions and photo-hadronic pγ interactions. A common feature of pp and pγ is the production

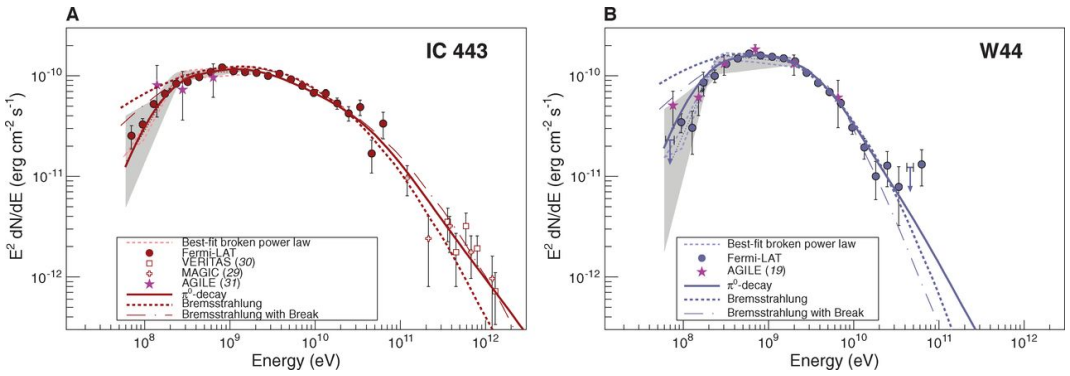

Figure 1.3: Gamma-ray spectra of two supernova remnants, W44 (Left) and IC 443 (Right), measured by the Fermi and other TeV gamma-ray observations (Ackermann et al., 2013). The red line shows a neutral pion decay model induced by accelerated protons. Two kinds of dashed lines mean a bremsstrahlung model caused by electrons.

of pions, which decay into photons ($\pi^0 \longrightarrow \gamma + \gamma$) and neutrinos (e.g., $\pi^+ \longrightarrow \mu^+ + \nu_\mu$, $\mu^+ \longrightarrow e^+ + \nu_e + \bar{\nu}_\mu$). This shows a beautiful connection between cosmic-ray, neutrino, and high-energy-photon astrophysics.

It is believed that the origin of cosmic-ray sources is supernova remnants in our galaxy up to the energy region of the knee. This scenario is partly supported by several reports which show the high energy gamma-ray emission from such a supernova remnant. When materials blowed by supernova explosion collide with interstellar gases and circumstellar materials, shock waves are formed in the interstellar space. It is considered that particles are boosted to high energies in the shock waves. The accelerated particles interact with surrounding materials, and high-energy gamma rays are emitted. These high-energy gamma rays erupted from supernova remnants such as W44 (Abdo et al., 2010a) and IC 443 (Abdo et al., 2010b) have been observed by the Fermi Gamma-Ray Space Telescope (Fermi). Furthermore, it was revealed that the energy spectrum of gamma rays at these supernova remnants has a good agreement with that of cosmic-ray protons with energies less than 200 MeV (Ackermann et al., 2013). Figure 1.3 shows gamma-ray spectra of these supernova remnants observed by the Fermi with other observations, comparing a few different scenarios of the gamma-ray production.

Although a part of our galaxy can be monitored by currently existing observations, Cherenkov Telescope Array (CTA) will cover the region of all the galaxy. Therefore, it is expected that more SNRs can be observed by the

CTA with its higher sensitivity over the wide range of energies.

Above around the knee, their origin (whether galactic or extra-galactic sources) is under discussion. Therefore, identification of cosmic-ray accelerators in which particles can reach at least the PeV energy domain (or "PeVatrons") is an important challenge at present. Recently the origin of the large gamma-ray glow around the centre of the galaxy was found by the High Energy Stereoscopic System (H.E.S.S.) (Abramowski et al., 2016). The shape and energy spectrum of these gamma rays may show that an unprecedentedly violent particle accelerator might lurk nearby a super-massive black hole (Sgr A*). This might be a first PeVatraon accelerator found in our Milky Way.

Besides, the IceCube observatory has detected two sub-PeV neutrino events thus far, including the highest energy event during the operation of seven years (Aartsen et al., 2016). These are considered as astrophysical neutrinos with 92.3% probability, which is produced by the interaction between UHECRs and photons or matters at the source, namely "in-situ" neutrinos. On the other hand, it is said that the highest energy of cosmogenic neutrinos may reach 100 EeV, namely GZK neutrinos. These neutrinos can be produced by the interaction between ultra-high-energy protons and the CMB, namely "off-situ" neutrinos. It is expected that such GZK neutrinos will be detected by an extension of the IceCube or radio Askaryan neutrino detectors.

It is thought that a strong candidate of UHECR sources may be GRBs and/or AGNs. The recent measurement by TA shows a sign of the hot spot around the legs of Ursa Major with 3.4σ above 57 EeV during an operation period of five years (Abbasi et al., 2014). On the other hand, Auger reported a correlation between the arrival direction of UHECRs above 57 EeV and the positions of AGNs with a confidence level of 99% from their operation of 3.7 years (Abraham et al., 2007). It was found that the correlation was lower than expected before with enlarged data sets (Kampert et al., 2012), but still about 3 σ excess exists. The recent result by Auger also shows the existence of the warm spot in the direction of the active galaxy Centaurus A in the Southern Hemisphere sky (Abreu et al., 2010).

In terms of the scenario of the particle acceleration, the exact acceleration scheme is not known, but standard scenarios are generally considered such as Fermi mechanisms and reconnection processes. As mentioned above, it is considered that high-energy particles may be accelerated by a strong shock in supernova remnants in our galaxy. As the shock velocity becomes

relativistic, the acceleration physics becomes quite different. Such accelerations at relativistic shock waves may take place in gamma-ray outflows (e.g., Piran 2005, Piron 2016), in blazar outflows (e.g., Dermer and Giebels, 2016), or trans-relativistic supernovae. They may be the source of cosmic-rays over a wide energy range. The process of magnetic reconnection has been proposed for high-energy particles in the solar corona (e.g., Priest et al., 2002). It has gained popularity as its phenomenological features may explain the rapid variability of blazer flares (e.g., Giannios et al., 2010), the flaring high-energy emission of the Crab nebula (e.g., Uzdensky et al., 2011, Cerutti et al., 2012) or the pulsed high-energy emission of pulsars (e.g., Cerutti et al., 2015).

As stated above, it has been studied about the origin of cosmic rays and the acceleration mechanism thus far and much has been understood in a past few decades. On the other hand, the Sun is an astronomical object which is identified as one of the origin of protons and nuclei which are boosted to multi-GeV energies. Although the maximum energy is lower than that of other astrophysical objects, the acceleration mechanism of these particles is related with the reconnection processes as well as the gamma-ray flares of the Crab nebula and other flares. The Sun is always monitored by multi-wavelength observations. Therefore, it can be said that the Sun is a suitable object for researching the particle acceleration mechanism. In Section 1.2, I refer to ion acceleration mechanism on the solar surface: particle acceleration model, observational methods, and what we learned from the past observations.

1.2 Particle acceleration via solar flares

The Sun is the nearest source of cosmic rays for us, and it enables us to observe particles directly from the known source. Solar flares are potential sources of particle acceleration. They produce high energy particles which do not exist in a steady state and are sometimes boosted to GeV energy region, whereas solar winds and neutrinos are always emitted from the Sun. Such high energy particles are classified as two categories: electron and ion (including protons and heavier nuclei). However, the acceleration site, and the acceleration mechanism has not been clarified. A review of solar flares is described here. I also give particle acceleration models based on the existing observations.

It is widely known that the release process of magnetic energies at the solar surface may be well explained by magnetic reconnection models firstly

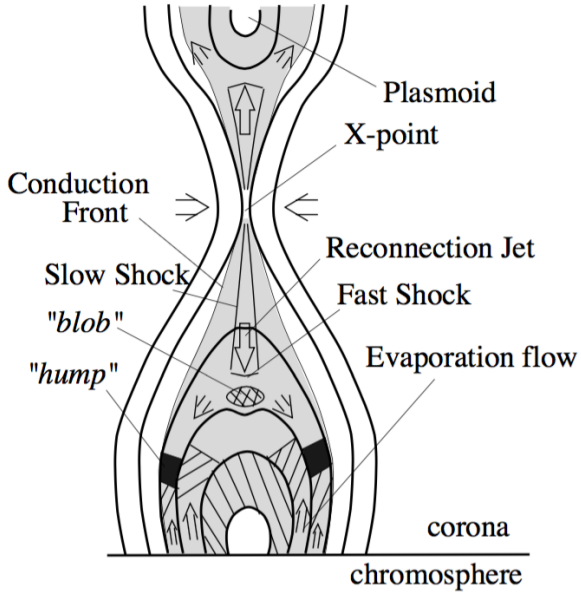

Figure 1.4: Schematic illustration of the reconnection model in solar flare suggested by Yokoyama and Shibata (2001). Thick solid lines show magnetic field.

suggested by R.G. Giovanelli, F. Hoye, P.A. Sweet, and E.N. Parker (Giovanelli 1946, Hoyle 1950, Sweet 1958, Parker 1957). The exsistence of magnetic reconnection models was confirmed by observations of solar flares via the Yohkoh satellite. A loop-top hard X-ray source in a compact flare was observed by Yohkoh Hard X-ray Telescope and Soft X-ray Telescope (Masuda et al., 1994). The cusp-shaped loop structure was also observed by the Soft X-ray Telescope (Tsuneta et al., 1992). Yokoyama and Shibata (2001) simulated magnetic reconnection of solar flares by the MHD simulation. It is found that the simulation reproduces observations of the Yohkoh satellite. Figure 1.4 illustrates a drawing of a standard magnetic reconnection model derived from the MHD simulation. However, these indicated phenomena have not been directly observed yet. More detailed observations are required to confirm the magnetic reconnection model.

Solar flares release huge amounts of energy in an active region at the solar atmosphere. It is widely known that the sunspot number has been increased and decreased repeatedly known as the solar cycle of 11 years shown in Figure 1.5. Sometimes one solar flare occurs during one month at the minimum solar activity, and sometimes more than 10 flares are registered during one day at the maximum solar activity. The total energy release attains 10^{32}

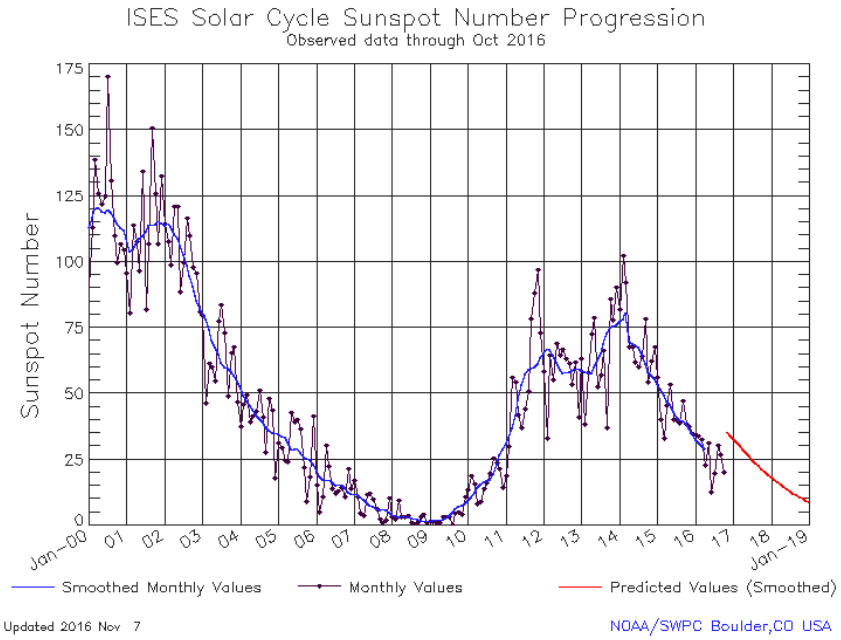

Figure 1.5: Solar cycle sunspot number progression since 2000. The monthly averaged value of the sunspot number is plotted by purple dots and lines. The blue curve means a smoothed one of monthly values. The red curve is a predicted one based on the current state. Available at: <http://www.swpc.noaa.gov/products/solar-cycle-progression> [Accessed 30 November 2016]

erg in the maximum case. Most of the energy release is delivered to kinetic energy of the ambient plasma, which sometimes induces Coronal Mass Ejections (CMEs). The rest is converted into processes of particle acceleration and electromagnetic radiation and so on. Solar flares induce increase of emission intensity at various wavelengths. Soft X-rays are radiated from the ambient plasma with a high temperature; therefore, the emission intensity of soft X-rays is considered as a standard of the total energy release from solar flares. The GOES always monitor solar flares, and then the emission intensity of soft X-rays is classified into five classes as in Table 1.1.

There are several theories to explain the particle acceleration mechanism which are consistent with observations. Hereafter I describe three representative theories.

Table 1.1: Classification of solar flares by the GOES: emission intensity of soft X rays in the vicinity of the Earth.

X-class	10^{-4} W/m^{-2}
M-class	10^{-5} W/m^{-2}
C-class	10^{-6} W/m^{-2}
B-class	10^{-7} W/m^{-2}
A-class	10^{-8} W/m^{-2}

Secondary fermi acceleration

Provided that V $\ll$ c and v $\simeq$ c. Considering particles at a velocity of v trapped in a magnetic mirror moving at a velocity of V, the velocity of particles will change to v+2V (v-2V) by the front (rear) collision to the moving magnetic mirror. Since the former case is dominant in comparison with the latter case, these particles will gain much energy through this magnetic trapping process as a consequence.

Shock acceleration

Provided that V $\ll$ c and v $\simeq$ c. Assuming that a strong shock wave moves at a velocity of V, particles at a velocity c gain an averaged energy of 2/3$\times$V/c by passage of the shock wave (4/3$\times$V/c for back and forth). Particles will be efficiently accelerated by the back and forth process. It is considered that the formation of shock waves may be caused due to the magnetic reconnection process in the downstream of solar flares and at front side in CMEs.

Electric field (DC) acceleration

The velocity distribution of thermal electrons in one region is well explained by the Maxwell distribution. If electric fields are given, a portion of the electrons can escape from the region. The strongest electric field which all the electrons can run away from the region is called "Dreicer field". In the case of the solar corona, the Dreicer field is equal to about 1 mV/m. DC electric field models can be categorized into two: weak sub-Dreicer and strong super-Dreicer models.

1.3 Observations of ions accelerated at the Sun

Two kinds of particles, electrons and ions, are accelerated associated with solar flares on the solar surface. The observations are roughly divided into three methods:

1. Direct observation of ions in space and on the ground
2. Gamma-ray observation in space
3. Neutron observation in space and on the ground

In this section, I review these three methods and observational results in each subsection.

1.3.1 Observations of SEPs and GLEs

Solar Energetic Particles (SEPs) are high-energy protons and other heavier ions coming from the Sun. Such particles are accelerated nearby the Sun by solar flares or in the interplanetary space by CME shocks. SEPs are deflected by interplanetary magnetic fields. Therefore, SEPs are observed associated with west-limb flares in most cases, because charged particles come along the magnetic field lines between the Sun and the Earth. High energy SEPs are seldom observed on the Earth, which is called as Ground Level Enhancement (GLE). GLEs represent the presence of high energy particles accelerated up to around GeV energy range in the Sun.

In space, SEPs are directly observed by detectors onboard satellites. It is possible to observe the particles which escape from the Sun to the interplanetary space. Since the particles are deflected by the solar and interplanetary magnetic field, it is not easy to specify the source. However, this in-situ measurement provides us with not only the flux of each particle but information about the magnetic field and precise measurements of different nuclei. The flux measurement of SEPs has been made by various near-Earth spacecraft at different locations (GOES, ACE, STEREO, SOHO, WIND).

GLEs have been mainly observed by Neutron Monitors (NMs) . Figure 1.6 shows a picture of the Mexico NM in Mexico City. Since NMs also have been used for solar neutron observation, I describe the configuration and the detection method in detail. Since 1957, NMs have been installed at

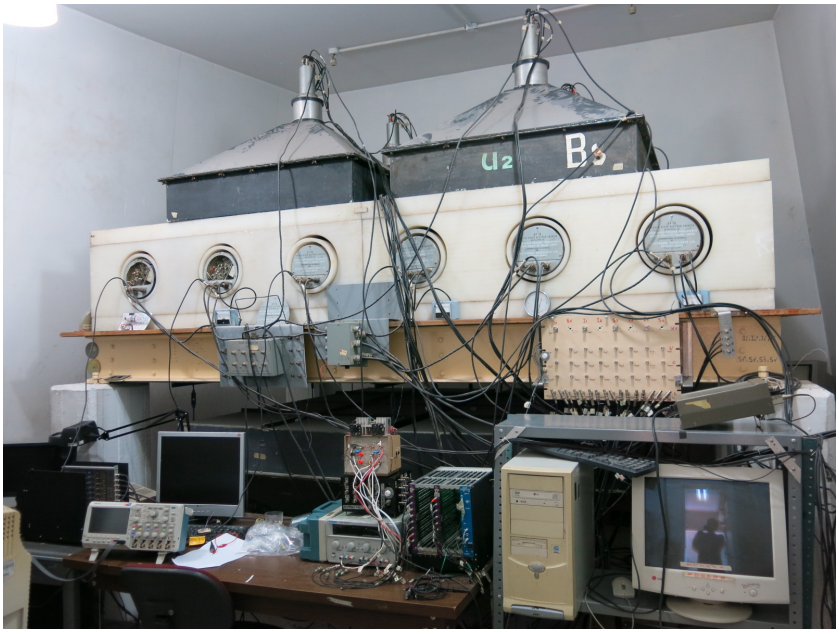

Figure 1.6: Picture of the NM installed in Mexico City. White parts are Polyethylene surrounding six neutron detectors.

various locations on the Earth for monitoring the flux of Galactic Cosmic Rays (GCRs). It consists of four components:

1. Reflector made of paraffin or polyethylene.
2. Producer made of lead.
3. Moderator made of paraffin or polyethylene.
4. Proportional Counter.

Thermal neutrons are captured by boron or helium, and α particle or proton may be finally detected in the Proportional Counter. The reactions are as follows:

$$^{10}\mathrm{B} + \mathrm{n} \longrightarrow {}^{7}\mathrm{Li} + \alpha$$

$$^{3}\mathrm{He} + \mathrm{n} \longrightarrow {}^{3}\mathrm{H} + \mathrm{p}$$

NMs are sensitive to both high energy protons and neutrons. NM has an advantage for its high detection efficiency. It is also easy to increase the volume, because of the simple architecture. But the energy of incident particles

cannot be measured directly by using NMs, because of the thermalization process.

The first GLE event associated with a flare on 1942 February 28 registered by ion chambers was reported by Forbush (Forbush, 1946). Since then, GLEs have been observed 71 times (Available at: <http://neutronm.bartol.udel.edu/~pyle/GLE_List.txt> [Accessed 2016 November 30]).

It is now widely agreed that SEPs come from two different sources with different acceleration mechanisms. The flares release impulsive events whereas the CME shocks produce gradual events (see the terminology discussion between the impulsive and gradual events by Cliver and Cane, 2002). The gradual event is dominated by protons. On the other hand, the flux of electrons are higher than those of the protons in the impulsive event.

1.3.2 Solar gamma-ray observations

Studies of gamma rays in the Sun have been gradually revealed by the development of detection technologies. Gamma-ray line emissions are occurred by several reactions:

1. $e^+ + e^-$ Annihilation with 511 keV delayed gamma-ray line.
2. Nuclear reactions: nuclear de-excitation lines at 4.4/6.1 MeV from Carbon/Oxygen, and neutron capture line at 2.223 MeV.
3. Bremsstrahlung via accelerated electrons.
4. Neutral pion decay production around 70 MeV.

In association with the ion acceleration, a variety of line gamma rays are produced by the nuclear interaction, i.e. 2.223 MeV neutron capture line, 4.4 MeV and 6.13 MeV de-excitation lines, and 70 MeV pion decay line. Besides these lines, the continuous spectrum of gamma rays is produced by the bremsstrahlung processed by accelerated electrons. Figure 1.7 is one example of gamma-ray spectrum observed by OSSE/CGRO in association with a flare on 1991 June 4.

The electron/positron annihilation lines at 511 keV were clearly detected by the solar gamma-ray monitor onboard OSO-7 (Orbiting Solar Observatory 7) in one of the series of American Orbiting Solar Observatory satellites

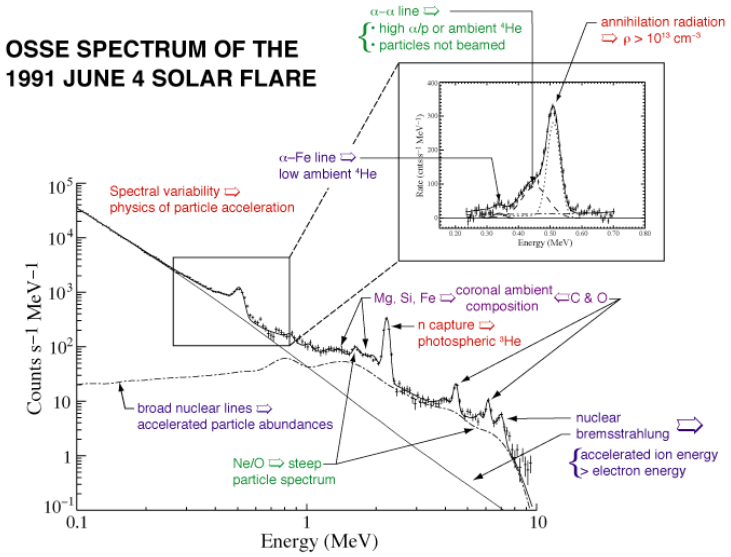

Figure 1.7: Example of the gamma-ray spectrum associated with the 1991 June 4 flare. Available at: <https://heasarc.gsfc.nasa.gov> [Accessed 2016 November 30]

in 1970's. These gamma-ray line observations were followed by the Gamma Ray Spectrometer (GRS) on the Solar Maximum Misson (SMM) satellite launched in 1980. The satellite successfully detected multiple gamma-ray lines at different flare events, and it enabled us to discuss about particle acceleration mechanism and a relationship between observed gamma-ray lines and accelerated particles. The observation over a wide energy range (10 keV to 30 GeV) was performed by four detectors (BASTE, OSSE, COMPTEL, and EGRET) onboard the Compton Gamma Ray Observatory (CGRO) from 1990's. The EGRET which aims to observe high energy gamma rays from 20 MeV to 30 GeV detected totally three energetic events associated with X-class flares. In the 2000s and later, two observatories have led the solar gamma-ray observation: Reuven Ramaty High Energy Solar Spectroscopic Imager (RHESSI) and Fermi Gamma-ray Space Telescope (Fermi). In this paper, I follow recent status of solar gamma-ray observation by these two satellites.

The RHESSI has opened a new era to search the physics of particle acceleration and energy release at the Sun. The primary feature is an imaging technique over the energy range from 3 keV (X-rays) to 20 MeV (Gamma Rays) and make observations with high energy resolution (about 1 keV resolution at 100 keV).

The RHESSI gave a first-ever imaging of energetic ions through nuclear gamma-ray observations (Hurford et al. 2003, Hurford et al. 2006). Figure 1.8 shows the observed ion/electron double foot points overlaid on the TRACE image. This may indicate that the magnetic reconnection model is also supported for the ion acceleration mechanism, but the difference between ion and electron foot points cannot be explained. More precise separation of these ion/electron foot points will be given by other experiments such as a future plan of the Gamma-Ray Imager/Polarimeter for Solar flares (GRIPS) instrument with its high spatial resolution.

The Fermi has the Gamma-ray Burst Monitor (GBM) and the Large Area Telescope (LAT). The GBM which has a combination of BGO and NaI scintillators is sensitive to the energy range from 8 keV to 40 MeV, whereas the LAT, a pair conversion telescope, is sensitive from 20 MeV to > 300 GeV. Especially, the LAT enables us to detect high energy gamma rays from pion decay induced by accelerated protons and ambient plasma at around 70 MeV. These high energy gamma rays had been hardly observed for the recent two decades.

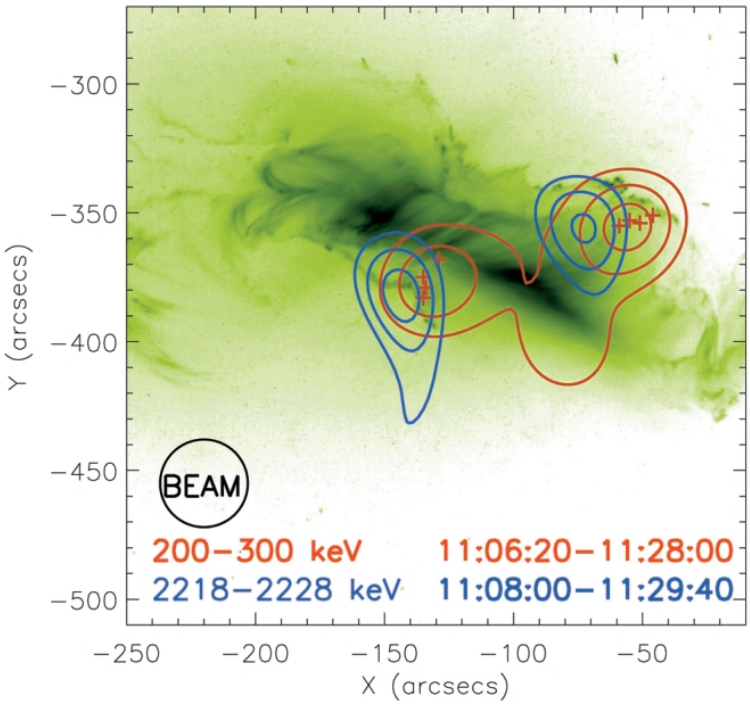

Figure 1.8: Overlay of the 50%, 70%, and 90% contours of gamma-ray images made with the TRACE image (195 $\mathring{A}$) for the 2003 October 28 flare. Double ion and electron foot points detected by RHESSI (Hurford et al., 2006), with blue and red lines, respectively.

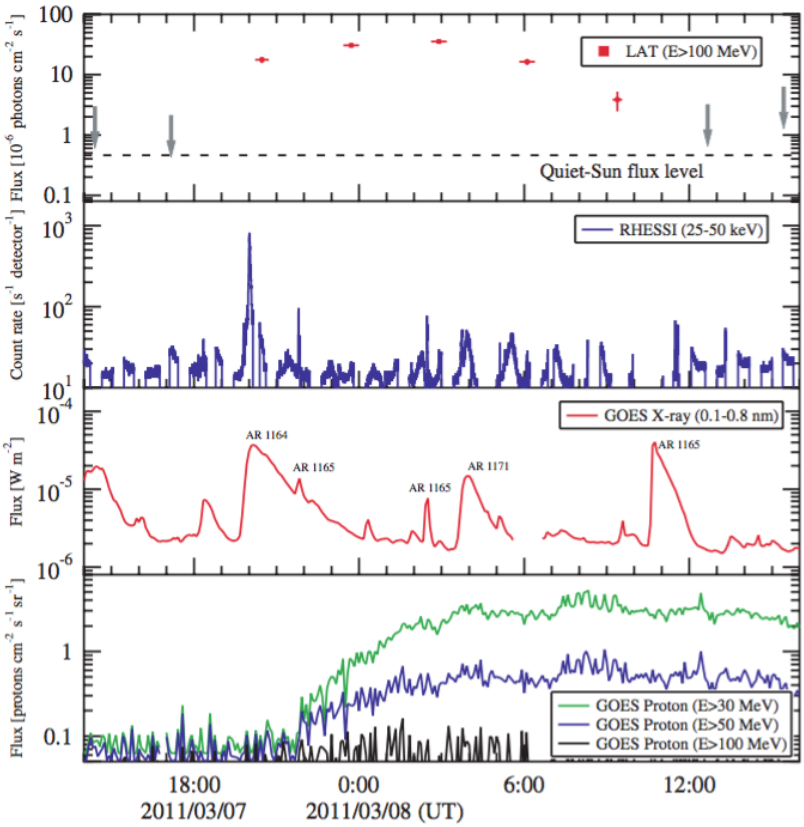

Figure 1.9: Multi-wavelength and proton light curves in context with the M3.7 flare in 2011 March 7 (Ackermann et al., 2014). Gamma-ray data are detected by the Fermi LAT, hard X-rays are from the RHESSI, and soft X-rays and protons come from the GOES.

Since the Fermi was successfully launched in 2008, the LAT has detected both impulsive events and long duration events associated with not only X-class solar flares but modest M-class flares. The long-duration gamma-ray emission was detected lasting 12 hours in associated with two flares occurred on 2011 March 7 (Ackermann et al., 2014), although there are no such long duration emissions for other wavelengths as shown in Figure 1.9. The brightest event occurred in 2012 March 7, whose flux is equivalent with 1000 times larger than the flux of the quiet Sun (Ajello et al., 2014). High energy emission (>100 MeV, up to 4 GeV) has lasted for around 20 hours. Thanks for the improved LAT's angular resolution, the gamma-ray emission was localized nearby the active region 11429 for this event.

Ackermann et al. (2014) discuss about the high energy gamma-ray emis-

sion with an energy of about 1 GeV recorded in association with the 2011 March 7 flares. If this is due to pion decay, this corresponds to an energy of protons about 5 GeV. If the high energy gamma-ray emission is caused by bremsstrahlung via accelerated electrons, the electron spectrum should extend beyond 1 GeV. But it is too difficult to produce such gamma rays by bremsstrahlung by existing observations and emission mechanisms in the coronal chromosphere. The pion decay scenario seems more plausible.

Ajello et al. (2014) describes the highest energy gamma-ray event on 2012 March 7. They discussed about several important parameters: continuous versus prompt acceleration in a magnetic trap, proton versus electron emission, and acceleration at the coronal reconnection site versus CME shock. They conclude that the most likely scenario is continuous acceleration of protons in the solar corona that penetrate the lower atmosphere and produce pions that decay into gamma rays.

1.3.3 Solar neutron observations

Since solar neutrons are produced by the interaction between accelerated ions and the ambient plasma in the Sun, the measurement provides us with valuable information about the acceleration mechanism of ions. Two production models are raised to explain solar neutron production: the thick and thin target models. A difference between two models is a depth of the production. The former is the corona, whereas the latter is the chromosphere or the photosphere. Chupp (1984) explained the production mechanism of solar neutrons using the thick target model and concluded that solar neutrons are generated where the densities of hydrogen atoms exceed $10^{12}/\mathrm{cm}^3$. This means deeper place than the chromosphere at 1000-1200 km. Based on the thick target model, Murphy et al. (1987) calculated the production rate of neutrons and gamma rays in the solar atmosphere using stochastic and shock acceleration models, respectively. Figure 1.10 shows solar neutron production spectra assuming stochastic and shock acceleration and the ambient plasma. For the stochastic acceleration spectrum, below 10 MeV the bulk of neutrons are produced by accelerated protons (mostly via p-α reactions), while at higher energies the bulk of the production is due to fast alpha particles (mostly via α-p and α-α reactions). The total neutron production is very sensitive to the composition of the ambient plasma. For the shock acceleration spectrum, the bulk of the neutrons are produced by accelerated protons, mostly via p-α reactions at low energies and p-p reactions at high energies. The total neutron spectrum is not sensitive to the composition of the ambient plasma.

Neutrons are not deflected by the interplanetary magnetic field between the Sun and the Earth. Free neutrons are unstable and induce the β decay in a mean lifetime of about 885 sec:

$$n \longrightarrow p + e^{-} + \overline{\nu}_e \tag{1.1}$$

Figure 1.11 shows the neutron survival probability during a distance of 1 AU. About 30% neutrons can come across the 1 AU distance assuming an impulsive emission of 100 MeV neutrons at the Sun. Therefore, solar neutrons may be detected in space and on the ground of the Earth. Neutron decay products (protons and electrons) may be detected if these particles can be distinguished from SEPs themselves, and such events have been reported to date (Evenson et al. 1983, Agueda et al. 2011).

In space, lower energy neutrons have been observed by detectors onboard satellite. The first solar neutron event was detected associated with a solar flare on 1980 June 21 by Gamma Ray Spectrometer (GRS) on the Solar Maximum Misson (SMM) satellite. It is however difficult to discriminate neutrons from gamma rays using NAI and CsI scintillators equipped on the GRS.

A new type of Neutron Monitor (NEM) of the Space Environment Data Aquisition equipment - Attached Payload: SEDA-AP started to acquire data on the International Space Station (ISS) in the middle of 2009. A scintillation fiber detector (FIB) has a dimension of $10 \times 10 \times 10$ cm^3. One layer consists of 16 scintillation fibers, and 16×2 layers are read out from two sides of the detector using two sets of 256-channel Multi-Anode Photo Multiplier Tubes (MAPMTs). It is entirely surrounded by active veto counters. It is sensitive to the energy range of 15-100 MeV neutrons.

About 200 solar flares occurred during the SEDA-AP operational period from 2009 to 2014 were analysed. Twenty-one neutron events associated with the solar flares were found. A detailed analysis was performed for three events (Muraki et al., 2015), in which simultaneous observation of solar neutrons by using the MESSENGER and the SNTs on the ground of the Earth described in this subsection were available. From the detailed analysis of these events, two possible candidates of neutron production mechanisms are suggested. Sakai and Jager (1996) suggest that a strong electric field is formed by the

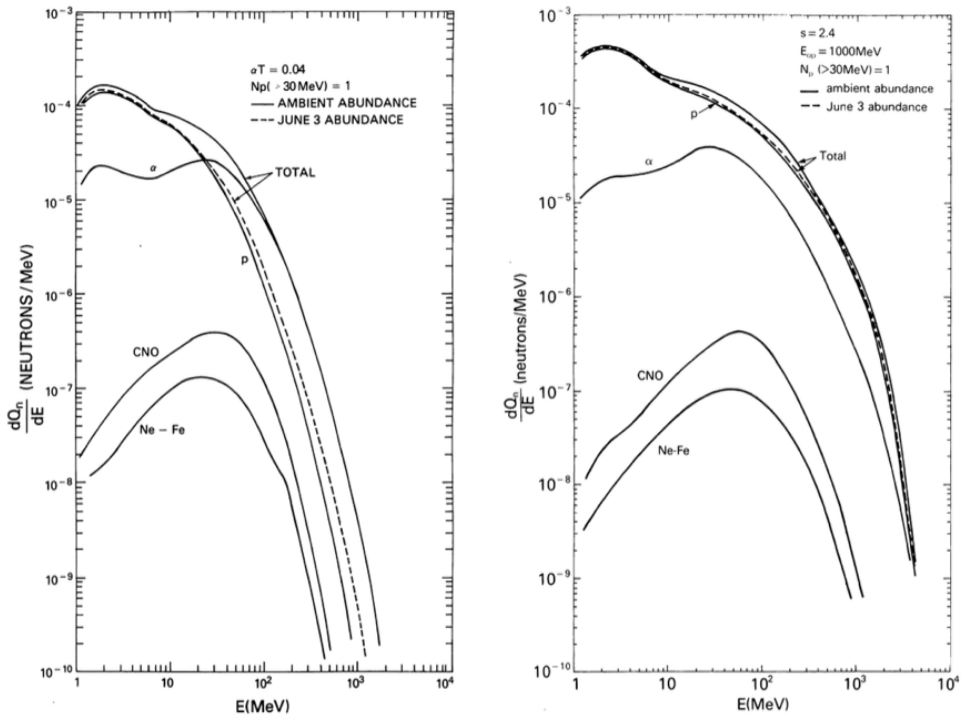

Figure 1.10: Left: Neutron production spectra assuming a stochastic acceleration spectrum with αT = 0.04 and ambient composition. Right: Neutron production spectra assuming a shock acceleration spectrum with s = 2.4 and E_{0p} = 1000 MeV and ambient composition. The dashed curve shows the total neutron production spectrum for a primary composition given by the June 3 composition. Curves labeled p, α, CNO, and Ne-Fe represent neutron spectra from energetic protons, alpha particles, C, N, and O nuclei, and nuclei from Ne through Fe interacting with the ambient plasma. (Murphy et al., 1987)

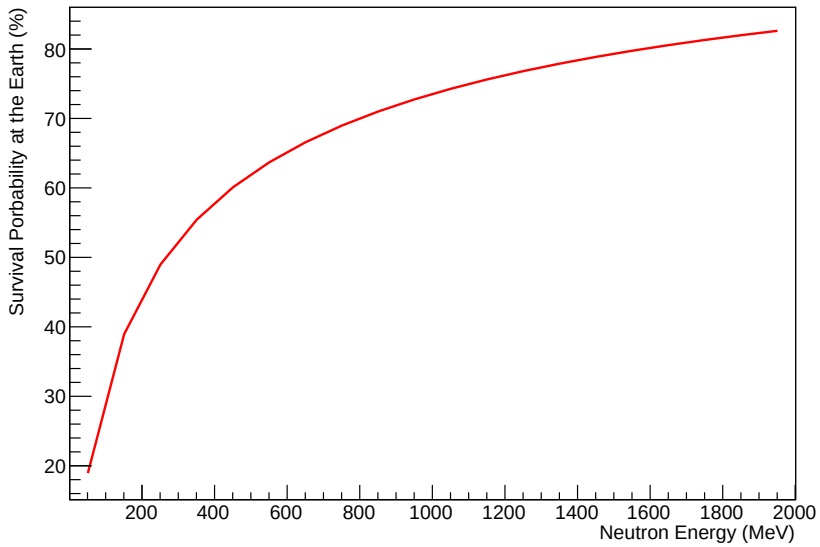

Figure 1.11: Neutron survival probability at the distance of 1 AU, considering the relativistic effect.

collision of two current loops, so that protons are accelerated to around 100 GeV. Another possible scenario is the shock acceleration at the front side of CMEs, modeled by Mandzhavidze and Ramaty (1992).

MErcury Surface, Space ENvironment, GEochemistry, and Ranging (MESSENGER) was launched on 2004 August 3, and was inserted into an orbit around Mercury in 2011 March. Gamma-Ray and Neutron Spectrometers (GRS and NS) are equipped with MESSENGER to collect complementary data on elements that form Mercury's crust (Goldsten et al., 2007). NS can measure the energy of neutrons with three energy ranges from thermal to about 7 MeV. At the far distance of Mercury, they may discriminate solar neutrons from Mercury's neutrons. Feldman et al. (2010) and Lawrence et al. (2014) reported that the data from NS and GRS indicates that neutrons have a solar origin associated with a solar flare on 2007 December 31 and 2011 June 4. It is, however, difficult to discriminate solar neutrons from neutrons induced by low energy charged particles. Actually whether these events are caused by solar neutrons is under discussion (Share et al., 2011, Share et al., 2015, Lawrence et al., 2015). Rejecting a possibility of the enhancement due to the energetic-ion-induced neutrons, they use energetic ion spectrometers on several spacecraft at 1 AU, which is magnetically connected to MESSEN-

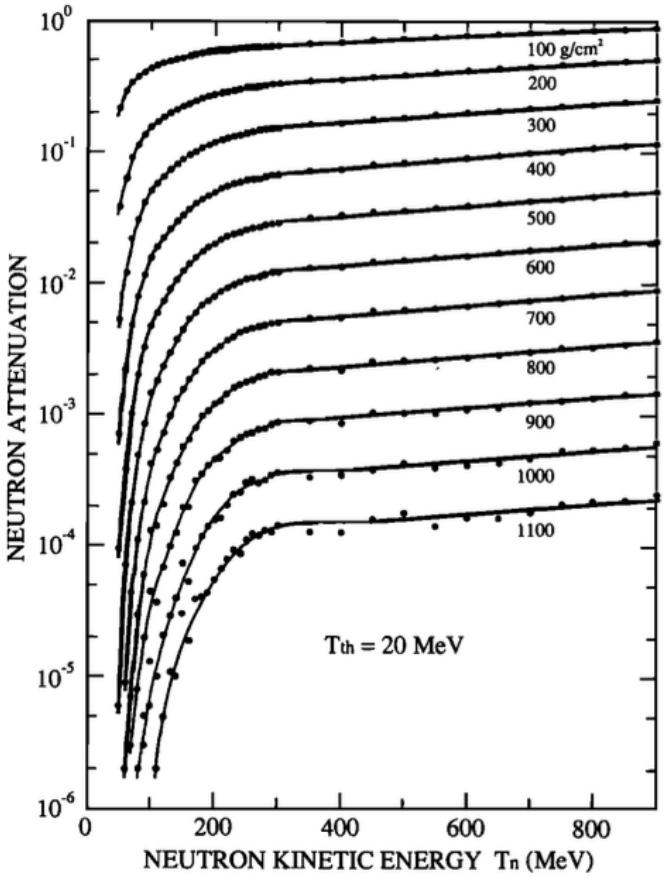

Figure 1.12: Neutron attenuation due to the Earth's atmosphere as a function of the incident energies of neutrons at the top of the atmosphere (Shibata 1994). Each curve is derived from data corresponding to the atmospheric depth. The threshold energy is set to 20 MeV.

GER during the event (Feldman et al., 2015). As a result of the analysis, six neutron events do not have the origin at the local spacecraft.

Solar neutrons have thus far been observed in space and on the Earth. Neutrons are attenuated in the earth's atmosphere. Therefore, it is possible to detect high energy solar neutrons (>100 MeV) at high altitudes on the earth. Figure 1.12 shows an influence of the atmospheric attenuation to neutrons calculated by Shibata (Shibata 1994). According to the calculation, we can expect to detect high energy solar neutrons having the energy larger than about 50 MeV at high altitudes.

On the Earth, solar neutron events associated with solar flares have thus far been observed by the network of Solar Neutron Telescopes (SNTs) and NMs explained in Subsection 1.3.1. The ground-based observation has a merit in the sense that we can put a large volume detector. The SNT has basically three components:

1. Target scintillator. Protons are produced by the nuclear interaction between neutrons and hydrogen or carbon in the scintillator.

2. Anti counter. This is used to veto background charged particles.

3. Directional detection counters.

Our group has introduced SNTs to seven high altitude locations near the equator, Gornergrat (Swiss), Aragats (Armenia), Yangbajing (Tibet), Norikura (Japan), Mauna Kea (Hawai), Sierra Negra (Mexico), and Chacaltaya (Bolivia). It enables us to monitor solar neutron events for 24 hours continuously.

In the target scintillator, plastic scintillators are used. Therefore, the reaction between neutrons and the scintillators is $n + p \longrightarrow p + n$ or $n + C \longrightarrow p + X$. The energy of neutron-induced protons reflect that of incident neutrons. Proportional counters or plastic scintillators are used for the anti counter. Figure 1.13 illustrates a schematic view of the SNT installed at Mt. Sierra Negra in Mexico. The Mexico SNT has plastic scintillators of a 4 m^2 area and 30 cm thickness covered by gondolas of proportional counters as anticounter. The threshold level of the Mexico SNT is set by the different four levels of energies: 30, 60, 90, and 120 MeV, respectively.

Since we can not measure the energy and the direction of neutrons by NMs as discussed in Subsection 1.3.1, the energy spectrum is always calculated by using their time-of-flight (TOF) method assuming the emission profile at the solar surface. These methods are well described in Watanabe et al. (2006). But an actual emission profile may be different from the assumed emission profile. On the other hand, we are able to measure the energy of neutrons and the direction by SNTs.

Solar neutron events in association with five and six solar flares were detected before and after solar cycle 23, respectively. Watanabe (2005) performed the comprehensive discussion for these events but the last event which is associated with a flare on 2005 September 7. This event was discussed in several papers: Sako et al. (2006), Watanabe et al. (2007), Watanabe et al.

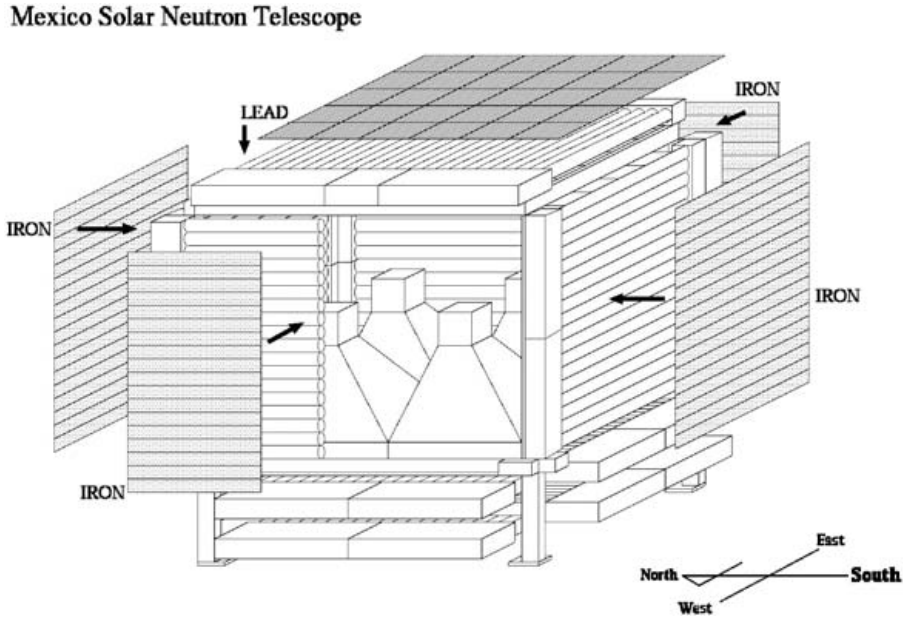

Figure 1.13: Schematic view of the Solar Neutron Telescope (SNT) located at Mt. Sierra Negra, Mexico (Valdés-Galicia et al., 2004).

(2009), González et al. (2015).

In solar cycle 23, more than 100 X-class solar flares have been observed by GOES satellites. More than 5 σ enhancements of the count rate on NMs are coincident with five of them: 2000 November 24, 2001 August 25, 2003 October 28, 2003 November 2, and 2003 November 4. These events were registered by hard X- and gamma-ray detectors, RHESSI and INTEGRAL. Assuming that the emission of solar neutrons is coincident with that of gamma rays, the energy spectrum of neutrons for these events was fitted by the power-law function, and the spectral index α_n is equal to 3-4. Then the energy spectrum of ions can be reconstructed from that of the observed neutrons using a flare magnetic-loop transport and interaction model given by Hua et al. (2002). The calculated result shows that α_p = 3-5, and the total flux of ions is equal to 10^{30} - 10^{33}.

A most significant event occurred in association with a X17.0-class solar flare on 2005 September 7. Since this event is quite important for understandings solar neutrons, I discuss about this event based on several reports. Furthermore, I describe the most recent solar neutron event in association

with the 2004 July 8 solar flare, reported by Muraki et al. (2015).

Relativistic neutrons were observed by four ground detectors: the SNTs and NMs located at Mexico and Bolivia respectively. Sako et al. (2006) reported that the significance of the event is 40 σ, 9 σ, 12 σ, and 16 σ for the Bolivia NM, the Mexico NM, the Bolivia SNT ($>$ 40 MeV), and the Mexico SNT ($>$ 30 MeV neutral channel). They assumed a model that ground-detected neutrons are emitted with the same profile as the hard X-rays and γ-rays detected by INTEGRAL and GEOTAIL. Then data obtained at the Bolivia NM is best fitted to a single-power-law spectrum with an index of –3.2. The rising edge of the profile is well-fitted with a sharp cutoff at 400 MeV. They however could not fit with any set of parameters to a tail of the data. They summarized that this indicates that ions were continuously accelerated or trapped for a longer period than the electrons.

INTEGRAL also observed the 4.4 MeV line γ-rays. Assuming that the emission of neutrons is consistent with that of these gamma rays at the peak time 17:36:40 UTC, Watanabe et al. (2007) calculated the energy spectrum of neutrons. By fitting the spectrum by a power-law function, the spectral index was estimated to be –3.8. The neutron flux is 6×10^{27} MeV^{-1} sr^{-1} at 100 MeV. Regarding the shape of the rising edge for the neutron time profile, the cut off energy was estimated to be about 500 MeV. But the decay component of the time profile can not be explained using the time profile of the impulsive γ-ray emission. This may indicate a possible extended neutron emission.

Furthermore, Watanabe et al. (2009) performed the detailed calculation using the flare magnetic-loop transport and interaction model (Hua et al., 2002) to explain time profiles of solar neutrons observed at the Earth and 2.2 MeV neutron-capture γ-ray line by INTEGRAL. Figure 1.14 shows a time profile of the Bolivia NM and 2.2 MeV neutron capture line detected by INTEGRAL. They attempted to determine which process is dominant, long acceleration or trapping. An acceptable fitting result was obtained using 4.4 MeV line time profile. At that time, the accelerated ion spectral index is estimated to be about 4.5. Then they concluded that a portion of ions has been trapped in the flare loop, although others are accelerated over a term of γ-ray emission.

González et al. (2015) used an another approach to re-evaluate the neutron emission using a GEANT4-based detector simulation and the data of the threshold channel revealed the most clear excess obtained by the Mexico SNT. They concluded that the spectral index is around 3 assuming a power

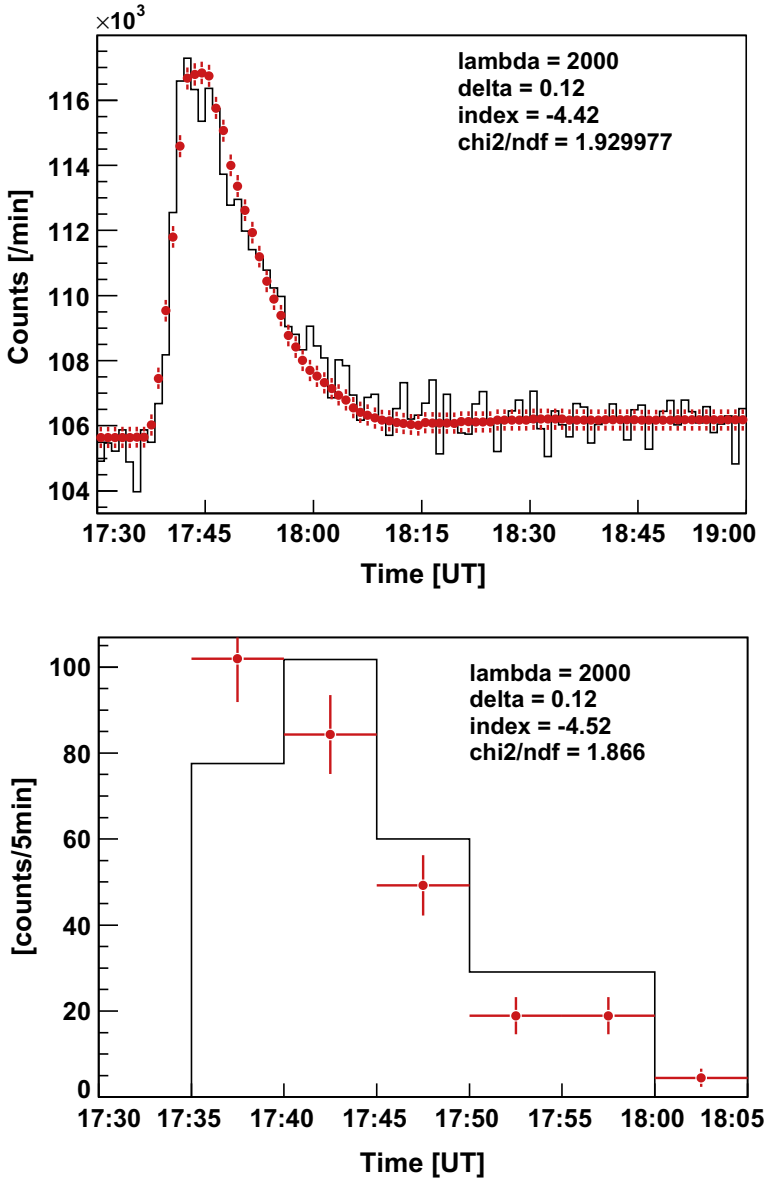

Figure 1.14: Top: Time profile of neutrons detected by the Bolivia NM. The black line means the count rates of the Bolivia NM. The red dots are results calculated from the transport and interaction model by Hua. Bottom: 2.2 MeV gamma-ray line detected by INTEGRAL on 2005 September 7. The black line represents the observed 2.2 MeV gamma-ray line. The red dots are the best fitted plots. These calculations are performed by Watanabe et al. (2009)

law spectrum, and it is consistent with previous independent studies mentioned above. Their calculation implies that the energy of neutrons might have attained to 1 GeV, which corresponds to 10 GeV protons at the Sun. These energetic protons have not been observed on the Earth, because the active region was located at the eastern limb of the Sun. This paper discussed about the particle acceleration capability of the solar flare based on the detection of solar neutrons for the first time.

Another important solar neutron event was registered in association with the M6.5-class solar flare on 2014 July 8. The enhancement was recorded by two ground-based detectors in Mexico and Bolivia. At that time, the enhancement was also detected by the NEM onboard the International Space Station simultaneously. As a consequence of the analysis, Muraki et al. (2015) suggested that the production mechanism of neutrons cannot be explained by a single model: one of the enhancements may be explained by an electric field generated by the collision of magnetic loops and the other by the shock acceleration mechanism at the front side of the CME.

1.4 Overview of this thesis

As discussed in Section 1.3, previous studies revealed that the emission of solar neutrons is not an impulsive but a long duration emission in the case of the most significant event on 2005 September 7. This is the only event which puts constraints on the emission of solar neutrons. It was not allowed to study the energy spectrum of neutrons and the emission time of neutrons separately, because of fewer statistics of neutrons for other events. For obtaining more statistics of solar neutron events and further information on the emission of solar neutrons, the SciBar Cosmic Ray Telescope (SciCRT) was deployed at the top of Mt. Sierra Negra (4,600 m) in the middle of Mexico in 2013. However, the sensitivity of the SciCRT was significantly limited by the dead time of its readout electronics.

This thesis aims to realize the full performance of the SciCRT by developing and installing a new DAQ system for fast readout and more reliable system for our observation. It is expected that 10 times smaller events than before could be detectable by the SciCRT. This also indicates that rich information about the time and the energy of solar neutrons will be given if solar neutron events with the same flux as the previous event's one is observed.

It should be confirmed that the SciCRT at full performance can unlock

the degeneracy problem between the arrival time and energies of solar neutrons. It is expected that the instantaneous emission and the long duration emission exceeding 10 minutes can be discriminated considering more than 20 minutes emission such as the event on 2005 September 7. The difference of the power-law index of the energy spectrum should be determined within an accuracy of $\pm$ 1.0 at least. This is because the power-law index differs more than 1.0 between the shock acceleration and the stochastic acceleration.

This thesis is composed as follows. In Chapter 2, I give a review of the SciCRT including its concept and a design of the detector in detail. Chapter 3 describes the development of fast readout new back-end boards (BEBs) based on SiTCP. The assembly of new BEBs and the deployment of the new DAQ system are also described in the chapter. Chapter 4 describes the sensitivity studies of the SciCRT with the new DAQ system to the emission of solar neutrons. The conclusion of this thesis is finally described in Chapter 5.

Chapter 2

SciBar Cosmic Ray Telescope (SciCRT)

2.1 Concept of a new solar neutron telescope

As mentioned in Chapter 1, we have got only 10 solar neutron events up to date. Except for the information obtained by the 2005 September 7 event, the number of events and the statistics of neutrons are not enough to discuss about the ion acceleration mechanism using the energy spectrum obtained from data. For increasing the statistics of significant solar neutron events such as the 2005 September 7 event, it was suggested to install a new solar neutron telescope which improves the function of SNTs, i.e. the capability for energy measurement and determination of the arrival direction of solar neutrons with high detection efficiency. Sako et al. (2003) suggested a new type of solar neutron telescope as the Super Solar Neutron Telescope (SSNT) as shown in Figure 2.1.

All the three independent functions (target scintillator, anti counters, and directional detection counters) of the SNT are packaged in the bulk of plastic scintillators. Sako et al. (2003) pointed out current problems of the observational method used in the SNT. The left of Figure 2.2 shows a method of the measurement of the direction in the SNT. In the case a of the figure, the direction of neutron-induced protons could be reconstructed by tracking the location of PRC layers into which the particles penetrate underneath the scintillator . But in the case b, its track is too short to reconstruct the arrival direction. Furthermore, the multiple scattered particles in a case c make a misidentification of the direction, because both patterns are identified and registered as two different events.

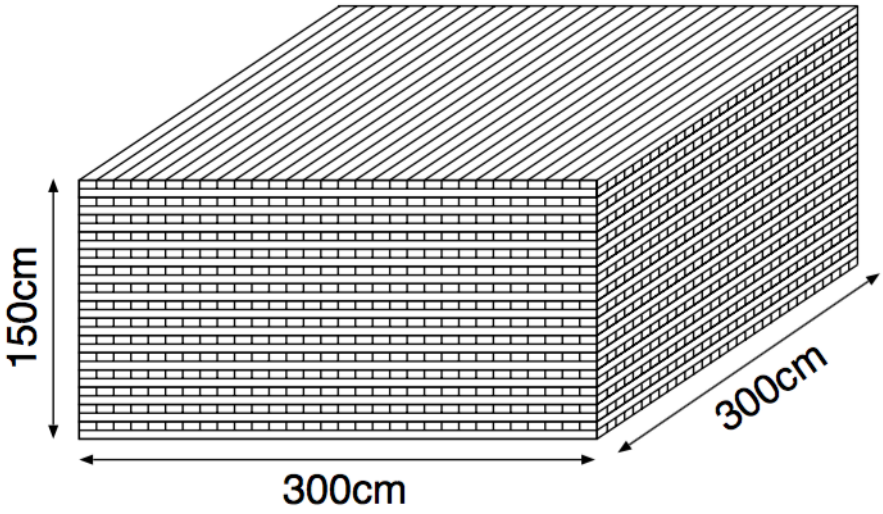

Figure 2.1: Schematic view of the Super Solar Neutron Telescope (Sako et al., 2003). It consists of scintillator rods with dimensions of 5 cm × 10 cm × 300 cm.

The concept of the new telescope is discussed in Sako et al. (2003). They use many rods of a plastic scintillator with dimensions 5 cm × 10 cm × 300 cm. A plane which consists of horizontally aligned scintillators is orthogonally attached, and such planes act as a three dimensional tracker. Even in a case b, it may be possible to determine the direction. In the paper, they put a trigger condition to penetrate at least four scintillator layers, which corresponds to the energy threshold 150 MeV.

The capability of energy measurement will be improved by using this plastic scintillator tracker with more intelligent readout electronics. If energy deposit of recoil protons is recorded by some ADC (Analog to Digital Converter), we can know the track shape and the energy deposit in each scintillator. It makes off-line analysis more flexible and the signal-to-noise ratio will be improved consequently. As long as all triggered tracks are recorded in data, the case c is successfully judged by off-line analysis.

The use of plastic scintillators in anti counters also enhances the rejection power for charged particles, because of the PRC's low conversion efficiency and the dead area of the cylinder type PRC. Gamma rays pass through anti PRCs without any interactions; therefore, these are the dominant back-

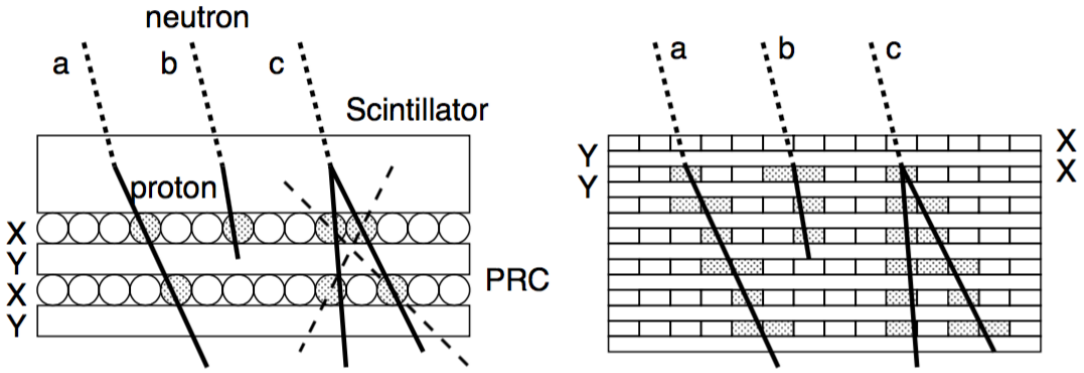

Figure 2.2: Methods of the direction measurement of neutron-induced protons (Sako et al., 2003). Left: Method of the direction measurement used in SNTs. Right: Method of the direction measurement in plastic scintillator rods suggested in Sako et al. (2003). The detailed explanation is described in the text.

ground components in SNTs unless leads are put on the PRCs. The plastic scintillator tracker has a capability to reject the background particles (muons and gamma rays) by means of a combination of the robust anti counters and off-line analysis.

2.2 A review of the SciBar detector

The SciBar detector was constructed for the world's first long baseline neutrino oscillation experiment (K2K) in Japan and used in the SciBooNe (SciBar Booster Neutrino Experiment). Our group was allowed to use this detector as a new solar neutron telescope by the grace of the K2K-SciBar group and the SciBooNe group. I describe the configuration and each component of the detector in this section.

The structure of this detector is quite similar to that of the SSNT. Figure 2.3 illustrates a schematic drawing and description of the SciBar detector. The detector size: 3 m $\times$ 3 m $\times$ 1.7 m (14.3 m^3) is bigger than the SSNT's. Each scintillator bar has a dimension of 1.3 cm $\times$ 2.5 cm $\times$ 300 cm. The total channel number is 14,848. Therefore, the SciBar is more massive and more fine-segmented detector than the SSNT.

The specification of each component in the SciBar detector is summarized

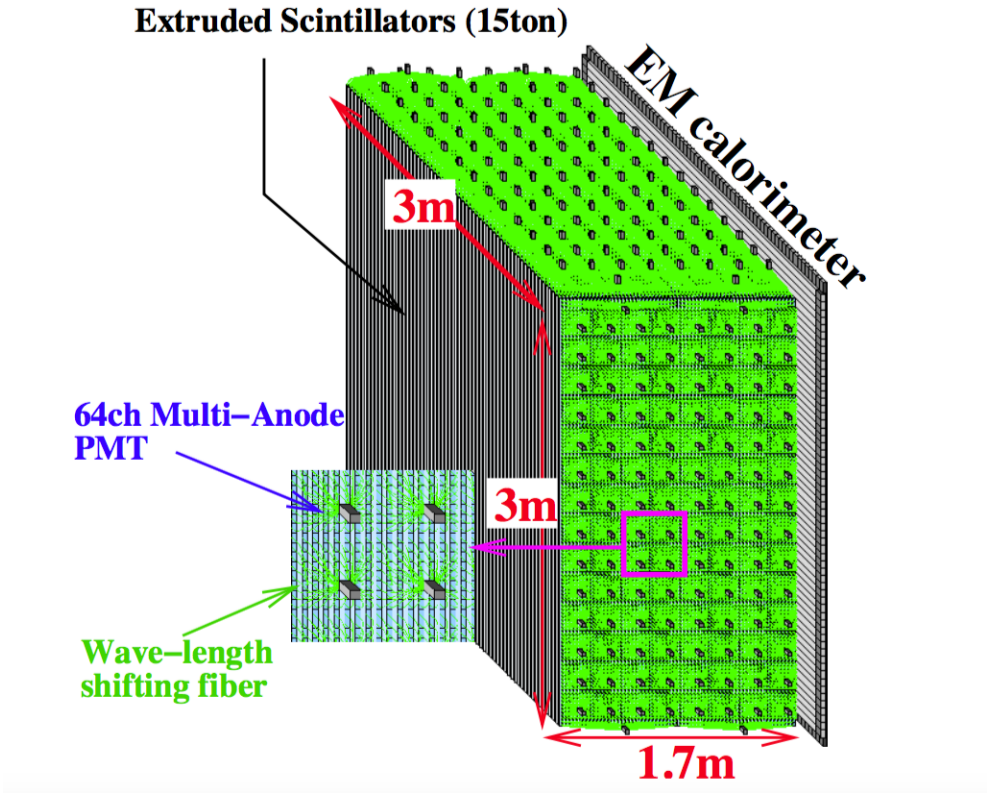

Figure 2.3: Schematic drawing and description of the SciBar detector (Maesaka et al., 2005).

Table 2.1: Specification of each component of the SciBar detector (Nitta et al., 2004).

Structure	Dimensions	3 m (horizontal), 3 m(vertical), 1.7 m(thickness)
	Weight	15 tons
	Number of strips	14,848
	Number of PMTs	224 (+OD:8)
Scintillator	Material	Polystyrene, PPO (1%) and POPOP (0.03%)
Strip	Size	1.3 cm (thickness), 2.5 cm (width), 300 cm (length)
	Weight	1 kg
	Coating	0.25 nm (TiO_2)
	Emission length	420 nm (peak)
	Density	1.021 g/cm^3
Fiber	Diameter	1.5 mm Φ
	Reflective index	1.59 (outer)/1.50 (middle)/1.42 (inner)
	Absorption length	430 nm (peak)
	Emission length	476 nm (peak)
PMT	Model	H8804
	Cathod material	Bialkali
	Anode	8×8 (2×2 mm^2/pixel)
	Wave length sensitivity	300-650 nm (Max 420 nm)
	Number of dynode stages	12
	Gain (@800 V)	3×10^5
	Quantum efficiency	21% at 390 nm
DAQ	Shaping time	80 nsec (TA), 1.2 μs (VA)
	Pedestal width	0.03 MeV
	Linearity	5% at 30 MeV
	Dynamic range	0.1-30 MeV

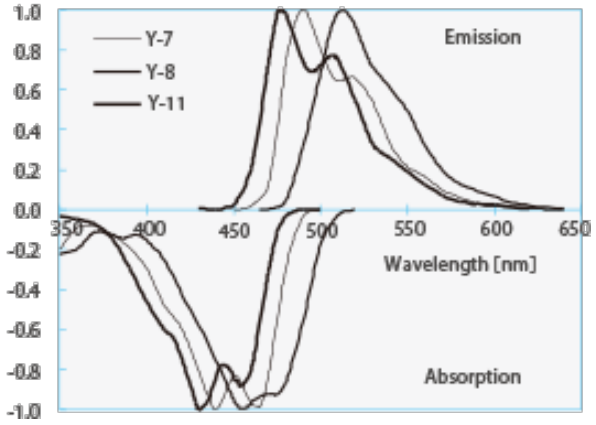

Figure 2.4: Emission and absorption spectra of the wavelength shifting fiber, Y11(200)MS, made by Kuraray. The black thick curve is the spectrum of Y11 series. The absorption peak corresponds to 430 nm, and the emission peaks at 476 nm. Available at: <http://kurarayпsf.jp/psf/ws.html> [Accessed 2016 December 2]

in Table 2.1. The detail of the detector is written in Nitta et al. (2004). Here I describe a brief review of the detector components.

The extruded scintillator bar is made of polystyrene with PPO (1%) and POPOP (0.03%), and these components are same as used for the MINOS experiment. A peak of the emission spectrum is about 420 nm. It is coated with titanium based reflector (TiO_2) with 0.25 mm thickness to enhance the collection efficiency. Each of 116 scintillator bars is arranged in a same plane. A combination of two planes orthogonally attached is called a layer.

The scintillator bar has a hole (a diameter of 1.8 mm) to insert a wavelength shifting fiber which is multi-clad type, Y11(200)MS made by Kuraray. Figure 2.4 shows a relation between the emission and absorption spectra of the WLS fiber. The attenuation length of all fibers inserted to the SciBar is estimated before and after installation to the K2K. The average value of measured all fibers was around 350 cm (Nitta et al., 2004). To adjust a contact between a Multi Anode Photo Multiplier Tube (MAPMT) and WLS fibers, 64 WLS fibers are bundled using a jig called as a cookie developed by Kyoto University.

Multi Anode Photo Multiplier Tubes (MAPMTs H8804) made by Hama-

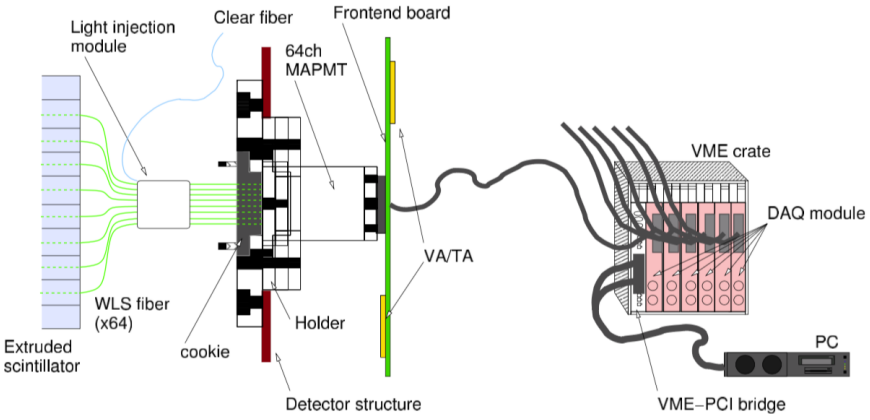

Figure 2.5: Schematic view of the readout system of the SciBar (Maesaka et al., 2005). Sixty-four bundled WLS fibers are inserted into 64 extruded scintillators, and scintillation photons of these fibers are readout by a 64-channel MAPMT. Signals from the MAPMT are dealt with a Front-end board with which VA/TA chips are equipped. The VA/TA FEB is connected to a DAQ module (BEB) in the VME crate. BEBs are controlled by the PC.

matsu Photonics are used as photon sensors of the SciBar detector. The photocathode is divided into sixty four (8×8) with each area of 2×2 mm^2. The sensitive wavelength ranges from 300 to 650 nm, and the peak is about 420 nm. The gain is suppressed in low level (about $6{\times}10^5$) using an external amplifier. The maximum gain channel has three times higher gain than the minimum gain channel on a MAPMT. Since one high voltage value is assigned to each MAPMT, it is important to keep high voltage values of all MAPMTs as constant as possible so that the high linearity must be kept. The crosstalk on the photocathode is suppressed within about 3% by using the cookie.

A Front-End Board (FEB) is directly attached to the MAPMT. A combination of VA32HDR11 and TA32CG (VA/TA) developed by IDEAS is packaged to an Application Specific Integrated Circuits (ASIC), and two ASICs are employed to the FEB. The VA is a VIKING chip developed for a low noise Si-strip detector based on CMOS technology. It has charge sensitive preamplifiers, slow shaper amplifiers and sample&hold circuits for inputs of 32 channels respectively. Each output line from 32 channels is passed to an analog multiplexer. The slow shaper has the peak time ranged from 0.8 to 1.2 μsec. The hold timing is controlled by a Back-End Board (BEB). The VA

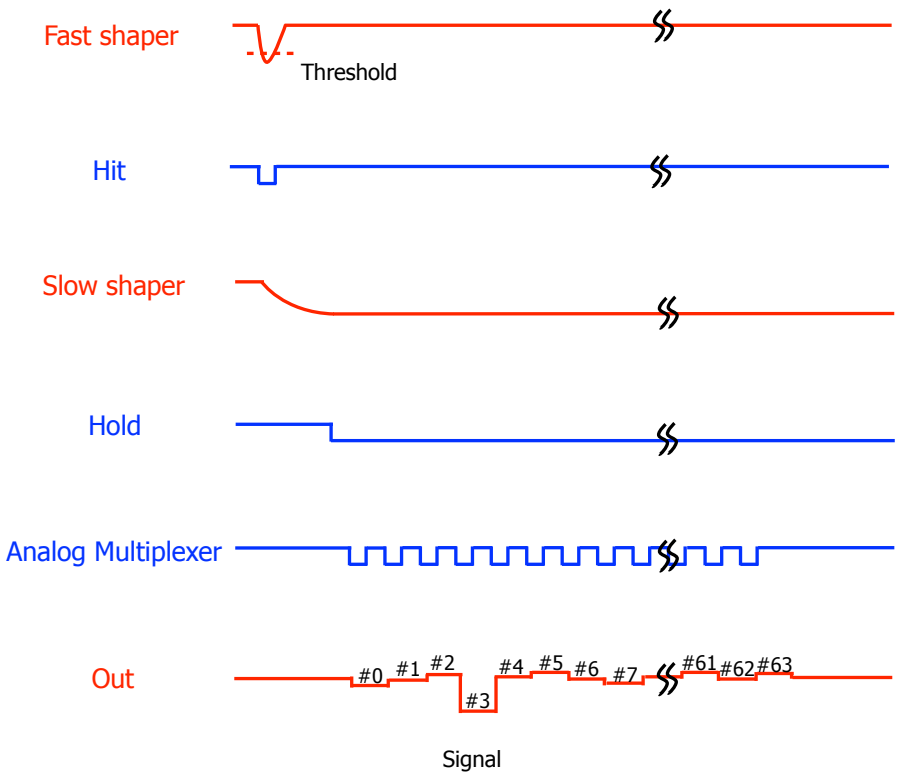

Figure 2.6: Basic function of the VA/TA chip. The red characters mean analog signals, and the blue characters are digital signals. The detailed descriptions are written in the text.

readout speed is determined by a frequency of the analogue multiplexer. The output voltages of 64 channels are sequentially readout by the daisy-chain connection between two ASICs. Then the VA is connected to the MAPMT by AC coupling.

On the other hand, the TA has a fast triggering function. A trigger signal is generated through a fast shaper followed by a level sensitive discriminator for 32 multi-channel inputs. The time constant of the fast shaping amplifier is about 70 μsec. Trigger signals from 32 channels are sent to a OR circuit so that one trigger pulse is generated from the TA.

One BEB can control eight FEBs simultaneously and digitize voltage output from the VA. This was developed as VME 9U size board. Since the BEB

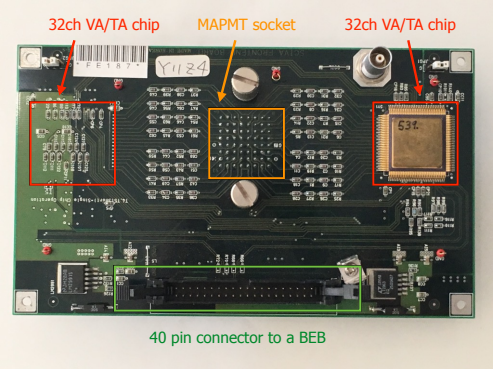

Figure 2.7: Picture of a FEB.

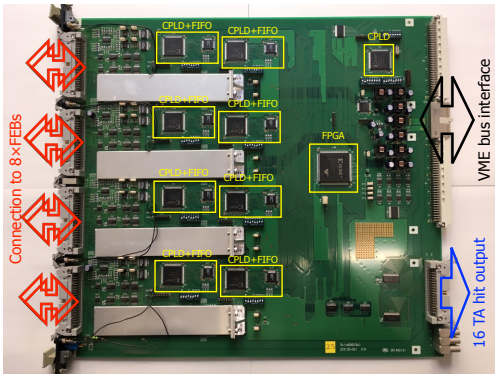

Figure 2.8: Picture of a BEB.

drives analog signals from the VA through a distance of 4 m, these signals are easy to be affected by noise. Therefore a shielded twisted-pair cable is used for the connection between the BEB and the FEB. The BEB receives output from the VA as differential signals through 150Ω registers which is higher than the impedance matching register with the cable (100Ω). A 12bit Flash Analogue to Digital Converter (FADC) which has a sampling speed with 10 MHz is employed on the BEB. Note that a peak hold technique is used for sampling output from VAs for each channel. Although the dynamic range of the FADC is from 0 to 5.0 V, an offset voltage (+2.5 V) is given to detect both positive and negative charges. Therefore the actual dynamic range is equal to 11bit.

The discrimination level of the TA is controlled by a digital to analog converter (DAC), MAX525 made by Maxim Integrated, equipped on the BEB. As well as polarity of the FADC, it is required to provide the bipolar threshold to the DAC. Actually the DAC can output ±2.0 V. By controlling various load modes (written in a datasheet of MAX525) of the DAC, it is possible to assign different values to each TA on the FEB.

Power is supplied to BEBs from a VME crate, and ±5 V, 2.5 V and 3.3 V are produced by regulators on BEBs. After ±5 V power is sent to FEBs, the voltage is dropped to ±2.5 V on FEBs.

One FADC and eight combinations of a Complex Programmable Logic Device (CPLD) and a First In First Out (FIFO) memory are implemented on the BEB, and the Field Programmable Gate Array (FPGA) controls the readout sequence of eight FEBs and the VME transmission sequence between

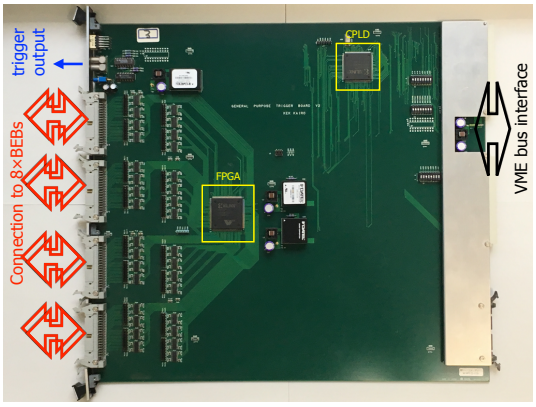

Figure 2.9: Picture of the TRGB.

other CPLD which controls VME bus interface.

Two trigger conditions were used for data taking of the SciBar. The self trigger mode is used for neutrino data whereas the external trigger mode is for cosmic rays. Regarding the external trigger mode, hit signals from FEBs are sent to a Trigger Board (TRGB). A Field Programmable Gate Array (FPGA) is implemented on the TRGB. Therefore, a variety of hardware trigger conditions can be realized. This was used for taking cosmic-ray data for energy calibration in K2K. Figure 2.9 shows the TRGB, a GNV-210 VME 128CH trigger module, which can control eight BEBs in the maximum case. Finally, trigger signals from the TRGB are used for informing the hold timing of the VA on the FEB.

The timing information is processed and recorded by a 64ch multi-hit TDC. This was used in K2K, but it is not used for our solar neutron observation. We also do not use the Electron Catcher (EC) which measures the electron neutrino contamination in the beam and π^0 production events. The description of the TDC is found in Nitta et al. (2004).

2.3 SciBar detector as a new solar neutron telescope: SciCRT

After the K2K was finished in 2004, the detector was transported to the FNAL (Fermi National Accelerator Laboratory) in Chicago, USA. The SciBooNE (SciBar Booster Neutrino Experiment) began running in 2007 and completed its run in 2008. In 2011, the SciBar detector was transported

Figure 2.10: Place of two sites, Instituto Nacional de Astrofísica, Óptica y Electrónica (INAOE) and Sierra Negra volcano in the middle of Mexico (Available at: <https://www.google.com/maps> [Accessed 2017 January 11]). The left red flag is the place of INAOE, and the right flag is the location of Mt. Sierra Negra.

to the Instituto Nacional de Astrofísica, Óptica y Electrónica (INAOE) in Mexico. Eventually, it was installed at the top of Mt. Sierra Negra (about 4,600 m) in April, 2013. We use the detector for cosmic-ray observation and call it "SciBar Cosmic Ray Telescope (SciCRT)".

The beam injection surface of the detector is directed to the zenith. Since the deflection of the bulk of scintillator bars influences the alignment, the detector is supported by a metal frame. This was tested in INAOE. Figure 2.11 shows the detector supported by the frame. Regarding this test, see the Appendix A in Nagai (2014).

The SciCRT consists of two functional parts. One part, the top layer and the bottom layer (muon layers), are used as a muon detector. This also functions as active veto counters to charged particles. The other part (the central tracker) is divided into eight Super Blocks (SBs). They are arranged from top to bottom as SB1 to SB8. Every SB consists of eight layers, each with a dimension of $20.8 \times 300 \times 300$ cm^3. Since neutrons are neutral particles, we obtain energy information on neutron-induced protons produced by a nuclear interaction between neutrons and materials in the target scintillator.

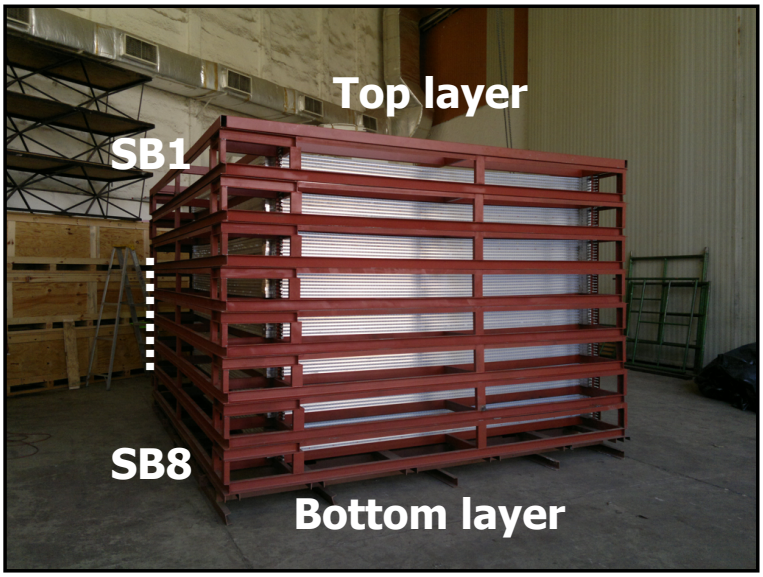

Figure 2.11: An image of the SciCRT detector taken at Instituto Nacional de Astrofísica, Óptica y Electrónica (INAOE). Scintillator bars are contained by an iron-based structure for supporting the weight of all bars. The detector is functionally divided into two detection parts. One, the top and the bottom layers, are employed for the muon selection and the charged veto counters to the other part. The other part, the central tracker, is divided to eight blocks called Super Blocks (SBs). Neutrons are detected using the central target, eight SBs.

Neutron-induced protons are read out as three-dimensional trajectories from two sides (X and Y). The DAQ system works for each SB independently, because neutron-induced protons rarely penetrate across two SBs.

Nagai (2011) pointed out that the BEB causes dead time about 1 msec/BEB, when ADC data are read out by VME bus. Owing to the dead time, it is impossible to obtain ADC data of all the neutrons, because the rate of background neutrons is very high at such a high mountain. For the sake of minimizing the influence of the dead time, it is necessary to consider about the alignment of the FEB and the BEB.

Since a hit signal is produced from the bulk of 32 scintillator bars, too complex trigger logic can not be implemented on the FPGA of the TRGB. An order of the 32 scintillator bars corresponding to one TA in muon layers and one SB is shown in Figure 2.12. The trigger condition is made by a combination of these hit signals using logical AND and OR.

As explained in the following text, a coincidence between X and Y sides is used for the trigger condition of ADC data in SBs, and ADC data are read out at both X and Y sides simultaneously. Therefore, one BEB is connected to seven FEBs overlapping both sides. As shown in Figure 2.12, one SB is separated to four regions, and one BEB takes charge of one region.

Trigger and the DAQ system

Figure 2.13 shows the signal flow of the DAQ system of the SciCRT based on the SciBar's electronics. The function of the FEB and the BEB is same as that used in the SciBar described in Subsection 2.2. The trigger condition is originally studied for our observation in Nagai (2014). I will summarize the data acquisition condition, the DAQ system, and data sets in the SciCRT.

The data acquisition condition is determined by three parameters: a combination of hit signals for obtaining ADC data (i.e. trigger condition), the energy threshold level, and a combination of anti counters (i.e. anti trigger condition). The trigger condition is determined by simulating the solar neutron event on 2005 September 7.

The trigger condition is a coincidence between X and Y sides, (Xup and Yup) or (Xdown and Ydown). This is because ADC data are used to trigger longer and higher energy tracks of neutron-induced protons.

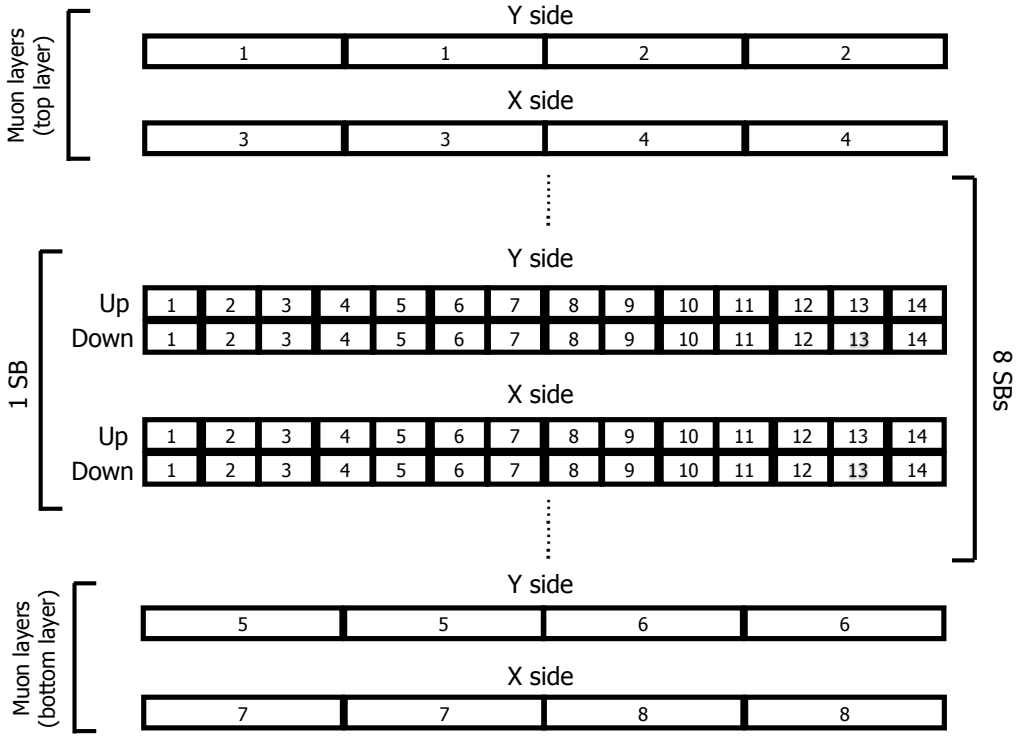

Figure 2.12: The region of 32 scintillator blocks to which one TA chip corresponds in muon layers and one SB of the SciCRT. The number of each block in muon layers and the SB means the serial number of MAPMTs.

Table 2.2: Correspondence between the FEB and the BEB in muon layers and SB1-4. In muon layers, "T" and "B" mean top and bottom layers, respectively. This table is related to the alignment of the MAPMT shown in Figure 2.12.

Number	Address								
muon layers		1	2	3	4	5	6	7	8
BEB1	0x1301	TY1	TY2	TX3	TY4	BY5	BY6	BX7	BX8
TRGB1	0x1401								
SB1-3		1	2	3	4	5	6	7	8
BEB1	0x1301	X1	X2	X3	Y1	Y2	Y3	Y4	
BEB2	0x1302	X4	X5	X6	X7	Y5	Y6	Y7	
BEB3	0x1303	X8	X9	X10	Y8	Y9	Y10	Y11	
BEB4	0x1304	X11	X12	X13	X14	Y12	Y13	Y14	
TRGB1	0x1401								
SB4		1	2	3	4	5	6	7	8
BEB3	0x1306	X1	X2	X3	X4	Y1	Y2	Y3	Y4
BEB4	0x1307	X5	X6	X7	X8	Y5	Y6	Y7	Y8
BEB5	0x1308	X9	X10	X11	X12	Y9	Y10	Y11	Y12
BEB6	0x1309			X13	X14			Y13	Y14
TRGB1	0x1401								

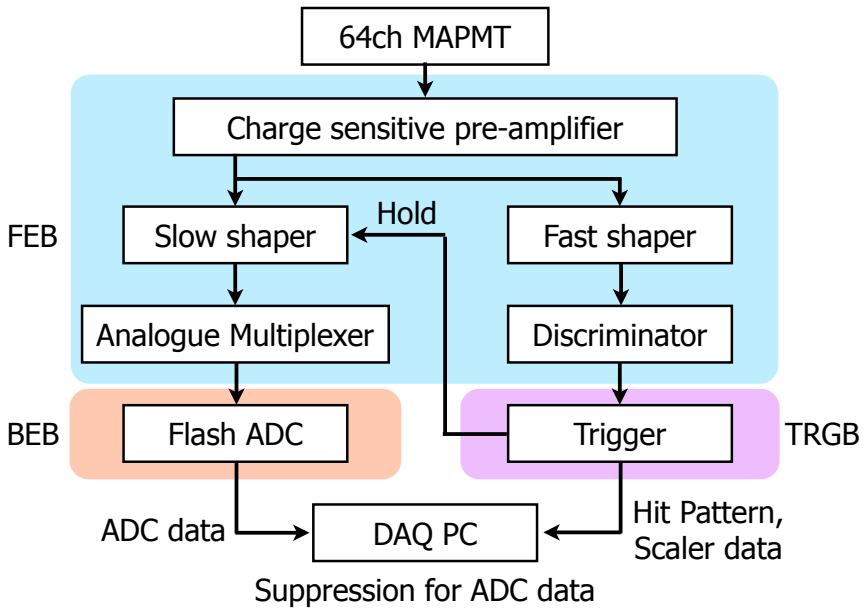

Figure 2.13: DAQ overview of the current SciCRT based on the SciBar electronics with minimum elements.

Table 2.3: The calculated significance of solar neutrons for neutron ADC data and neutron scaler data (Nagai, 2014). These significances are calculated for the threshold energy from 1 MeV to 13 MeV.

threshold (MeV)	1	2	3	4	5	6	7	8	9	10	11	12	13
Neutron ADC (σ)	2.28	2.23	2.60	3.03	3.47	3.56	3.53	3.20	2.86	2.46	2.18	1.92	1.55
Neutron scaler (σ)	13.1	15.1	15.5	15.9	16.7	17.4	17.5	17.3	16.8	16.1	15.2	14.3	13.1

Table 2.4: The rejection rate of some anti trigger patterns. The first line shows the count rate of each particle per 30 seconds and the significance of solar neutrons in the case of no anti trigger condition. From the second line to the bottommost line, the rejection rate and the significance for each anti trigger logic are illustrated.

	charged particles	neutrons	γ-rays	solar neutrons	significance
total count	63438	111592	30939	4952	10.783
top or side or bottom	0.922	0.321	0.479	0.273	11.360
top or side	0.913	0.305	0.451	0.264	11.323
top or bottom	0.670	0.145	0.246	0.142	11.197
top	0.579	0.117	0.191	0.130	10.955
four fold	0.073	0.001	0.007	0.000	10.913

The energy threshold level is determined so that the signal-to-noise raito of solar neutrons are most significant. Table 2.2 is results of the calculated significance of solar neutrons to neutron scaler/ADC data for each threshold energy ranged 1-13 MeV. Here we define that neutron scaler data are the sum of hit signals from all the MAPMTs without any coincidence of anti signals, and neutron ADC data are ADC data obtained when the trigger condition is satisfied without any coincidence of anti signals. As a consequence, the highest significance is obtained for both neutron scaler/ADC data at 7 MeV. Note that this value corresponds to the energy deposit in one scintillator strip.

The anti counters consist of top, bottom, and side layers. The anti counter condition is made by a combination of these layers. Table 2.3 shows the significance of solar neutrons and the rate of rejection power to charged particles for some combinations of layers. Although the side counter is not used in the SciCRT, it seems the significance of "top or bottom" is not so different from that of "top or side or bottom". Charged particles penetrating from the side surfaces will be rejected by off-line analysis.

As shown in Figure 2.13, the hit pattern is registered by the TRGB and sent to the DAQ PC via VME bus interface. When ADC data are sent to

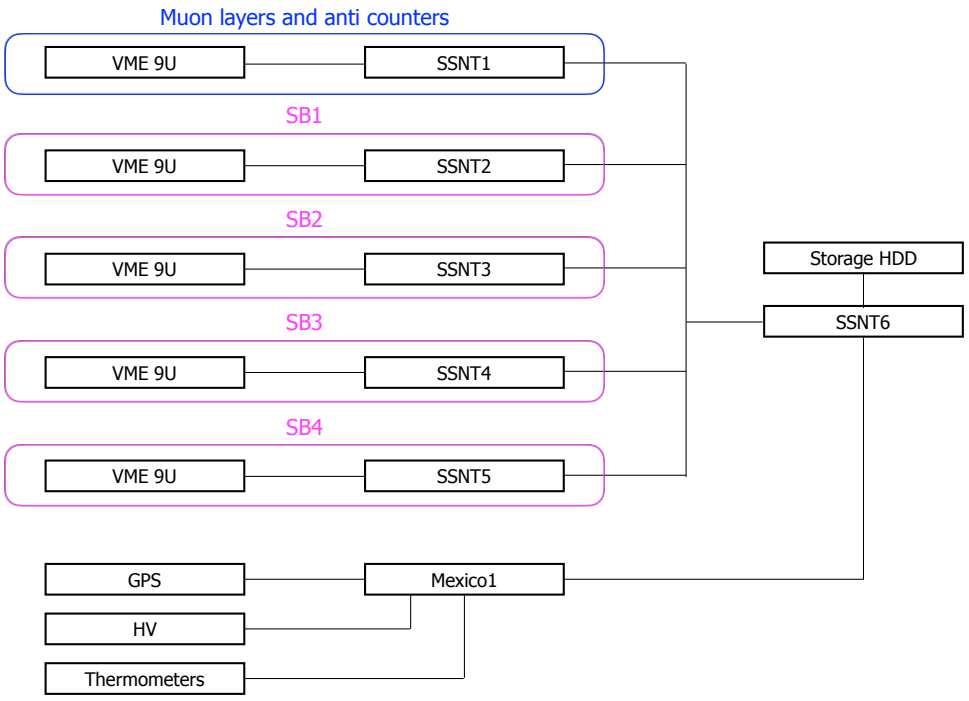

Figure 2.14: Configuration of VMEs, servers, environmental monitors of the SciCRT. The servers are named SSNT1-6 and Mexico1.

the DAQ PC, only the data of 32 scintillator bars which output hit signals are recorded in the storage. This is the suppression of ADC data.

Figure 2.14 shows the configuration of servers and environment monitors. SSNT1-5 corresponds to muon layers and SB1-4, respectively. These servers are controlled by a central server, SSNT6. Data obtained by each server are sent to SSNT6 and stored to portable hard disks. A high voltage power supplier (HV), a GPS receiver, and thermometers are managed by a server named Mexico1. The GPS is used for synchronization between the absolute time and the server local time.

The data sets

The SciCRT obtains three categories of data sets, namely, muon ADC data, neutron ADC data, and neutron scaler data. Each data set is ex-

plained briefly in the following.

Since high energy cosmic-ray muons penetrate through the SciCRT from the top to the bottom, a 4-fold coincidence condition is applied using each side (X and Y) of top and bottom layers. At the 4-fold coincidence timing, the muon ADC data is read out from eight MAPMTs and recorded into a data file. The threshold level is set to around 0.7 MeV on muon layers. This corresponds to about 0.3 Minimum Ionizing Particle (MIP). Anti signals are also generated from a combination of OR'ed four layers and are used for both neutron ADC data and neutron scaler data.

The SciCRT detects neutrons using two different trigger conditions. They are recorded as a neutron ADC data and a neutron scaler data. We set the neutron ADC trigger condition to obtain long proton tracks generated by high energy neutrons using a combination of X and Y with anti signals as veto to charged particles. Since it is difficult to reconstruct the trajectory of protons induced by low energy neutrons, these are recorded as the neutron scaler data using the sum of hit signals which are output from each TA with anti signals. The neutron scaler data is recorded every 10 seconds, and return value from counters is recorded for each TA. The neutron scaler data is sensitive to low energy neutrons compared with the neutron ADC data. In every SB the neutron threshold is set to 7 MeV. This corresponds to about 3 MIP. The current trigger condition and the threshold were determined by our Monte Carlo simulation (Nagai et al. 2014 and Nagai 2014).

Performance of the SciCRT

The performance was tested by several analyses using cosmic-ray muons in INAOE at an altitude of 2,150 m. The detail can be found in Nagai (2014).

After the SciCRT was installed at the top of the Mt. Sierra Negra, the gain and the threshold level were adjusted in muon layers and SBs. Regarding the gain: one voltage value is given to one MAPMT. An energy threshold level is assigned to each TA. Both parameters are ordinary fixed by obtaining muon events at Sierra Negra. The gain was adjusted so that the MIP peak was 300 and 14 ADC counts for muon layers and SBs, respectively. In Figure 2.15, the red distribution shows the stacked data when the maximum energy is deposited in one scintillator plane for each muon event, whereas the black distribution shows the sum of the ADC data for all 64 channels. In terms of the red distribution, it is easy to find the peak by fitting. The same method

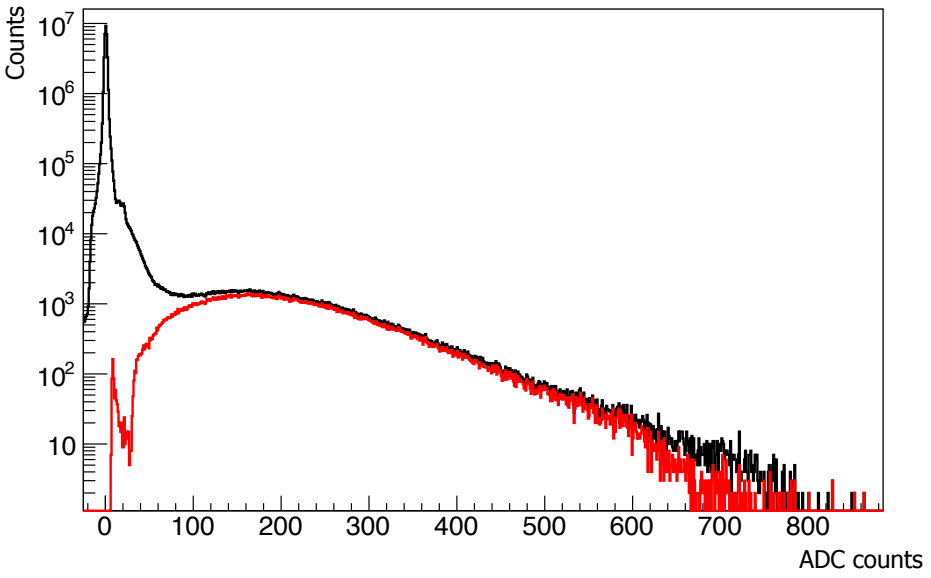

Figure 2.15: ADC distributions of the MAPMT No.3 which is located at the left position of the side X in the top layer. The black distribution includes all the 64 channel ADC data. The red one is a distribution of the ADC data recorded for the channel where the maximum energy is deposited in one scintillator plane. The peak of the red one is normalized to that of the black one.

is applied to SBs. The red distribution is derived from the same method used as used in muon layers. However, it is difficult to find the MIP peak from the pedestal overlapping distributions. Therefore, an additional criterion is applied to the red distribution: a discrepancy with two planes on upper and lower to a focused plane must be less than two scintillator strips. The result after the new criterion was added is the green distribution in Figure 2.16.

After the calibration was finished at Mt. Sierra Negra, the continuous operation began using muon layers and three SBs (SB1-3) in September 2013. An example of the neutron-induced proton like event is displayed in Figure 2.17. In the middle of 2014, it was found that many fake triggers cause an increase of shower like events in muon layers. This was induced by a leak of light, especially from a gap where many FEB-BEB cables are bundled. An extension cable was additionally installed to a part of the FEB-BEB cables, and the dark sheet was strengthened for filling the gap.

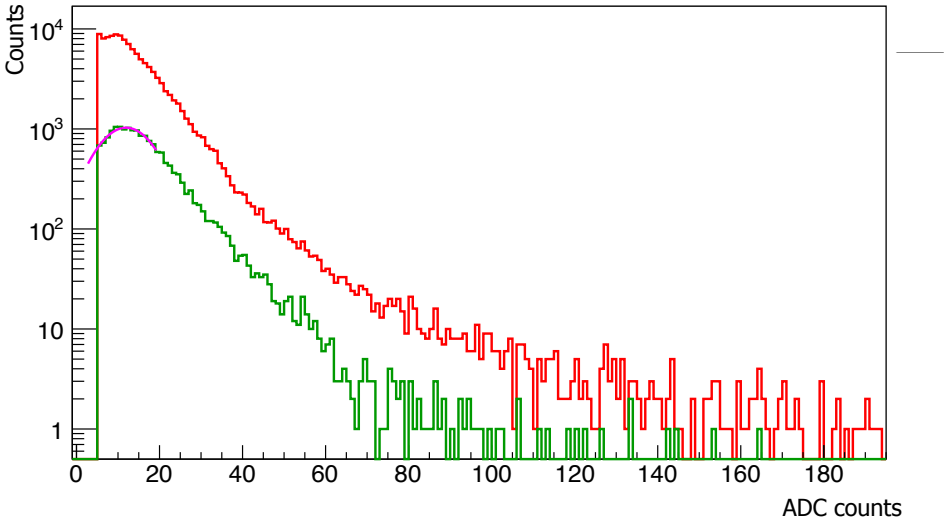

Figure 2.16: All channel summed ADC histograms of the MAPMT located at X1 in SB1 (Nagai, 2014). The green histogram is the ADC data recorded where the maximum energy is deposited in one scintillator plane of the side X. The pink curve is a result of the gaussian fitting.

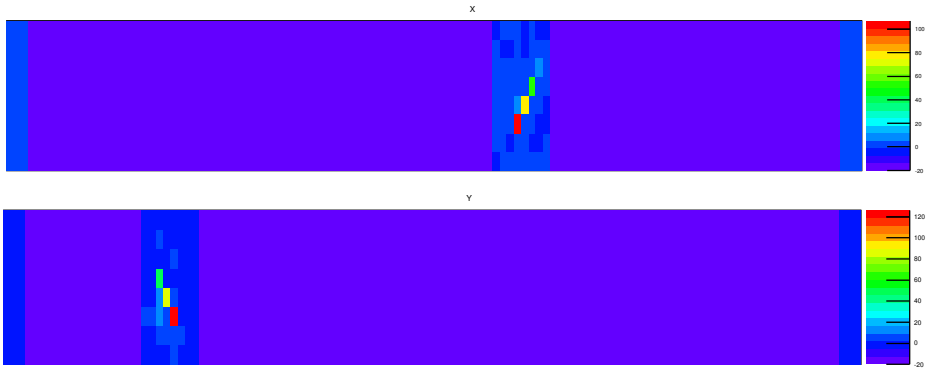

Figure 2.17: Trajectory of a neutron-induced proton from a view of both X and Y sides.

Chapter 3

Development of the new DAQ system of the SciCRT

3.1 Motivations and Requirements to the new DAQ system

As mentioned in Chapter 2, there is a fatal problem with the dead time when ADC data are acquired. To solve this problem, a brand-new BEB was developed to upgrade the DAQ system. In this section, I describe a couple of problems including the dead time, and requirements to the new DAQ system in detail.

Dead time of neutron and muon ADC data

The long dead time occurs event by event while ADC data are processed. It takes about 1.2 msec to acquire ADC data per one BEB; thus, the maximum transfer speed is limited to about 1 kHz in muon layers. This constraint comes from a combination of the BEB and the VME bus. One BEB is used to read out in muon layers, and the readout rate is limited to about 1 kHz. Regarding SBs: neutron ADC data are read out by typically two or three BEBs per one event. The dead time further increases when ADC data are read out for multiple BEBs, because ADC data are read out by each VME crate unit. The readout rate of neutron ADC data is limited to a few hundred Hz.

Influence of VME readout noise to neutron scaler data and neutron ADC data

VME readout noise influences the transmission line of hit signals in the BEB while ADC data are read out. Due to this problem, it is impossible to count the number of neutron scaler events correctly while ADC data are read out. Therefore, there is no choice but to inactivate a function of scalers while ADC data are read out. Moreover, a live time of the anti counter is limited, because the VME readout noise also occurs in the transmission line of anti signals when ADC data are read out in muon layers. Signals from the anti counter are forcibly set to be high as if charged particles are continuously injected during the readout term.

Environmental problems at observation site

The new DAQ system should be optimized for our environment condition (4,600 m a.s.l.), which was not taken into account in the accelerator experiment. Especially, electronics holds the heat at such a high altitude environment. The SciCRT always runs under an unmanned operational mode. Therefore, it is required to reconfigure firmwares remotely whenever we want to change the data acquisition flow, the trigger condition, and the readout routine. Furthermore, a single event upset (SEU) may occur due to its high frequency of cosmic rays.

Requirements of the new DAQ system

As stated above, the trigger rate of neutron ADC data are influenced by the dead time and the readout noise by the VME bus, increase of the dead time by readout of multiple BEBs, and decrease of live time of the anti counter by the VME readout noise. Therefore, the trigger rate is limited to about 260 Hz in maximum for one SB. The actual averaged trigger rate is limited to about 123 Hz. Assuming a new BEB which has the 10 times faster readout rate and are free from the VME readout noise, the trigger rate will increase up to about 400 Hz for one SB. Under the current situation, the influence of the dead time makes the ratio of solar neutrons to background particles lower relatively, because the proportion of background particles is quite higher than that of solar neutrons. Figure 3.1 shows the significance of solar neutrons to background particles for two cases: the current situation and the new situation using the ideal BEB. It is evident that the significance of solar neutrons under the new situation reaches the almost ideal

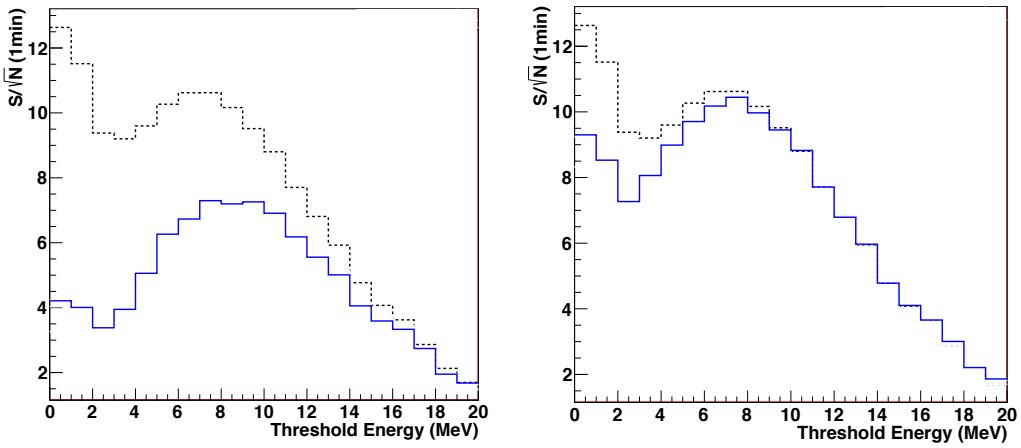

Figure 3.1: Significance of solar neutrons to background particles for threshold energies 0-20 MeV for one minute. The black dotted curve simulates an ideal situation which has no dead time of electronics. The blue curve shows the significance assuming the current situation and the new situation (10 times faster readout speed and no readout noise) in the left and right figures, respectively. The solar neutron event occurred on 2005 September 7 was assumed for simulating an emission of solar neutrons.

situation. Therefore, 10 times faster readout rate is the special requirement which should be achieved by developing new BEBs to realize the expected performance of the SciCRT.

3.2 Development of new BEBs

Prototype of new BEB and SiTCP

Before development of the new BEB, its prototype was produced at the Solar-Terrestrial Environment laboratory in Nagoya University. Figure 3.1 shows a picture of the prototype for readout of one FEB. Two FPGAs are implemented on this board: SiTCP is implemented on one FPGA, the other one is used for control of VA/TA chips on FEB. Other parts are produced based on the old BEB.

SiTCP (Uchida, 2008) is a key technology for the development of the new

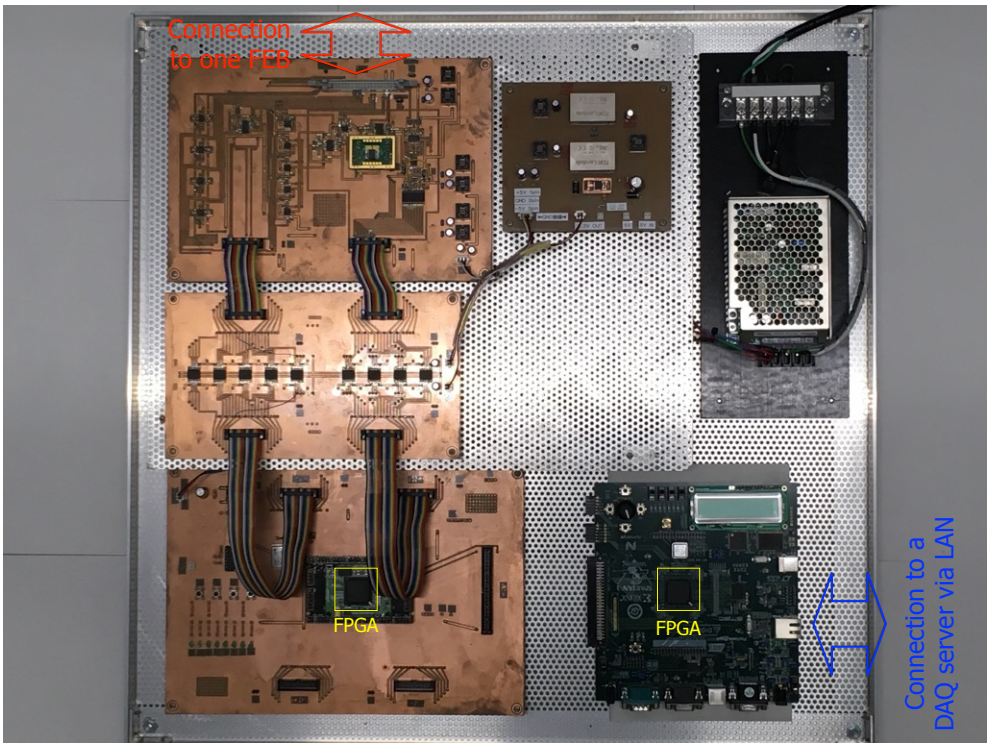

Figure 3.2: Picture of a prototype of the new BEB. In the lower-right corner, there is the Spartan-3AN starter kit. Other boards are originally produced at the STE laboratory. In the right center, there is a regulator board which supplies power to the FEB, analog/digital parts of this prototype, and isolation devices. In the left side, VA/TA interface board, isolation board, and FPGA board are deployed from the top.

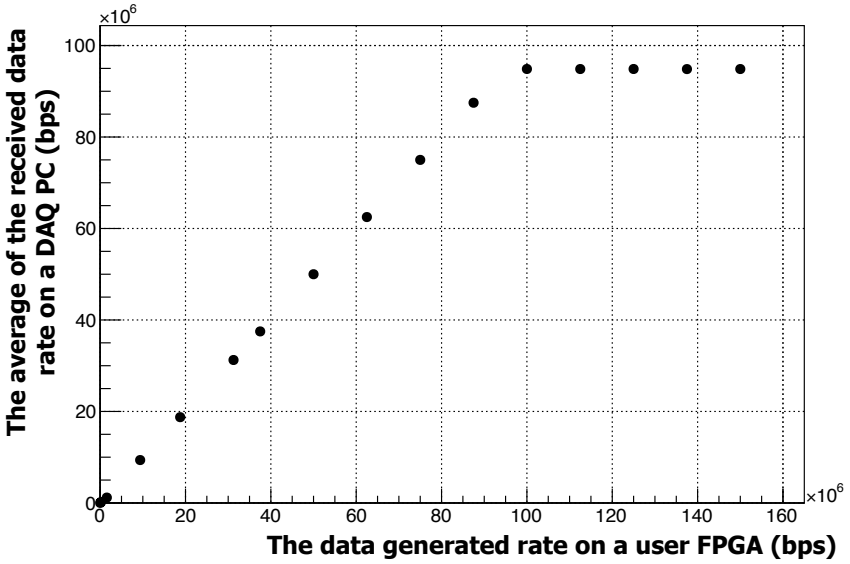

Figure 3.3: Result of the measurements of the data transfer via 100 Mbps SiTCP using the Spartan-3AN Starter Kit developed by Xilinx. The maximum rate of received data was about 95 Mbps.

BEB. It is a hardware-based network processor, which can be implemented on a FPGA produced by Xilinx Inc. SiTCP corresponds to two protocols in transport layer: Transmission Control Protocol/Internet Protocol (TCP/IP) and Remote Bus Control Protocol (RBCP). RBCP is based on UDP. TCP has high reliability with a connection-oriented protocol, in contrast to UDP, which is connectionless. In most cases, TCP/IP is applied to data transfer of ADC data, and RBCP is used for slow control. SiTCP has two kinds of firmwares of 100 Mbps and 1 Gbps.

I tested data transmission performance of 100 Mbps SiTCP with the Spartan-3AN Starter Kit produced by Xilinx Inc. A counter, that is implemented on the FPGA was used as a data generator. The proportion of data obtained in a Linux PC was measured using the time information of the Linux PC which is based on a function of C programming language, gettimeofday(). Figure 3.3 shows the relation between the transferred data rate from the starter kit and the received data rate in the Linux PC. The measurement shows that data are transferred to the Linux PC at the maximum speed of about 95 Mbps via TCP/IP.

According to this measurement result, the maximum trigger rate of neutrons can be roughly estimated. In the case of readout of one FEB, it is as follows:

$$\frac{95 \text{ Mbps}}{16 \text{ bit} \times 64 \text{ channels} \times 1 \text{ FEB}} = 93 \text{ kHz} \tag{3.1}$$

It corresponds to 23 kHz and 12 kHz of the trigger rate for readout of 4 and 8 FEBs, respectively. The network readout system is different from the VME readout system. ADC data are read out by each BEB from a DAQ server. In the actual case, ADC data from multiple new BEBs are read out by a network switching hub. Therefore, the maximum trigger rate is eventually determined by two parameters: how many FEBs are read out by one new BEB, how many BEBs are processed by one DAQ server.

1 Gbps SiTCP has a capability to deal with 10 times larger data than 100 Mbps SiTCP. On the other hand, 100 Mbps SiTCP wastes less heat and provides higher reliability for operation. It is required that the new BEB keeps running without any troubles for at least several years. 100 Mbps SiTCP has already provided the competent performance of data transfer capability as already shown. Therefore, I adopt 100 Mbps SiTCP for the data transmission technique of the new BEB.

Development of new BEB

We developed two new BEBs in March 2014. A picture is shown in Figure 3.4. We evaluated the basic performance for several items, that are described in Section 3.3, in Nagoya. After we assembled the new BEBs, we tested them using a part of the SciCRT at Mt. Sierra Negra in November 2014. We successfully obtained cosmic-ray data using a few data taking modes at that time. Then we developed eight new BEBs for installation in the SciCRT in March 2015.

Hereafter, I describe the configuration and the specification of the new BEB in comparison with the old BEB.

The old BEB is equipped with several PLDs described in Subsection 2.2. On the other hand, the new BEB has only one FPGA chip to control Ethernet communication (SiTCP), FEB interface and TRGB interface. Since the new BEBs are assembled to a rack with a power supply and a powerful circulator at the outside of a dark box which covers the detector, the waste

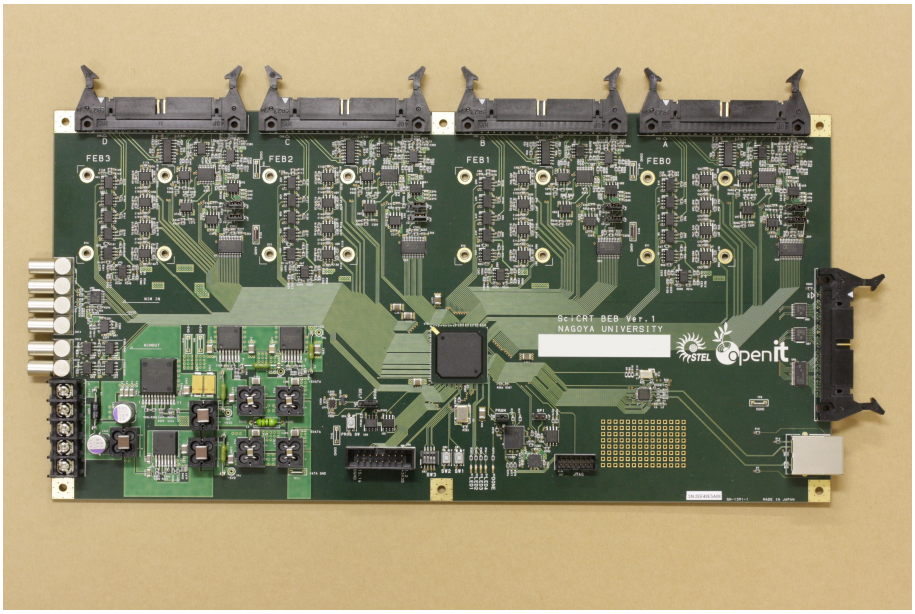

Figure 3.4: Picture of the new BEB. It is 160 mm wide by 320 mm long, developed as a six-layer board. A Xilinx Spartan-6 family device (XC6SLX100-2FGG484i) is implemented on the center of this board.

of heat is suppressed satisfactorily. One thermometer is added to the new BEB to monitor the waste of heat.

The SciCRT is always operated under an unattended mode at the mountain. Therefore I implemented a function of the FPGA configuration through Ethernet via SiTCP. It enables us to reconfigure the FPGA remotely. We call this the auto configuration mode. Then the FPGA is configured at a fixed interval (once a day) for the countermeasure to Single Event Upset (SEU) using the auto configuration mode.

To follow we describe how to use the new BEB in our experiment. A schematic diagram of the new BEB is shown in Figure 3.5. An internal clock (IntCLK) is generated by the FPGA and is sent to an external clock distributor through a NIM interface. The clock distributor provides all BEBs with a common system clock (ExtCLK).

The TA is initialized from the new BEB (TA control), and the threshold (Threshold) is set via RBCP through a digital to analogue converter (DAC). Hit signals (Hit×8) are passed to a TRGB after conversion to Low Voltage Differential Signaling (LVDS) signals. Trigger signals are supplied from the

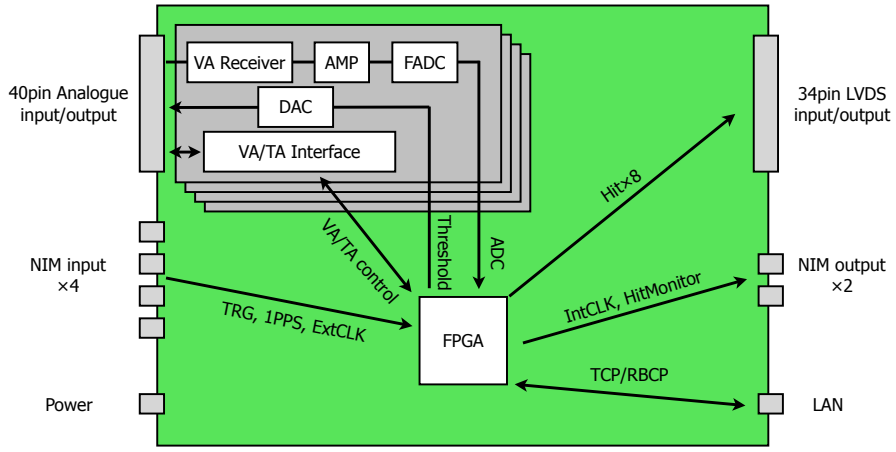

Figure 3.5: Schematic diagram of the new BEB for the SciCRT. The function of each signal is described in the text.

NIM input, and then the VA is sequentially controlled by the new BEB (VA control). ADC data are sent to the FPGA, and it is transferred to the DAQ server via TCP/IP.

Since each new BEB takes ADC data independently, it is needed to combine the data between new BEBs event by event. An event build counter is used for reconstructing each event's data. To reset event build counters, 1 PPS clock signal (1PPS) is distributed to all new BEBs commonly. We also monitor each hit signal (HitMonitor) from the NIM output using an oscilloscope at the field. We can simply switch a monitoring channel of each hit signal by RBCP.

The 4 m length cable is subject to an influence of noise. Hence, we adopt a 150 Ω resistor which is larger than the matching impedance (100 Ω) with the cable for reducing high frequency components.

3.3 Performance tests

3.3.1 Pedestal noise

I evaluated a noise level for the pedestal distribution. Common mode noise can be subtracted by off-line analysis. Pedestal noise is defined as follows: 64-channel average of the root mean square for each channel's pedestal distribution after common mode subtraction. I compare two distributions,

ADC raw data and common mode subtracted data, in the right of Figure 3.6. The common mode subtracted distribution is almost overlapped with the raw data distribution so that these two distributions cannot be distinguished. The left panel of Figure 3.6 shows the fluctuation of the pedestal distribution in which the trend of common mode noise cannot be mostly seen. Figure 3.7 shows the mean and RMS distributions of 64 channels in one MAPMT for ADC raw data and common mode subtracted data. As a result of the analysis, 0.4 and 1.9 ADC counts are derived for common mode noise and normal mode noise, respectively. Therefore we may conclude that normal mode noise is dominant for our new BEB, which is equivalent to 0.3 p.e., and countermeasures for common mode noise in the new BEB are sufficient, e.g. line bypass to signal and power supply lines. I used a shielded twisted-pair cable 4 m long between the FEB and the new BEB. This shielding also has a function to suppress normal mode noise. As a matter of fact, I obtained 2.8 ADC counts for normal mode noise using a non-shielding cable. As 1 MIP is equal to about 10 p.e. at the opposite edge of the scintillator bar (Yoshida et al., 2004), a signal to noise (S/N) ratio of about 30 is achieved.

3.3.2 Sample&Hold time and ADC peak hold time

The Sample&Hold time and ADC peak hold time must be tuned to maximize ADC counts.

Figure 3.8 shows a sampled waveform of the VA slow shaper obtained changing the Sample&Hold time with a step of every 40 nsec. Since the beginning of the hold time is not set to correspond to the rise of the VA slow shaper, the peak does not match to 1.2 μsec which is the peaking time of the VA slow shaper. In the following contexts, the hold time is fixed to be about 450 nsec.

We have used a FEB-BEB cable 4 m long as mentioned in Subsection 3.3.1. However as the cable gets longer the waveform from the VA is further smeared for the edge of the waveform. If there is a large waveform in one of 64 channels, the pedestal level will be shifted on the both channel sides by the wide-based waveform. This is the baseline-shift crosstalk.

Since the peak hold method is used for both the old and new BEBs, we obtain just one peak hold value for each channel as 12 bit ADC data. By changing the AD conversion time for each measurement, we can finally obtain the entire waveforms of 64 channels as if the waveform sampling method

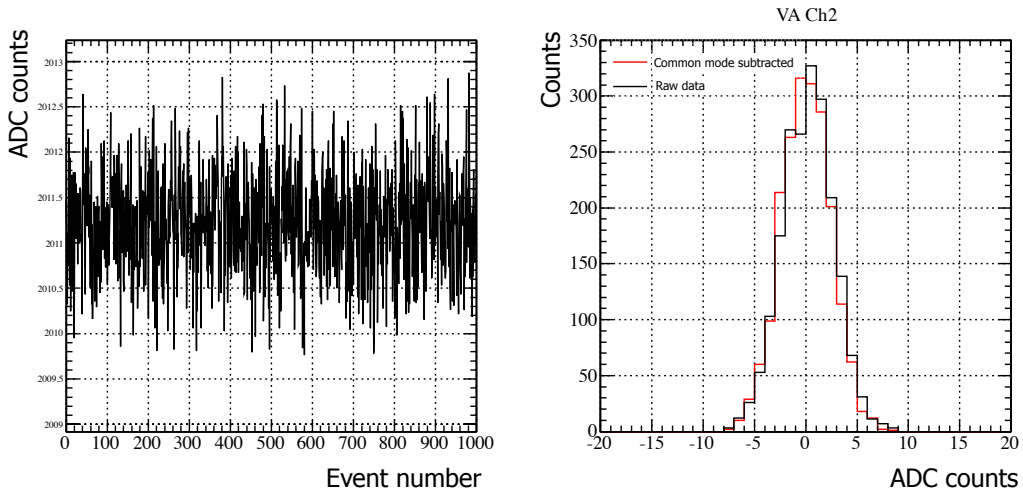

Figure 3.6: Fluctuation of raw pedestal ADC data and a typical example of pedestal distributions. Left: fluctuation of ADC counts in 1000 ADC events. Right: the raw data is shown by the black solid line, and the common mode subtracted distribution is shown with the red solid line. The number of event samples is 2000 in both distributions. For comparison, the peak of these distributions is normalized to zero ADC counts.

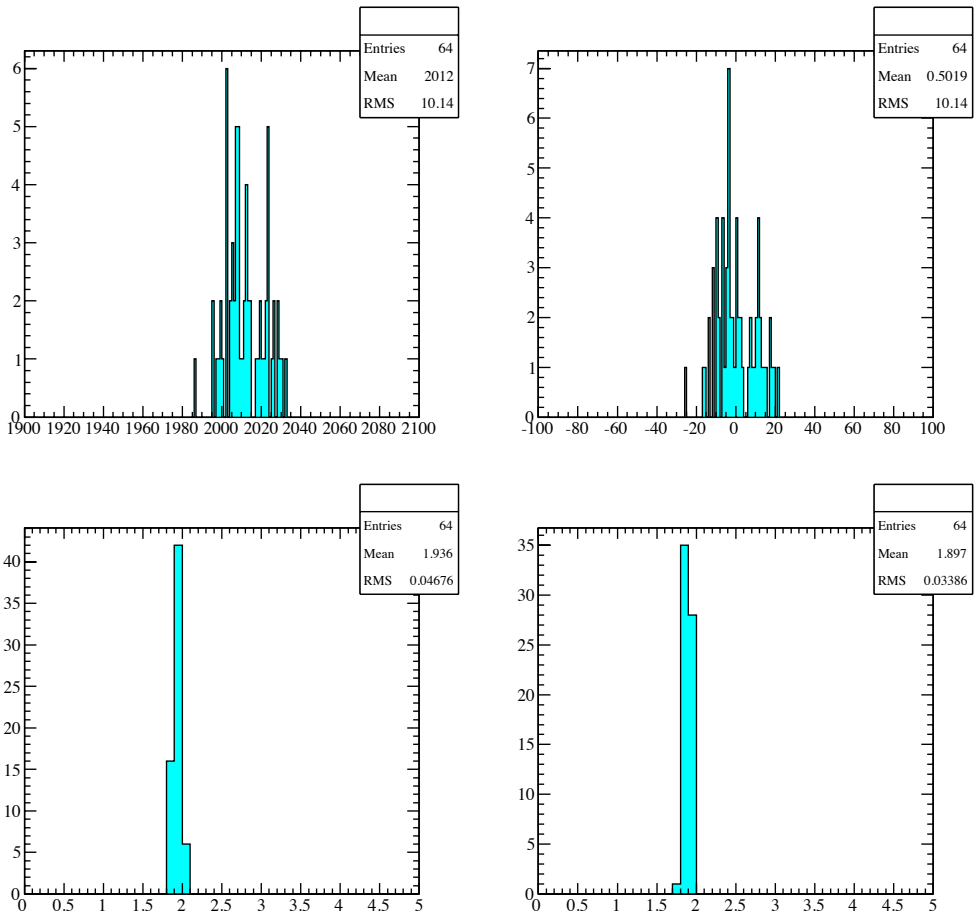

Figure 3.7: Mean (top panels) and RMS (bottom panels) distributions of 64 channels for ADC raw data (left panels) and common mode subtracted data (right panels) by using the 4 m shielded twisted-pair cable.

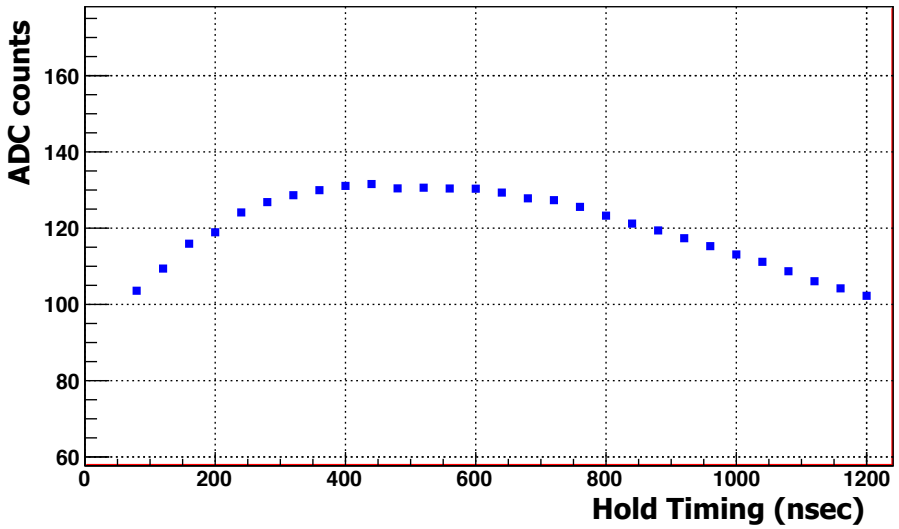

Figure 3.8: Sampled waveform of the VA slow shaper which is obtained changing the sample&hold timing with a step of 40 nsec.

is used.

The sampled waveform for peripheral channels are shown in Figure 3.9, in the case dummy signals are supplied to one of 64 channels. We put the waveforms of just five channels in Figure 3.9 out of 64 channels for simplicity. These channels are shown by five different colors in Figure 3.9, which are sampled by changing the peak hold time every 40 nsec. The red waveform shows the channel to which dummy signals are supplied. The edge of the pulse is strongly smeared, whereas the peak of the pulse is not so strongly smeared. The pink and blue waveforms are the left and right channels to the red waveform in the order of output from an analog multiplexer. The shift of a baseline can be seen at the left side of the blue waveform and at the right side of the pink waveform.

Since three dots are stable between 1000 to 1400 nsec, we finally fixed the peak hold time around 1200 nsec. In addition to this, I discuss about the measurement of the crosstalk in Section 3.3.4.

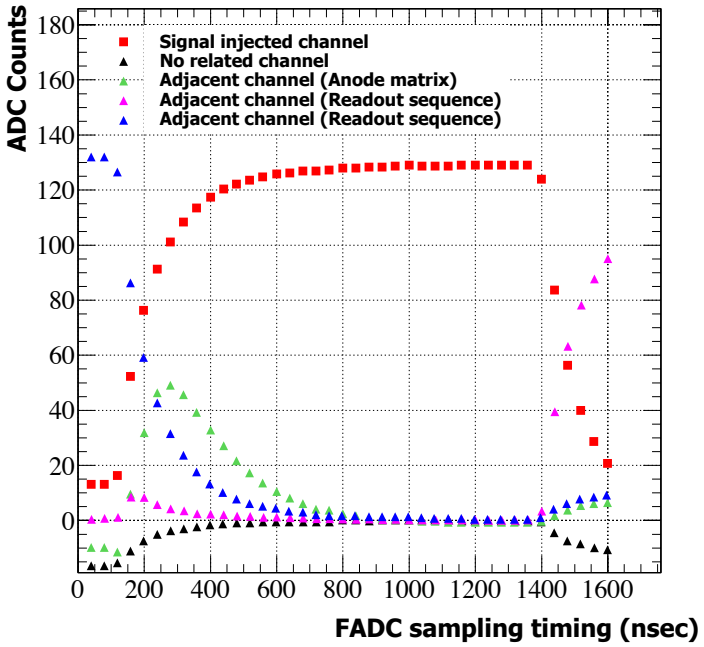

Figure 3.9: VA waveform scanned by changing the ADC sampling time. The red dots are sampled points on a channel to which the test pulse was applied. The pink and blue dots are the front and rear channels to the channel to which signals were applied in the VA readout sequence. The black dots are the channel which is independent of the signal applied channel. The green dots are one of the adjacent channels for the anode matrix on the MAPMT. We determined to adopt the sampling point at around 1200 nsec.

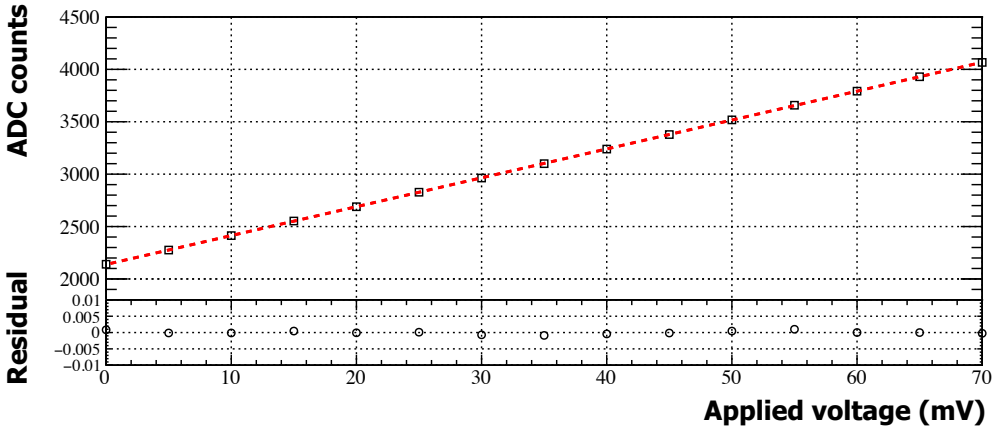

Figure 3.10: Typical example of the ADC linearity for input voltages from 0 to 70 mV. Values of the vertical axis show an average of ADC counts. Each point includes the error bar derived from one sigma by a gaussian fit. The pedestal offset was set to around 2048 counts, because negative signals can be detected in the pedestal distribution. The dynamic range, hence, is actually equal to 11 bit to negative charge injection from the MAPMT. The bottom panel shows the residual of each point of the linear fit.

3.3.3 Linearity

I measured the ADC linearity of the new BEB. Dummy signals of VA slow shaper are supplied to input line of a new BEB. The signals are constant voltages which are common to all 64 channels and range from 0 to 70 mV. In this test, I used a DC input voltage source. Figure 3.10 shows that the linearity is estimated to be within 1% over the range of our flash ADC.

Neutron-induced stopping protons deposit energies 20 times larger than 1 MIP at the scintillator thickness of 1.3 cm. As the gain is set to 14 ADC counts/MIP in SBs, the maximum energy deposit is equal to 280 ADC counts. The ADC linearity is sufficiently ensured around about 2300 ADC, including the pedestal offset.

3.3.4 Electronics crosstalk

MAPMT crosstalk which is caused by knocking photons to other channels on a photocathode of MAPMT or charge leak in an amplification process is about 3% (Yoshida et al., 2004). Hence, the electronics crosstalk is required to be less than 3%. There are three possible causes of crosstalk as follows.

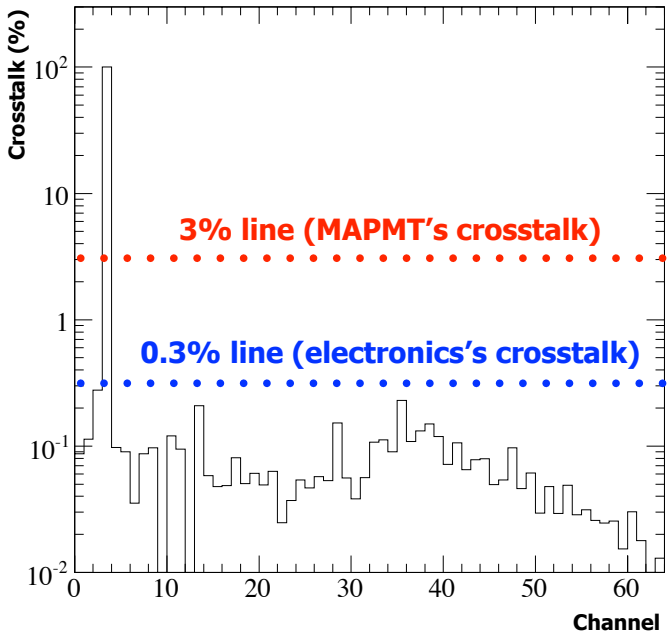

Figure 3.11: The proportion of electronics crosstalk in 64 channels. At the pulse injected channel (CH3), its peak of ADC data is shown as 100%. The most significant four channels are the adjacent four channels on the anode matrix of MAPMT (CH2, 13, 28 and 35).

- Adjacent channel's crosstalk for the anode matrix on MAPMT.
- Adjacent channels's crosstalk at input pins on the VA/TA chip.
- Previous and following channel's crosstalk caused by baseline shift of focused channel in the sequence of VA readout.

The electronics crosstalk was measured for readout electronics (a combination of one FEB, one shielded twisted-pair cable, and one new BEB) without MAPMT. As a result of the measurement, the proportion of the electronics crosstalk was estimated to be less than 0.3% as shown in Figure 3.11. The highest crosstalk recorded is about 0.3% at a previous channel (CH2) to a focused one (CH3) in the sequence of VA readout. This is because the channel is influenced by not only baseline shift of large signals in CH3 but also adjacent pattern on the anode matrix of MAPMT.

Table 3.1: Relation of pins between MAPMT, VA chip, and its TQFP package in 64 channels (Yamamoto, 2002). Test pulses are supplied to the channel which is surrounded by the double frame. There is the relatively large crosstalk in several channels which are surrounded by the single frame.

CHIP1			CHIP2		
MAPMT	VA	pin	MAPMT	VA	pin
0	25	27	32	63	33
1	22	24	33	62	32
2	19	21	34	61	31
3	16	18	35	60	30
4	15	17	36	35	5
5	12	14	37	34	4
6	9	11	38	33	3
7	6	8	39	32	2
8	26	28	40	27	29
9	23	25	41	56	26
10	20	22	42	21	23
11	17	19	43	50	20
12	14	16	44	45	15
13	11	13	45	42	12
14	8	10	46	39	9
15	5	7	47	36	6
16	27	29	48	58	28
17	24	26	49	55	25
18	21	23	50	52	22
19	18	20	51	49	19
20	13	15	52	46	16
21	10	12	53	43	13
22	7	9	54	40	10
23	4	6	55	37	7
24	31	33	56	57	27
25	30	32	57	54	24
26	29	31	58	51	21
27	28	30	59	48	18
28	3	5	60	47	17
29	2	4	61	44	14
30	1	3	62	41	11
31	0	2	63	48	8

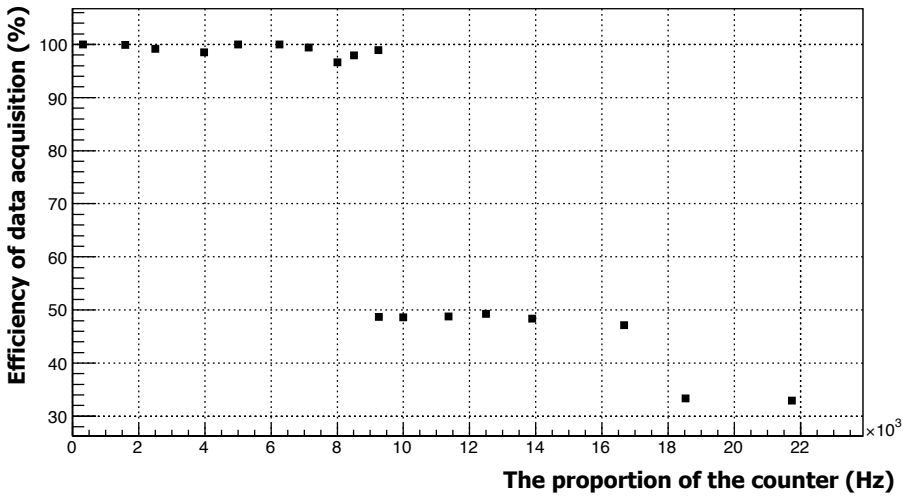

Figure 3.12: Efficiency of data acquisition in a DAQ server. Two new BEBs, one network switch, and one DAQ server are used in this test.

3.3.5 Throughput rate

Throughput is measured for a new DAQ system including new BEBs. There are two parameters to determine the absolute maximum trigger rate:

- Maximum readout rate of VA/TA chips: about 9.1 kHz/one FEB
- Maximum transmission rate of Ethernet communication: about 23 kHz/one new BEB

ADC data from each FEB are processed for one new BEB in parallel and finally transmitted to one FIFO memory. In short words, ADC data from four FEBs are processed at the maximum trigger rate of about 9.1 kHz.

In an actual case, multiple new BEBs are read out by one DAQ server through one network switch. Figure 3.12 shows efficiency of data acquisition in a DAQ server in case that two new BEBs are controlled by one server using one network switch. According to this result, it is evident that the throughput rate is limited up to 9.1 kHz for readout of ADC data from two new BEBs as well as the above case. If more than two BEBs are processed by one server, the throughput rate will be slightly decreased.

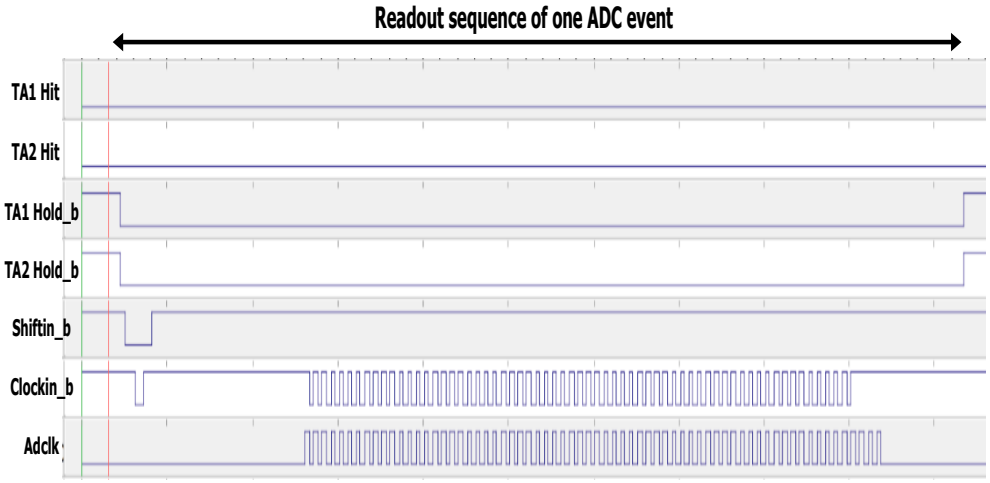

Figure 3.13: Behavior of internal signals in a FPGA on a new BEB observed by ChipScope Pro. This shows a readout sequence of ADC data from 64 channels by the self trigger mode of TA1 hit signals. Sequential signals are listed from the top: TA1 hit signals, TA2 hit signals, TA1 hold signal, TA2 hold signal, shiftin_b signal, clockin_b signal, and adclk.

3.3.6 TA noise hit during readout of ADC data

Old BEB has the VME readout noise problem stated in Section 3.1. New FPGAs produced by Xilinx has a function to observe internal signals of FPGAs on the window of PCs. For this test, I used ChipScope Pro which allows us to observe internal signals of Xilinx FPGAs. Figure 3.13 shows behavior of VA/TA control signals. In the case of old BEB, TA noise hits are induced by these control signals. On the other hand, it is confirmed that any noise hits do not occur on the new BEB and influence the transmission lines of hit signals during the readout sequence. Therefore, the number of neutron scaler data will be correctly counted even while ADC data are read out. It can also count the number of trigger signals for neutron ADC data, and hence to determine the live time of the DAQ system to correct for the dead time.

3.3.7 Power consumption and waste heat

Power consumption was measured for new BEBs using a clamp meter at Mt. Sierra Negra. According to our measurement, new BEB operates consuming about 30 W. Since one new BEB also supplies power to 4 FEBs, this

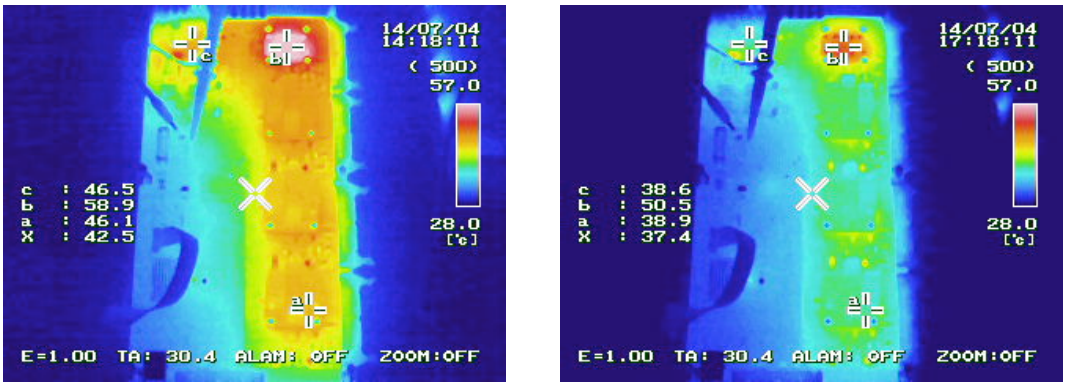

Figure 3.14: Pictures of a new BEB taken by an infrared camera in Nagoya's experimental room. The left picture was taken under no air condition control, whereas the right picture was done in an air-conditioned room. Three points, a-c, are focused to record the surface temperature of the new BEB, which is written in the left side of both pictures. Four heat sinks are equipped with each VA/TA interface of one new BEB, and point a focuses to one of the heat sinks. In the case of point b, a heat sink is not equipped. The point c is focused to DC-to-DC converters implemented on the new BEB.

value includes power consumption of four FEBs and the BEB totally.

Temperature is monitored for one new BEB by using an infrared camera. Figure 3.14 shows pictures of the new BEB taken by the infrared camera in Nagoya. According to the pictures of this figure, a combination of a heat sink and a cooling system are very effective for subtracting heat waste of the new BEB. Even if new BEBs are installed at Mt. Sierra Negra, the heat waste can be reduced by using such a cooling system.

3.4 Assembly and installation of new DAQ systems

Tests of one new BEB are performed at Mt. Sierra Negra in November, 2014. ADC data are obtained by using a few different data taking mode using a part of SB3: pedestal-run mode, self trigger mode, and two-fold coincidence mode without any coincidence of anti signals. At that time, I used a non-shielding short twisted-pair cable for connection between the new BEB and FEBs. As stated in Subsection 3.3.1 and 3.3.2, the cable length is not needed to be short and the linearity is substantially ensured for using

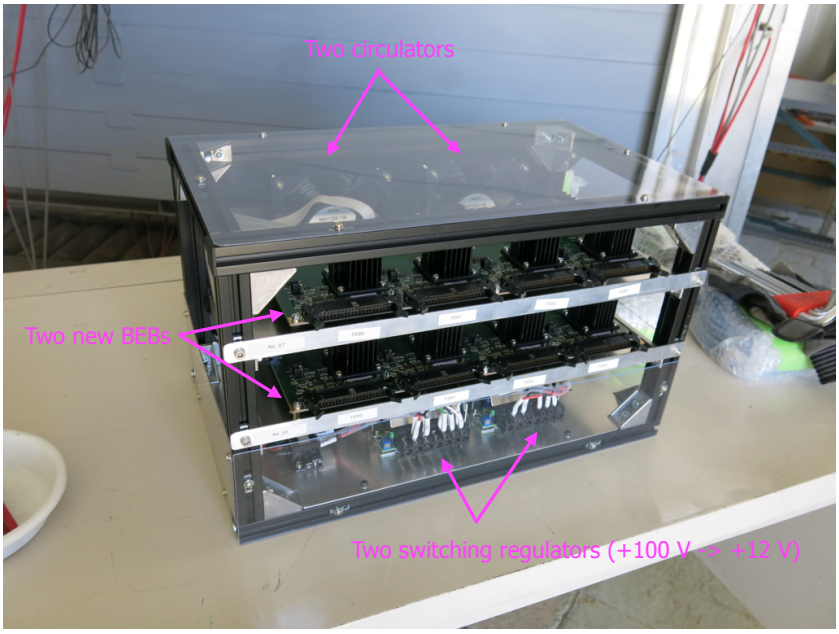

Figure 3.15: Assembled new two BEBs for muon layers.

the shielded twisted-pair cable. The pedestal noise is rather better than the short cable.

Subsequently, I decided to deploy new BEBs for muon layers and one of SBs, SB3, in the middle of 2015. For muon layers, two new BEBs are assembled in a rack with two switching regulators and two powerful circulators. The new DAQ system of SB3 has two separate racks in which three and four new BEBs are assembled. Figure 3.15 shows a picture of assembly of two new BEBs in a rack for muon layers. AC +100 V power is converted into DC +12 V power in a switching regulator, and it is converted to ± 5 V, ± 3.3 V, +1.8 V, and +1.2 V by DC-to-DC converters implemented on a new BEB.

Figure 3.16 shows the configuration of the new DAQ systems in muon layers and SB3. Two new BEBs are controlled by a DAQ server through a network switch in muon layers. This allows the 4-fold trigger rate of 9.1 kHz in maximum as mentioned in Section 3.3.5. On the other hand, seven new BEBs are controlled by a DAQ server through two network switches in SB3. The trigger rate of neutrons is limited up to about 3 kHz in maximum. Although throughput is limited, it is almost 10 times faster than the old one. It enables the trigger rate of about 260 Hz in maximum. Therefore, the 10 times faster readout rate was accomplished in this stage.

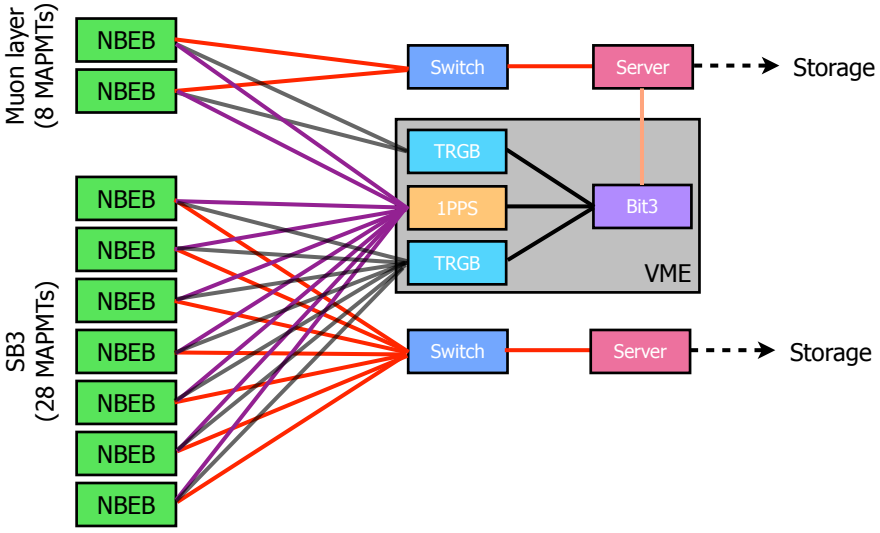

Figure 3.16: Final configuration of muon layers and SB3 in the SciCRT. NBEB represents a new BEB. The red line shows a LAN cable. Switch is a network switch. Bit3 is an adapter for VME bus transmission, produced by SBS technology Inc.

Two VME TRGBs are used to trigger particles for muon layers and SB3 as well as the old DAQ system. The system clock of these TRGBs are synchronized with an external system clock (64 MHz) supplied from a system clock distributor. Unlike in VME bus, an event flag is tagged with each event of ADC data: the ADC data are reconstructed by the event flag. The event flag is returned from an event build counter. It is implemented on each new BEB whose frequency is 1 MHz, which is set to be sufficiently faster than the actual trigger rate in muon layers and SB3. This counter is periodically reset by a signal of 1PPS which is distributed from a General Purpose Input/Output (GPIO) module. As shown in Figure 3.16, the two TRGBs and the GPIO module are controlled by a server which is engaged in a DAQ system of muon layers.

The DAQ software of one new BEB is created by a simple TCP/IP socket program. Multiple new BEBs are controlled by a shell script program in parallel. As for ADC data file, ADC data output from one new BEB are recorded in one data file. Contents of one event in a data file are as follows: the event number flag in the data file, local time recorded in a DAQ server, 16 bit ADC data of 64 channels from four FEBs connected, and the 32 bit event flag.

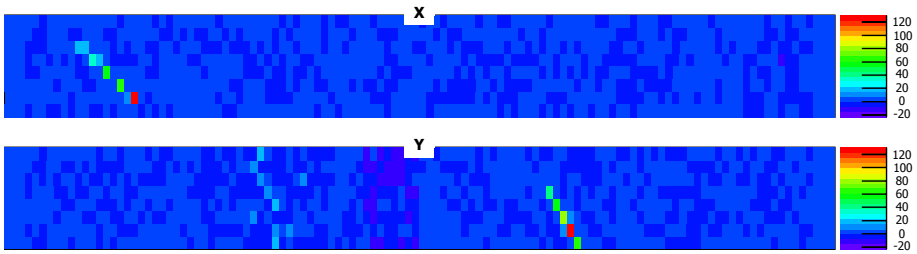

Figure 3.17: Sample of a neutron-like track obtained by the new DAQ system in SB3 on 2015 July 30.

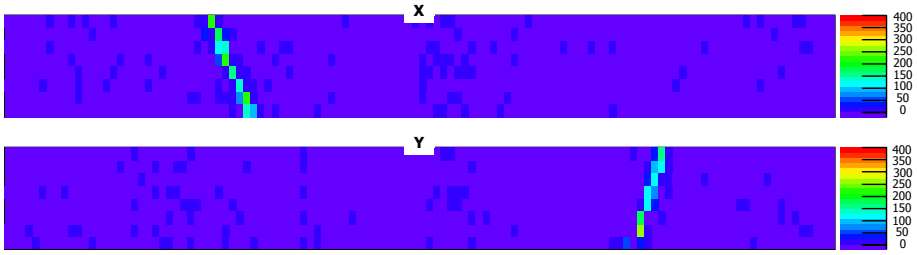

Figure 3.18: Sample of a muon-like track obtained by the new DAQ system in SB3 on 2015 November 27.

Muon ADC data and Neutron ADC data are successfully obtained by the new DAQ systems. Figure 3.17 shows a sample event display of a neutron-induced proton like track taken by X and Y sides, respectively. A muon calibration work was made for SB3 in November, 2015. Figure 3.18 shows a sample event display of a muon like track. Hence, it is confirmed that particles are correctly triggered and taken as neutron ADC data by these new DAQ system.

For the long-term stability, an example of the trigger rate of muon ADC data is shown in Figure 3.19. It is evident that the trigger rate is stable within 2% during the two weeks span of the plot in spite of the severe environment with an air mass of 585 g/cm^2. This fluctuation is consistent with that of a conventional muon telescope at Nagoya. Stable electrical power is always supplied from batteries and sine wave power inverters inside the electronics hut of the SciCRT. Batteries are continuously charged by the electrical power substation of the Large Milimetric Telescope (LMT) on the summit of Sierra Negra volcano. If the power is cut in an emergency by the LMT or by lightning, the DAQ system will be recovered when the power is restarted.

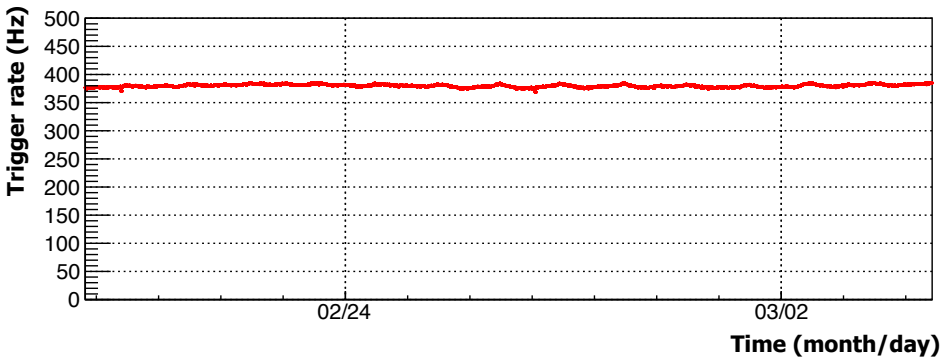

Figure 3.19: Example of the trigger rate of muon ADC data during two weeks. The term is from February 20 to March 4 in 2016. The trigger rate is about 380 Hz which is stable within 2%.

Chapter 4

Monte Carlo Simulation

Nagai et al. (2014) studied characteristics of the SciCRT using a Monte Carlo (MC) simulation. I re-evaluated the SciCRT with the new DAQ system using finally fixed parameters. At first, I describe a review of the MC simulation in this chapter. After that, I show results of re-evaluation of the future performance of the SciCRT.

4.1 Configuration of the MC simulation

A solar neutron event is assumed in this simulation. It is the most significant event on 2005 September 7 which was described in Chapter 1. This event was detected by the Mexico SNT deployed at the top of Mt. Sierra Negra, and hence appropriate to evaluate the performance of the SciCRT to solar neutrons. In this simulation, three assumptions are adopted as follows.

- The energy spectrum of solar neutrons at the Sun is followed by a power law function 6.1×10^{27} (E/100 MeV)$^{-3.8}$ MeV^{-1} sr^{-1}.
- An impulsive neutron emission was assumed.
- The solar zenith angle is set to be 17°.5.

Figure 4.1 shows configuration of the MC simulation. As shown in this figure, it consists of three simulation packages: Shibata model, PHITS, and GEANT4. Hereafter, I describe these packages one by one.

The Shibata model is a model to explain the propagation of solar neutrons in the Earth's atmosphere calculated by a Monte Carlo method using

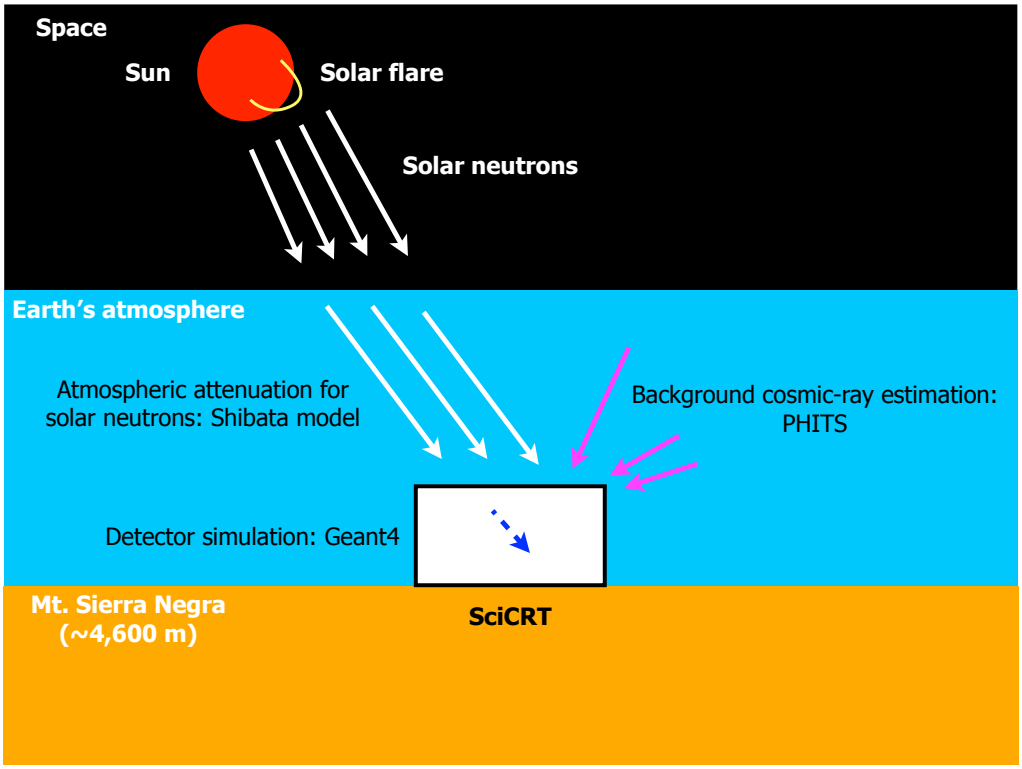

Figure 4.1: Global image of the MC simulation for the SciCRT at the top of Mt. Sierra Negra. The emission of solar neutrons at the most significant event on 2005 September 7 is assumed in this simulation. The Shibata model is used for simulating atmospheric attenuation of solar neutrons. Back ground particles are simulated by a PHITS code. GEANT4 gives the detector simulation. These details are described in the text.

Table 4.1: Parameters used in the simulation for the SciCRT with new DAQ systems assuming the 2005 September 7 solar neutron event.

Altitude of Mt. Sierra Negra	4,600 m a.s.l.
Vertical cutoff rigidity	8 GV
Force field potential	750 MV
Density of the scintillator bar	1.0 g/cm^3
Attenuation length of WLS-fiber	350 cm
Reflection rate of fibers at the edge	0.46%
Birks' constant	0.079 mm/MeV
Light yield	14 p.e./MIP
Cross talk for adjacent channel	3.0%
Readout dead time	106 μsec/BEB
Readout noise	No

a nuclear interaction model. It was confirmed that this model reproduces data obtained by the accelerator experiments (Koi et al., 2001). This model contains contribution of the elastic scattering process which has an important role for neutrons of low incident energies. The available energy region is ranged from 200 MeV to 1800 MeV.

PHITS (Particle and Heavy Ion Transport code System) is a package of calculation codes developed for simulating a behavior of a variety of radiations in materials using nuclear reaction models and nuclear data (Sato et al., 2013). In general, PHITS is used for design of accelerators, medical science, radiation protection research, and study on the transport of cosmic rays. In this case, it is applied to estimate background cosmic rays in the atmosphere of the Earth. Since gamma rays and neutrons are the most dominant contaminations for solar neutron observation by the SciCRT, it is momentous to know the behavior of these particles. Radiation transport in the atmosphere can be calculated by PHITS. It is confirmed that the estimation reproduces measurement results under a variety of situations. The result depends on the location, the cutoff rigidity, and the solar activity. Therefore, the PARMA model is constructed to predict cosmic-ray spectrum at arbitrary locations. Since the zenith angle distribution of particles cannot be calculated by the PARMA model, both the zenith angle table and the PARMA model are employed for our case.

GEANT4 (for GEometory ANd Tracking appeared in Agostinelli et al., 2003 and Allison et al., 2006) is a toolkit to track a behavior of particles in materials. The version of GEANT4 is 4.9.6 which uses QGSP BERT as a

hadron interaction model. The detector geometry of the SciCRT is created in this simulator. A sufficiently wide plane above the detector is assumed to allow particles to be injected without any loss.

The position and the energy information on particles are output from the GEANT4 simulation. The information is converted into VA/TA output information in a program, and data acquisition conditions of the current SciCRT experiment are applied to the information in another program. Parameters obtained by the new DAQ system are contained in these programs.

Table 4.1 shows parameters used in the simulation. The vertical cutoff rigidity and force field potential correspond to intensity of the geomagnetism and a solar activity index, respectively. These parameters are fixed to the location of 19,04°N and 97,3°W on 2005 September 7.

4.2 Significance of solar neutrons to background particles

Neutron scaler data

Neutron scaler data can be compared with the counting rate of the Mexico SNT for calculating the sensitivity to solar neutrons. Figure 4.2 shows time profiles of neutron scaler data assuming the solar neutron event on 2005 September 7. The time profiles are calculated for three cases: the old DAQ system, the new DAQ system, and an ideal DAQ system without any dead time of the readout electronics. The background count rate of these time profiles is normalized to that of the time profile which is actually obtained by Mexico SNT (>30 MeV neutral). The threshold energy of SBs is set to 7 MeV in this simulation.

The signal over noise ratio is calculated for 5 minutes around the peak. The significance becomes 38 σ and 61 σ for the old DAQ system and the new DAQ system, whereas it is 17 σ for data of the Mexico SNT. It is evident that the data acquisition of the new DAQ system is almost consistent with that of the ideal situation. This is because any readout noise does not occur for the new DAQ system. Especially, the live time of neutron scaler data was dominantly influenced by the VME readout noise of muon layers for the old DAQ system. Since the four-fold trigger rate is about 540 Hz for the old DAQ system, the live time of anti signals was limited to a half of the full live

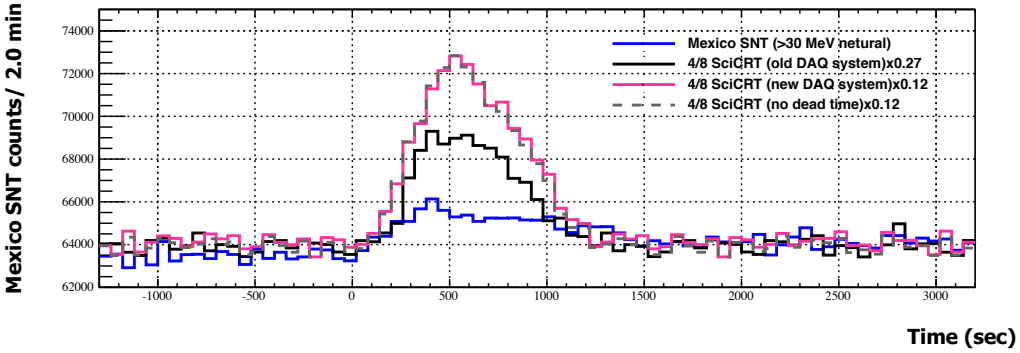

Figure 4.2: Normalized time profiles of scaler data which would be obtained by the SciCRT assuming the solar neutron event on 2005 September 7. The vertical dotted line at zero sec is the peak time of X-ray. The blue line shows real data obtained by the 30 MeV neutral channel of the Mexico SNT. The black line is data which would be obtained by scaler using 4/8 of the whole SciCRT under the current situation (1 kHz/BEB and VME readout noise). The green line illustrates a time profile obtained by the old DAQ system without the VME readout noise. The pink line is scaler data with new fast readout BEBs.

time. Hence, the counting rate is increased by a factor of 1.5, and the significance will be increased to 1.24 times. Furthermore, the live time of neutron scaler data is also limited by the VME readout noise of SBs. Because this limitation is also disappeared, the counting rate is increased by a factor of 1.43 which corresponds to 1.2 times for the significance. Therefore, it is estimated that the significance will be enhanced up to 1.5 times in comparison with the old DAQ system. This is consistent with 1.6 times which is derived from changes of the significance calculated.

It is concluded that the sensitivity of a half size of the SciCRT with the new DAQ system will be enhanced to 3.6 times higher than the Mexico SNT. This difference can be explained by the volume size of these detectors. Furthermore, it is clear that there is the peak of neutron scaler data with the new DAQ system at the later time of the peak of the Mexico SNT. This means that the SciCRT has a higher sensitivity to low energy neutrons compared with the Mexico SNT. This result shows that the SciCRT has a capability to detect lower flux and lower energy solar neutron events in the future.

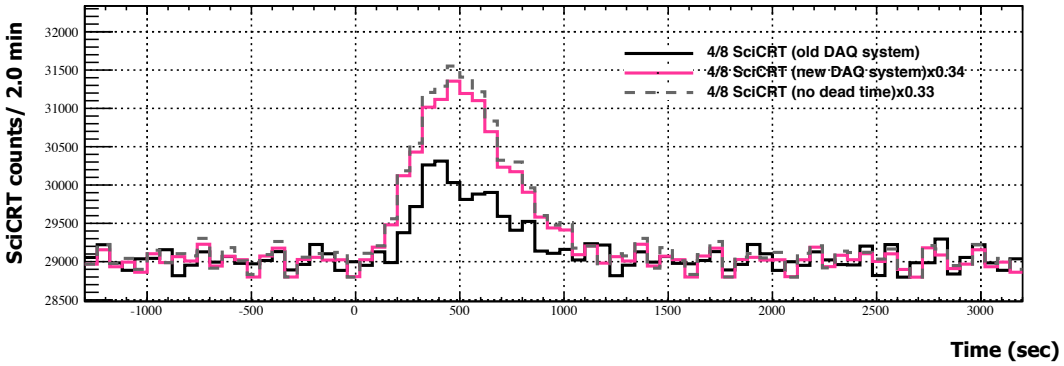

Figure 4.3: Time profiles of neutron ADC data would be obtained by the SciCRT assuming the solar neutron event on 2005 September 7. The black line is data that would be obtained using the old DAQ system. The pink line illustrates a time profile obtained by the new DAQ system. The dotted line shows a time profile under the ideal situation without any dead time.

Neutron ADC data

Figure 4.3 shows that normalized time profiles of neutron ADC data which would be obtained by a half size of the SciCRT. We can see the difference of the performance between the old DAQ system and the new DAQ system. The background count rate of these time profiles is normalized to that of the time profile using the old DAQ system. The significance is estimated to be 13σ and 21σ, respectively. The time profile obtained by the new DAQ system is almost consistent with the ideal situation.

Neutron ADC data are limited by two influences: the dead time of anti signals by the VME readout noise and the dead time for processing neutron ADC data. The dead time of anti signals has already been mentioned for the case of neutron scaler data. Hence, the counting rate is increased by a factor of 1.5, and the significance will be increased to 1.24 times. The dead time of neutron ADC data is improved and the count rate will be enhanced by a factor of 1.6. It corresponds to 1.26 times for the significance. Therefore, the significance will be totally improved up to 1.6 times. This is consistent with this simulation result.

In this calculation, I simulate the time profile of the new DAQ system using the currently used data acquisition conditions. It consists of the anti

Table 4.2: Significance of a half size of the SciCRT assuming three kinds of the trigger condition and the threshold energies of 1-7 MeV.

Threshold (MeV)	1	2	3	4	5	6	7
No coincidence	25.7	26.4	28.3	29.7	30.4	33.0	33.2
Double coincidence	23.3	22.3	22.6	23.5	22.8	21.8	21.2
Fourfold coincidence	8.2	4.7	4.2	4.3	5.0	2.6	-0.9

trigger condition (any signals from top and bottom layers without side anti layers), the trigger condition (Double coincidence), and the energy threshold (7 MeV). These conditions are optimized to enhance the significance of the old DAQ system. Therefore, the count rate of neutron ADC data is subtracted to be lower.

Therefore, I calculated the significance using different data acquisition conditions. Note that the anti trigger condition is fixed to the same condition as calculated for the old DAQ system. Table 4.2 shows calculated significances assuming three kinds of the trigger conditions and the threshold energies ranged from 1 to 7 MeV. In the following, the MC simulation is calculated using a combination of no coincidence and 5 MeV threshold energy for increasing the statistics of neutrons.

4.3 Accuracy of determining the energy spectrum of solar neutrons

The energy spectrum of solar neutrons can be approximated by a power-law function as explained in Section 1.3.3. In this section, I will discuss about an accuracy of determining the energy spectrum by the SciCRT. It is assumed that neutrons are emitted with several kinds of power-law indices at the solar surface. As described in Section 1.3.3, the TOF method has been applied to solar neutron events thus far to estimate the energy spectrum of solar neutrons. Hence, the same method can be employed for neutron scaler data obtained by the SciCRT. On the other hand, the energy spectrum can be estimated by a single analysis of neutron ADC data without any assumption. In the following, I will discuss about the accuracy of determining the energy spectrum of solar neutrons for both neutron scaler data and neutron ADC data, respectively.

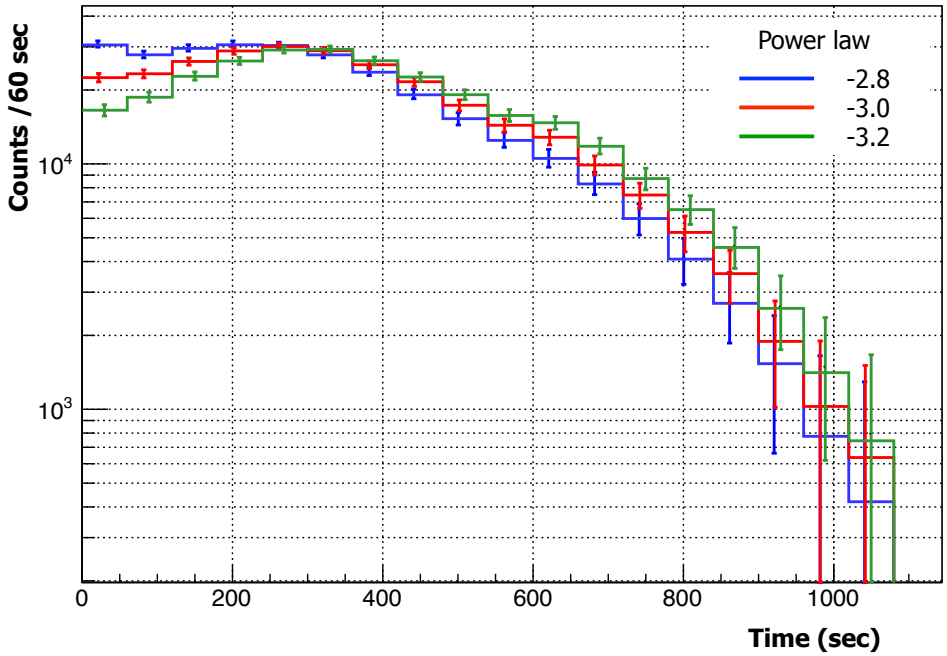

Figure 4.4: Time profiles of neutron scaler data estimated by the Monte Carlo simulation. Each line shows different three kinds of power-law functions α_e at the solar surface, namely –2.8, –3.0, and –3.2. Both statical errors of solar neutrons and background particles for each bin are included into each error bar. The threshold energy level is set to be 7 MeV.

Neutron scaler data

I simulate the time profile which would be obtained by neutron scaler data, assuming an emission of solar neutrons which is followed by a power-law function. The TOF method is applied in this case. Therefore, I assume several kinds of impulsive emissions of solar neutrons. Figure 4.4 shows the time profile with three kinds of power-law indices, whose α_s corresponds to –2.8, –3.0, and –3.2, respectively. The α_s means assumed power-law index at the source. The error bar of each bin includes the statistical error of background particles and solar neutrons. It is reproduced by a gaussian function with one sigma which is represented by a square root of the count rate of background particles.

The least squares method can be generally applied to comparing the spectrum of a model with that of experimental data. The model means an iden-

Table 4.3: Reduced χ^2 to fit each combination of α_s and α_e. α_s is the assumed power-law index and α_e is the obtained index by the experiment.

α_s \ α_e	–2.8	–2.9	–3.0	–3.1	–3.2
–2.8	1.0667	11.9985	42.7464	83.7626	142.3902
–2.9	12.0050	1.0728	11.1820	35.0723	75.5734
–3.0	42.7326	11.1724	1.0629	8.3220	31.5062
–3.1	83.4161	34.9969	8.3289	1.0719	9.5948
–3.2	141.5842	75.0999	31.3340	9.5657	1.0741

tical time profile assuming a power-law function with an index α_s. On the other hand, the experimental data mean a time profile which is fluctuated by a random gaussian function followed by a mean value and one sigma of α_s. Thus, the time profile is calculated for each α_s and its power-law index corresponds to α_e. For comparison, these time profiles are normalized to the total number of counts which is actually recorded by the Mexico SNT when the solar neutron event occurred on 2005 September 7.

$$\chi^2 \equiv \sum_{i=1}^{n} \frac{(N_{DATA}(i) - (N_{BG}(i) + N_{EV}(i)))^2}{(\sqrt{N_{BG}(i) + N_{EV}(i)})^2} \tag{4.1}$$

χ^2 is calculated in the equation 4.1. Here, $N_{DATA}(i)$ means the number of counts of the time profile with α_e for one bin i. $N_{BG}(i)$ and $N_{EV}(i)$ are the number of counts of the time profile with α_s for one bin.

Thus, the reduced χ^2 can be calculated for each combination of α_s and α_e as shown in Table 4.3. The degree of freedom (d.o.f) is equal to 17. Table 4.4 shows the confidence level for each reduced χ^2 calculated in Table 4.3. It is clear that the power-law index is determined within better than $\pm$ 0.1.

Neutron ADC data

In terms of neutron ADC data, the energy spectrum finally reconstructed from the deposited energy information depends on two data acquisition conditions: the threshold energy and the trigger condition of neutron ADC data. In this simulation, the conditions are set to be no coincidence condition with

Table 4.4: Confidence level calculated for each reduced χ^2 shown in Table 4.3. α_s is the assumed power-law index and α_e is the obtained index by the experiment.

α_s \ α_e	–2.8	–2.9	–3.0	–3.1	–3.2
–2.8	0.381	0	0	0	0
–2.9	0	0.375	0	0	0
–3.0	0	0	0.385	0	0
–3.1	0	0	0	0.376	0
–3.2	0	0	0	0	0.374

the energy threshold 5 MeV. It is also dependent on the method of off-line analysis to discriminate neutrons from other background particles. Hence, the same method as described in Nagai (2014) can be applied in the following. Figure 4.5 shows two-dimensional histograms which describe a relationship between the maximum energies deposited in one scintillator strip and the total deposited energies. The magenta line shows a boundary of neutron-gamma separation. It is supposed that the upper-left part is dominated by neutrons. In the following, the criterion is applied to selection of neutrons so that the purity of neutrons becomes about 80%.

Thus, the energy spectra reconstructed from neutron ADC data are illustrated for three kinds of power-law indices α_e in Figure 4.6. An instantaneous emission of neutrons are assumed here. As well as the case of neutron scaler data, the reduced χ^2 can be calculated for each combination of α_s and α_e as shown in Table 4.5. The d.o.f is equal to 48 in this calculation. Table 4.6 illustrates the confidence level calculated for each reduced χ^2 shown in Table 4.5. Therefore, the energy spectrum derived from neutron ADC data can be determined within an error of the power-law index around 0.1.

Then, I demonstrate that how well a difference between an impulsive emission and a short duration emission can be distinguished. Figure 4.7 shows energy spectra derived from neutron ADC data assuming the impulsive emission and the time duration with 5 and 8 minutes as an example of the short duration emission when the power-law index is fixed. The reduced χ^2 and the confidence level are shown in Table 4.7 and 4.8 for the power-law indices of –3.4. It is evident that the SciCRT has a capability to discrimi-

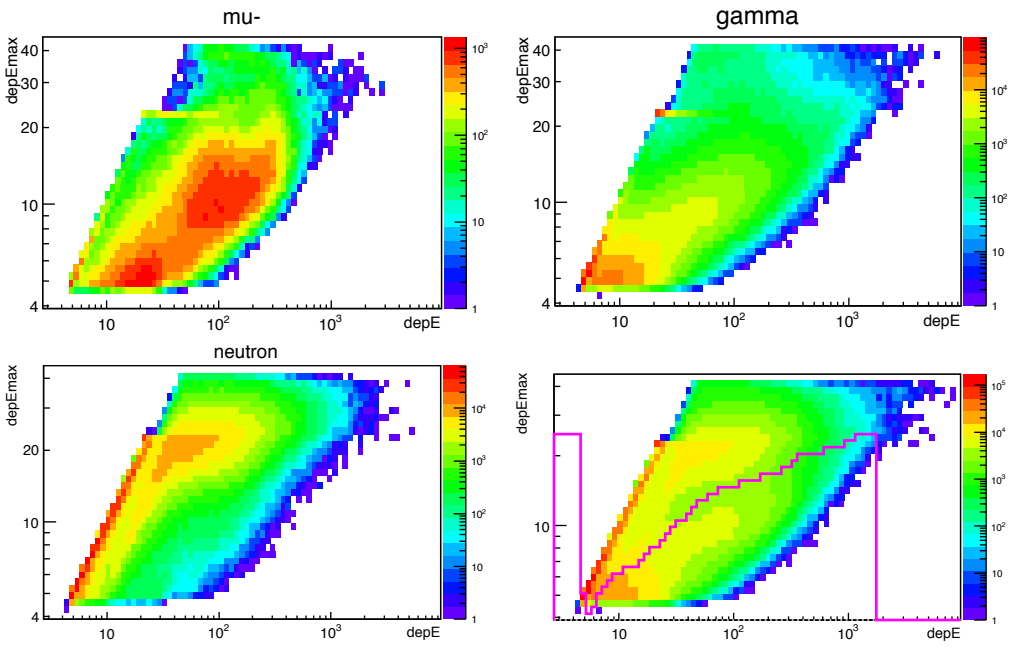

Figure 4.5: Two-dimensional histograms which show a relationship between the maximum deposit energies in one scintillator strip and the total deposit energies in the detector (Nagai, 2014). Each chart illustrates each particle's one: muons, gamma rays, neutrons, and all particles. In the lower-right figure, the magenta line shows the gamma-neutron separation line discussed in Nagai (2014).

Table 4.5: Reduced χ^2 to fit each combination of α_s and α_e. α_s is the assumed power-law index and α_e is the obtained index by the experiment.

α_s \ α_e	–2.8	–2.9	–3.0	–3.1	–3.2
–2.8	1.0230	1.6644	2.8998	4.9465	7.2789
–2.9	1.6490	1.0149	1.5498	2.6753	4.2059
–3.0	2.8768	1.5435	1.0173	1.4828	2.4697
–3.1	4.8982	2.6597	1.4901	1.0245	1.3941
–3.2	7.2628	4.1937	2.4690	1.4025	1.0221

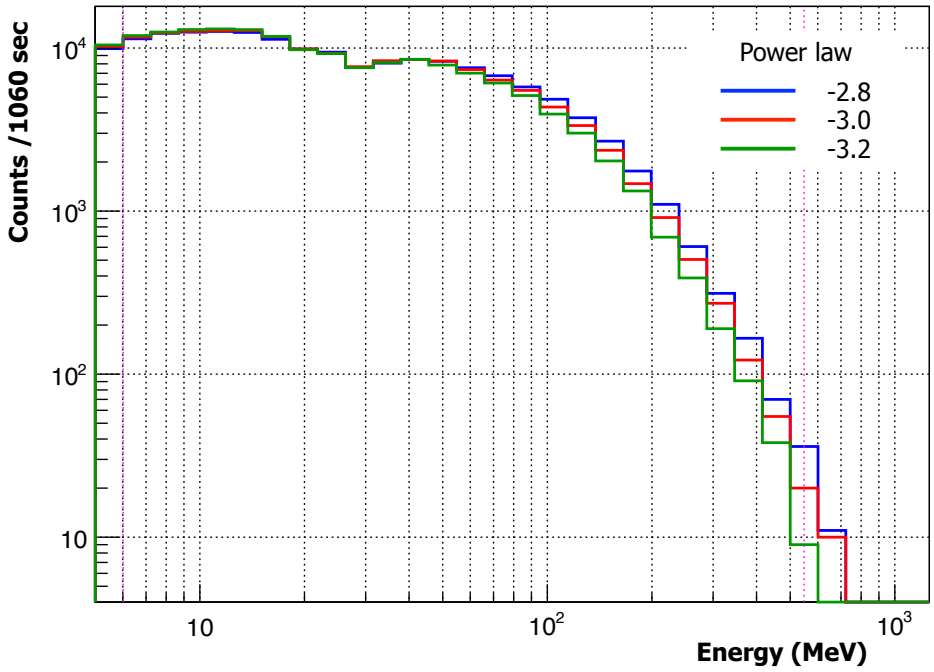

Figure 4.6: Energy spectra derived from neutron ADC data estimated in the Monte Carlo simulation. It is assumed that neutrons are emitted instantaneously at the Sun. Each line shows different three kinds of power-law indices at the solar surface, namely –2.8, –3.0, and –3.2. The dotted magenta lines show the duration between 6.01 and 548.2 MeV.

Table 4.6: Confidence level calculated for each reduced χ^2 shown in Table 4.5. α_s is the assumed power-law index and α_e is the obtained index by the experiment.

α_s \ α_e	–2.8	–2.9	–3.0	–3.1	–3.2
–2.8	0.429	0.003	0	0	0
–2.9	0.003	0.444	0.009	0	0
–3.0	0	0.009	0.439	0.017	0
–3.1	0	0	0.015	0.426	0.037
–3.2	0	0	0	0.034	0.430

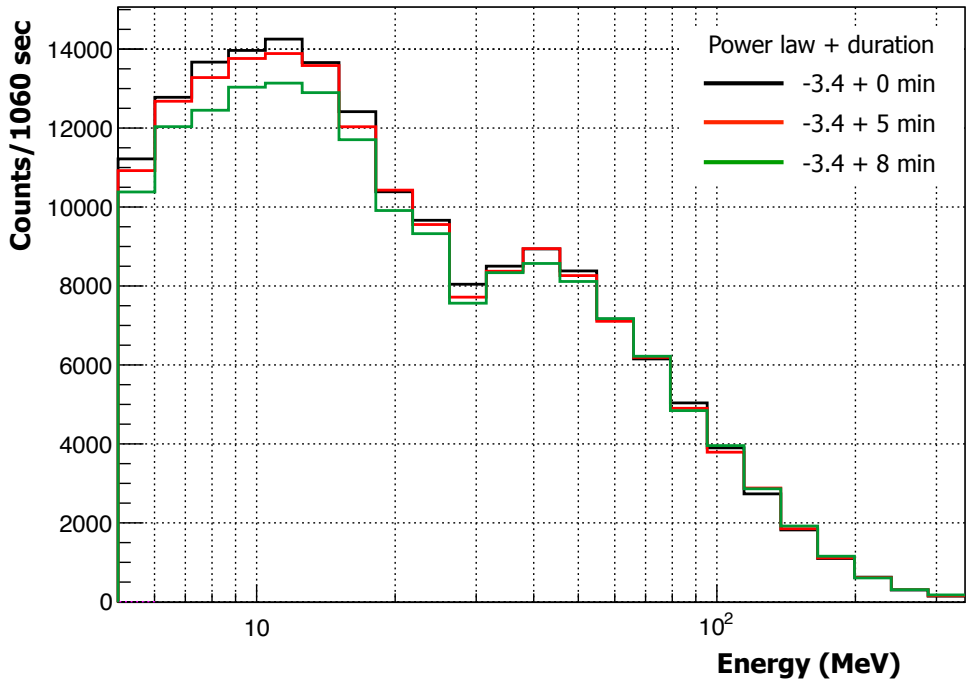

Figure 4.7: Energy spectra derived from neutron ADC data estimated in the Monte Carlo simulation. The lines show energy spectra with a power-law index –3.4. The black line is an energy spectrum assuming an impulsive neutron emission. The red and green lines are energy spectra assuming the neutron emission with durations of 5 and 8 minutes, respectively.

nate a difference between the emission of 8 minutes and the instantaneous emission for both power-law indices, although it is hard to distinguish the 5 minutes emission from the instantaneous emission.

Furthermore, the time profile derived from neutron ADC data may be helpful to determine the power-law index and the duration time. Figure 4.8 shows time profiles derived from neutron ADC data for various conditions. It is possible to discriminate three durations between 0, 5, and 8 minutes for a fixed power-law index. But it might be difficult to distinguish a different combination of the power-law index and the duration, e.g. –3.4 power-law index with 8 minutes duration and –4.0 power-law index with 5 minutes. To discriminate these degeneracy, a high-energy cut criterion is applied to these time profiles shown in Figure 4.8. The time profile for energies larger than

Table 4.7: Reduced χ^2 to fit each combination of α_s and α_e. α_s is the assumed power-law index and α_e is the obtained index by the experiment.

α_s \ α_e	–3.4	–3.4 with 5 minutes	–3.4 with 8 minutes
–3.4	1.0230	1.1943	1.9603
–3.4 with 5 minutes	1.1852	1.0149	1.5897
–3.4 with 8 minutes	1.9453	1.5923	1.0173

Table 4.8: Confidence level for each combination of α_a and α_e shown in Table 4.7. α_s is the assumed power-law index and α_e is the obtained index by the experiment.

α_s \ α_e	–3.4	–3.4 with 5 minutes	–3.4 with 8 minutes
–3.4	0.429	0.168	0
–3.4 with 5 minutes	0.178	0.444	0.006
–3.4 with 8 minutes	0	0.006	0.439

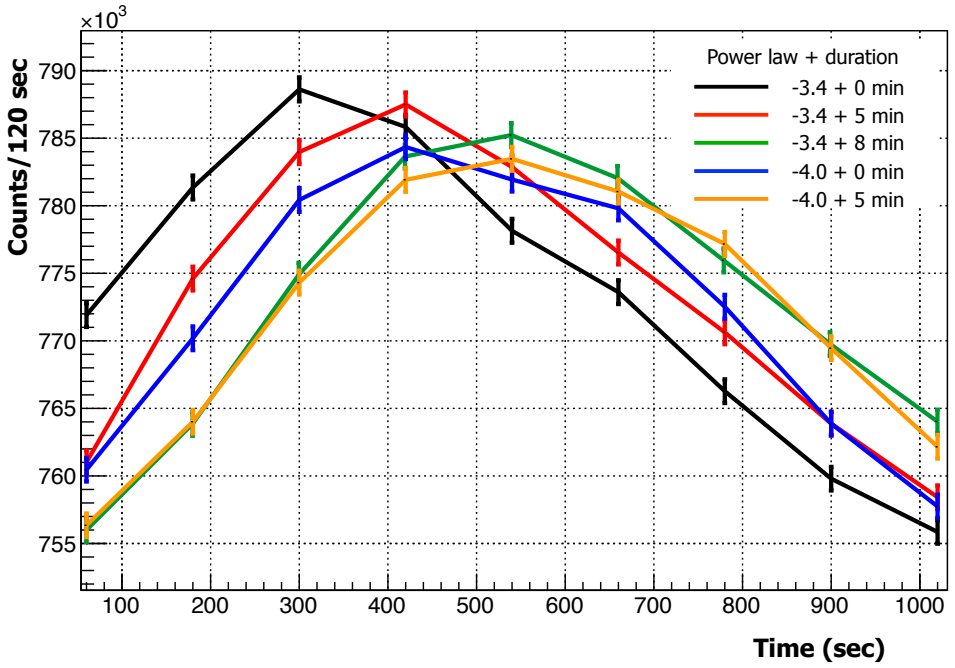

Figure 4.8: Time profiles derived from neutron ADC data assuming different power-law indices and emission durations. Each broken line has a different combination of the power-law index and the emission duration. Each point shows the count rate for 2 minutes with its statistical error.

200 MeV is shown in Figure 4.9. It is evident that each combination produces a different shape of time profiles. The case of the power-law index –3.4 and the duration 8 minutes and the power-law index –4.0 and the duration 5 minutes are discriminated.

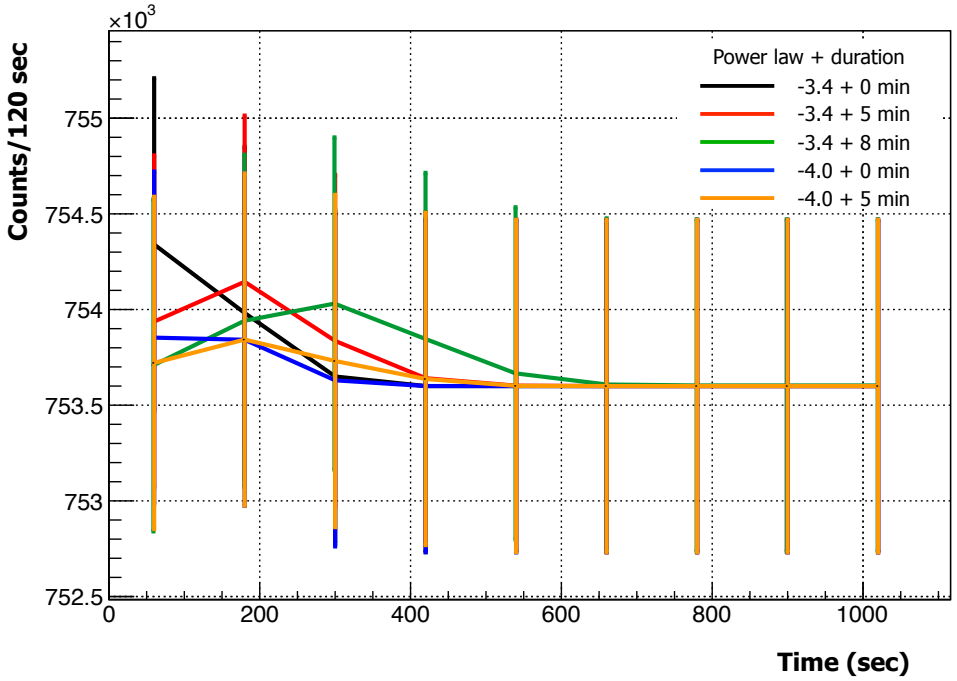

Figure 4.9: Time profiles derived from neutron ADC data after high-energy cut criterion. In this case, the value of the cut criterion corresponds to 200 MeV for total deposited energies. Each broken line has a different combination of the power-law index and the emission duration. Each point shows the count rate for 2 minutes with its statistical error.

Chapter 5

Conclusion

The purpose of the SciCRT (SciBar Cosmic Ray Telescope) is to observe high energy neutrons (>100 MeV) in association with solar flares, and it is expected to elucidate the acceleration mechanism of solar energetic particles which has been unknown. The SciCRT was originally constructed as a near detector (the SciBar detector) of the first long-baseline accelerator neutrino oscillation experiment, K2K. We use the detector as a cosmic-ray telescope. The SciCRT was installed at the top of Mt. Sierra Negra (4,600 m) in April 2013. Muon layers and three eighth of the SciCRT has been operated since September 2013.

Since the installation in 2013, the sensitivity of the SciCRT to solar neutrons has been very limited. In this thesis, I aimed to realize the full performance of the SciCRT for solar neutron events and studied the capability of the SciCRT to clarify the acceleration mechanism of ions which produce solar neutrons. The approaches and results of studies are described as follows.

The most dominant background components are background neutrons for our observations at the mountain. Therefore, studies of background neutrons is very important to extract solar neutron components. However, the readout rate of neutrons is limited by the dead time when ADC data are read out and its VME readout noise caused by the SciBar's electronics. These problems are basically caused by a combination of the Back-End Board (BEB) and the VME bus. Almost all the background components will be acquired in the SciCRT, if the readout rate becomes 10 times faster than the SciBar's one.

Therefore, I began to develop fast readout and more reliable new BEBs for the SciCRT. Instead of the VME bus, SiTCP is a key technology to implement a hardware-based network processor on a new BEB. It enables us

to realize network communication (TCP/IP and RBCP) via Ethernet. A prototype of the new BEB was produced in Solar-Terrestrial Environment Laboratory, Nagoya University. As a consequence of the test using the prototype, it is allowed to transmit ADC data with the maximum trigger rate of 93 kHz and 23 kHz for readout of 1 FEB and 4 FEBs, respectively. Thus, I determined to develop new BEBs for readout of 4 FEBs with 100 Mbps SiTCP. After the architecture was tuned according to results of performance tests, I designed and developed two new BEBs for actual operation in March 2014. After performance tests were done, eight new BEBs were produced to be deployed to the SciCRT.

The matters below were found by the performance tests. The pedestal distribution is sufficiently narrow. Common mode noise and normal mode noise are reduced to 0.4 and 1.9 ADC counts, respectively. Normal mode noise is dominant for the new DAQ system, which is equivalent to 0.3 p.e. The use of the shielded twisted-pair cable is also helpful to reduce the noise. Since a sample & hold technique and a peak hold technique are used in the new BEB, the hold timing and the ADC sampling timing are carefully optimized using a combination of the new BEB and the shielded twisted-pair cable. ADC linearity is measured for the new BEB unit. The linearity is sufficiently within 1% over the dynamic range of our FADC implemented on new BEBs. Assuming stopping protons in 1.3 cm of scintillator thickness, the linearity is satisfactory for observations of the SciCRT. The crosstalk of the electronics is measured and ensured less than 0.3% in the maximum case. This is sufficiently smaller than that of the MAPMT, about 3%.

No readout noise is measured when ADC data are read out. Now it is possible to count the number of events with 100% live time by a scaler. The trigger rate is allowed up to 9.1 kHz for readout of two new BEBs, and it is slightly decreased for readout of more than two new BEBs.

Finally, new BEBs were installed in a part of the SciCRT, muon layers and SB3, in the middle of 2015. For countermeasure of waste heat, these new BEBs are assembled into a rack with robust circulators and placed outside of a dark box surrounding the SciCRT. An example of a neutron-induced proton like trajectory is demonstrated in this paper. Stability of the new DAQ system is ensured within 2% in the two week's term from February 20 to March 4, 2016. Since new BEBs are also installed in muon layers, the live time of anti signals is 100%. Finally, the maximum readout rate of the new DAQ system is 10 times faster than old one, albeit limited by throughput for readout of multiple new BEBs.

In this thesis, sensitivity studies were made by using the MC simulation. In this simulation, the Shibata model was used to calculate the propagation of solar neutrons in the atmosphere. PHITS was employed to estimate background particles at Mt. Sierra Negra. The geometry of the SciCRT is simulated in GEANT4. I assume that a half size of the SciCRT works with the new DAQ system. The sensitivity of the SciCRT was estimated assuming the most significant solar neutron event occurred in 2005 September 7. Regarding neutron scaler data, the significance will be enhanced up to 1.5 times in comparison with the same size of the SciCRT using the old electronics. By this improved sensitivity, solar neutron events which are 10 times smaller than previously detected events can be obtained. Regarding neutron ADC data, it was found that almost all the background components can be obtained so that solar neutron components can also be fully acquired. Therefore, the data acquisition conditions of neutron ADC data are moderated for increasing the statistics of solar neutron components in the following calculations.

I estimated an accuracy to determine the energy spectrum and the emission duration of solar neutrons from the energy spectrum deposited by neutrons in the SciCRT. Assuming the emission of solar neutrons with several kinds of the power-law index, it was demonstrated that the SciCRT has a capability to separate a difference of the power-law index 0.1. Thus, the long duration emissions of solar neutrons at the Sun were assumed to study whether these are distinguished from each other. As a consequence of the simulation, it was found to be possible to discriminate a difference between an instantaneous emission and a long duration emission during 8 minutes. Furthermore, I calculated whether the energy spectrum and the emission duration of solar neutrons are determined simultaneously. By cutting low energy component $<$200 MeV, it was found that more complicated combinations of the power-law index and the emission duration can be well discriminated in comparison with the only information on the energy spectrum of deposited energies.

In conclusion,

1. I realized the full performance of the SciCRT. As for neutron scaler data, it is possible to detect 10 times smaller events than the most significant event which has been detected at the ground level.

2. According to the calculation of energy spectra derived from neutron

ADC data, it is possible to discriminate a difference between an instantaneous emission and a long duration emission during 8 minutes. The power-law index of the energy spectrum of solar neutrons can be determined within $\pm$ 0.1. If the difference between power-law indices is permitted up to 1.0, it is possible to discriminate the emission durations between 0 minutes, 5 minutes, and 8 minutes, respectively.

3. By cutting the low energy components in time profiles of neutron ADC data, the duration of the neutron emission and the energy spectrum of neutrons can be determined independently. This means the SciCRT unlocks the degeneracy problem between the emission time and the energy spectrum of solar neutrons.

Bibliography

M.G. Aartsen, et al., Constraints on Ultrahigh-Energy Cosmic-Ray Sources from a Search for Neutrinos above 10 PeV with iceCube. Phys. Rev. Lett **117** (2016)

R.U. Abbasi, et al., The energy spectrum of cosmic rays above $10^{17.2}$ eV measured by the fluorescence detectors of the Telescope Array experiment in seven years. Astropart. Phys. **80**, 131–140 (2016)

R.U. Abbasi, et al., Indication of intermediate-scale anisotropy of cosmic rays with energy greater than 57 EeV in the northern sky measured with the surface detector of the telescope array experiment. Astrophys. J. **790**(2) (2014)

A.A. Abdo, et al., Gamma-Ray Emission from the Shell of Supernova Remnant W44 Revealed by the Fermi LAT. Science **327** (2010a)

A.A. Abdo, et al., Observation of supernova remnant IC 443 with the Fermi Large Area Telescope. Astrophys. J **712**(1) (2010b)

J. Abraham, et al., Correlation of the Highest-Energy Cosmic Rays with Nearby Extragalactic Objects. Science **318** (2007)

A. Abramowski, et al., Acceleration of petaelectronvolt protons in the Galactic Centre. Nature **531** (2016)

P. Abreu, et al., Update on the correlation of the highest energy cosmic rays with nearby extragalactic matter. Astropart. Phys. **34** (2010)

M. Ackermann, et al., Detection of the Characteristic Pion-Decay Signature in Supernova Remnants. Science **339** (2013)

M. Ackermann, et al., High-energy gamma-ray emission from solar flares: summary of Fermi/Large Area Telescope detections and analysis of two M-class flares. Astrophys. J. **787**(1) (2014)

S. Agostinelli, et al., Geant4a simulation toolkit. Nucl. Instrum. Methods Phys. Res. A **506**, 250–303 (2003)

N. Agueda, et al., On the near-earth observation of protons and electrons from the decay of low-energy solar flare neutrons. Astrophys. J. **737**(2) (2011)

M. Ajello, et al., Impulsive and long duration high-energy gamma-ray emission from the very bright 2012 March 7 solar flares. Astrophys. J. **789**(1) (2014)

J. Allison, et al., Geant4 developments and applications. IEEE Trans. Nucl. Sci. **53**, 270–278 (2006)

P.V. Auger, et al., Extensive cosmic ray showers. Rev. Mod. Phys. **11** (1939)

B. Cerutti, et al., Extreme particle acceleration in magnetic reconnection layers: Application to the gamma-ray flares in the crab nebula. Astrophys. J **746** (2012)

B. Cerutti, et al., Particle acceleration in axisymmetric pulsar current sheets. Mon. Not. R. Astron. Soc. **448** (2015)

E.L. Chupp, High-energy neutral radiations from the Sun. Annual review of astronomy and astrophysics **22**, 359–387 (1984)

E.W. Cliver, H.V. Cane, Gradual and Impulsive Solar Energetic Particle Events. Eos Trans. AGU **83**, 61–68 (2002)

C. Dermer, B. Giebels, Active galactic nuclei at gamma-ray energies. C. R. Physique **17** (2016)

P. Evenson, et al., Protons from the decay of solar flare neutrons. Astrophys. J. **274** (1983)

W.C. Feldman, et al., Evidence for extended acceleration of solar flare ions from 18 mev solar neutrons detected with the messenger neutron spectrometer. J. Geophys. Res. **115** (2010)

W.C. Feldman, et al., Long-duration neutron production by nonflaring transients in the solar corona. J. Geophys. Res. **120** (2015)

S.E. Forbush, Three unusual cosmic-ray increases possibly due to charged particles from the Sun. Phys. Rev. **70**, 771–772 (1946)

D. Giannios, et al., Fast tev variability from misaligned minijets in the jet of m87. Mon. Not. R. Astron. Soc. **402** (2010)

R.G. Giovanelli, A theory of chromospheric flares. Nature **158** (1946)

J.O. Goldsten, et al., The messenger gamma-ray and neutron spectrometer. Space. Sci. Rev. **131**, 339 (2007)

L.X. González, et al., Re-evaluation of the neutron emission from the solar flare of september 07, detected by the solar neutron telescope at sierra negra. Astrophys. J. **814**(2), 1–7 (2015)

V.F. Hess, Über beobachtungen der durchdringenden strahlung bei sieben freiballonfahrten. Phys. Z. 13 **1084** (1912)

F. Hoyle, Some recent researches in solar physics (cambridge university press, cambridge) (1950)

X.-M. Hua, et al., Angular and energy-dependent neutron emission from solar flare magnetic loops. Astrophys. J. **140**(10), 563–579 (2002)

G.J. Hurford, et al., First gamma-ray images of a solar flare. Astrophys. J. **595**, 77 (2003)

G.J. Hurford, et al., Gamma-ray imaging of the 2003 october/november solar flares. Astrophys. J. **644**, 93 (2006)

K.H. Kampert, et al., 2012, Ultra-High Energy Cosmic Rays: Results and Prospects

T. Koi, et al., Attenuation of neutrons in the atmosphere and a thick carbon target. Nucl. Instrum. Methods Phys. Res. A **469**, 63 (2001)

D.J. Lawrence, et al., Detection and characterization of 0.58 mev neutrons near mercury: Evidence for a solar origin. J. Geophys. Res. **119**, 5150 (2014)

D.J. Lawrence, et al., The 4 june 2011 neutron event at mercury: A defense of the solar origin hypothesis. J. Geophys. Res. **120**, 5284 (2015)

H. Maesaka, et al., The K2K SciBar Detector. Nucl. Instrum. Methods Phys. Res. B **139**, 289–294 (2005)

N. Mandzhavidze, R. Ramaty, Gamma rays from pion decay - Evidence for long-term trapping of particles in solar flares. Astrophys. J. **396**(2), 111 (1992)

S. Masuda, et al., A loop-top hard x-ray source in a compact solar flare as evidence for magnetic reconnection. Nature **371** (1994)

R.A. Millikan, The Origin of the Cosmic Rays. Proceedings of National Academy of Science **12**, 48 (1926)

Y. Muraki, et al., Simultaneous observation of solar neutrons from the ISS and high mountain observatories in association with a flare on July 8, 2014. Sol. Phys. **291**, 1241–1265 (2015)

R.J. Murphy, et al., High-energy processes in solar flares. Astrophys. J. **63**, 721–748 (1987)

Y. Nagai, M.Sc. thesis (in japanese), Nagoya University, 2011

Y. Nagai, Observation of cosmic rays by the new solar neutron telescope, SciCRT, PhD thesis, Department of Physics, Nagoya University, 2014

Y. Nagai, et al., First cosmic-ray measurements by the scicrt solar neutron experiment in mexico. Astropart. Phy. **59**, 39–46 (2014)

K. Nitta, et al., The K2K SciBar detector. Nucl. Instrum. Methods Phys. Res. A **535**, 147 (2004)

E.N. Parker, Sweet's mechanism for merging magnetic fields in conducting fluids. J. Geophys. Res **62** (1957)

T. Piran, The physics of gamma-ray bursts. Rev. Mod. Phys. **76** (2005)

F. Piron, Gamma-ray bursts at high and very high energies. C. R. Physique **17** (2016)

E.R. Priest, et al., The magnetic nature of solar flares. Annu. Rev. Astron. Astrophys. **10** (2002)

J. Sakai, C.D. Jager, Solar flares and collisions between current carrying loops. Spa. Sci. Rev. **77**, 1–192 (1996)

T. Sako, et al., Super solar neutron telescope for the next solar maximum, in *Proc. of the 28th ICRC in Japan*, vol. 6, 2003, pp. 3437–3440

T. Sako, et al., Long-lived solar neutron emission in comparison with electron-produced radiation in the 2005 September 7 solar flare. Astrophys. J. **651**, 69 (2006)

T. Sato, et al., Particle and heavy ion transport code system, phits, version 2.52. Journal of Nuclear Science and Technology **50**, 913–923 (2013)

G.H. Share, et al., Physics of solar neutron production: Questionable detection of neutrons from the 31 december 2007 flare. J. Geophys. Res. **116** (2011)

G.H. Share, et al., Misidentification of the source of a neutron transient detected by messenger on 4 june 2011. J. Geophys. Res. **120**, 1 (2015)

P.A. Sweet, The neutral point theory of solar flares. in Electromagnetic Phenomena in Cosmical Physics, edited by B. Lehnert (1958)

S. Tsuneta, et al., Observation of a solar flare at the limb with the yohkoh soft x-ray telescope. PASJ **44** (1992)

T. Uchida, Hardware-based tcp processor for gigabit ethernet. IEEE Trans. Nucl. Sci. **55**, 1631–1637 (2008)

D.A. Uzdensky, et al., 2011, Reconnection-powered linear accelerator and gamma-ray flares in the Crab Nebula

J.F. Valdés-Galicia, et al., An improved solar neutron telescope installed at a very high altitude in méxico. Nucl. Instrum. Methods Phys. Res. A **535**, 656 (2004)

K. Watanabe, Solar neutron events in association with large solar flares in solar cycle 23, PhD thesis, Department of Physics, Nagoya University, 2005

K. Watanabe, et al., Solar neutron events of 2003 october-november. Astrophys. J. **636**, 1135–1144 (2006)

K. Watanabe, et al., Highly significant detection of solar neutrons on 2005 September 7. Adv. in Spa. Res. **39**, 1462 (2007)

K. Watanabe, et al., Physics of ion acceleration in the solar flare on 2005 September 7 determines γ-ray and neutron production. Adv. in Spa. Res. **44**, 789 (2009)

S. Yamamoto, 2002

T. Yokoyama, K. Shibata, Magnetohydrodynamic simulation of a solar flare with chromospheric evaporation effect based on the magnetic reconnection model. Astrophys. J. **549**, 1160 (2001)

M. Yoshida, et al., Development of the readout system for the k2k scibar detector. IEEE Trans. Nucl. Sci. **51**, 3043 (2004)

Neutron Monitor Database. http://www.nmdb.eu